FINE DROP RECOVERY IN BATCH GAS-AGITATED LIQUID-LIQUID SYSTEMS

Habibullah Shahrokhi

A thesis submitted in conformity with the requirements
for the degree of Doctor of Philosophy
Graduate Department of Chemical Engineering and Applied Chemistry
University of Toronto

FINE DROP RECOVERY IN BATCH GAS-AGITATED LIQUID-LIQUID SYSTEMS

Doctor of Philosophy

1998

Habibullah Shahrokhi

Graduate Department of Chemical Engineering and Applied Chemistry

University of Toronto

ABSTRACT

The hydrodynamics of batch gas-agitated liquid-liquid dispersions has received comparatively little attention in the open literature even though such systems arise in diverse contexts: batch pyrometallurgical processes, radioactive extraction processes and oil spills. Initially the two immiscible liquids form stratified layers. Liquid from the lower phase is then entrained into the upper phase in the form of small and large drops by gas bubbles passing through the liquid-liquid interface. At the end of a batch, gas agitation is stopped and the lower liquid phase drops suspended inside the upper liquid phase, separate under the influence of gravity. Fine drops separate slowly and consequently a small amount of the more dense liquid phase remains dispersed in the upper phase. For pyrometallurgical processes such as slag cleaning, long settling periods reduce equipment productivity and metal drops entrained in slag reduce metal yields. Both of these effects have sparked interest in slag cleaning and other remedial measures.

In this work, mechanisms for the recovery of fine water drops suspended in a sunflower oil + decane solution by injecting large nitrogen gas bubbles into the dispersion at a low

flux rate are assessed and it is shown how net rates of fine drop recovery can be enhanced by imposing circulation loops within the upper liquid phase that are oriented perpendicular to the liquid-liquid interface. Such loops are best generated through gas injection at or above the liquid-liquid interface. The primary mechanism for enhanced fine drop recovery, resulting from bubble injection, arises from improving drop liquid-liquid interface coalescence. Large drop-small drop coalescence is shown to be a secondary drop recovery mechanism. Bubble injection below the liquid-liquid interface, a frequently used industrial practice is not an optimal design option for exploiting these effects.

Measurements of drop concentration in the upper liquid phase reveal that there is an optimum gas flux corresponding to the best fine drop recovery rate and that the optimum gas flux is a function of fine drop concentration. At the optimum gas flux 20-100 μm diameter water drops are recovered at the approximately same rate. The overall rate of fine drop recovery is up to 4 times the rate obtained by gravity settling.

The physics of fine drop movement and capture in the experimental flow field are modeled numerically. Key features such as the spacial distribution of fine drops and the evolution of a complex concentration distribution pattern over time are modeled qualitatively. The model provides clear explanations for the drop concentration maxima arising remote from the bubble street and near the centroid of the circulation loops, and provides a basis for the development of a more general fluid mechanic model for such flows. The importance of mixing in the bubble street, and the flow profile adjacent to the liquid-liquid interface is also elucidated.

ACKNOWLEDGEMENT

I am deeply and greatly indebted to Professor John M. Shaw for his continual support, encouragement, inspiration and enlightening discussions during the course of this study. His open minded attitude toward suggestions has been valuable in maintaining the impetus behind this work.

I also wish to express a very special thanks to my committee members for their guidance and support, Professors David Kuhn for providing me the computing facility and Masahiro Kawaji for assistance in using his lab facilities. I am also grateful to Dr. Tokes Oshinowo for taking time to read this thesis and offer constructive criticism.

I appreciate the generous financial support of Centre of Metallurgy (CCPM) University of Toronto and the Natural Sciences and Engineering Research Council of Canada.

As always, I am in debt to my parents for their support, motivation and encouragement in pursuing higher education.

TABLE OF CONTENTS

Abstract ii

Acknowledgment iv

Table of Contents v

List of Figures ix

List of Tables xiv

Nomenclature xv

1.0 INTRODUCTION 1

1.1 Objectives 3

2.0 LITERATURE REVIEW 4

2.1 Fine drop generation 4

2.1.1 Prior experimental work (Shahrokhi and Shaw, 1994) 6

2.2 Possible mechanisms for fine drop recovery 9

2.2.1 Large drop-small drop coalescence 9

2.2.2 Drop-interface coalescence 10

2.2.3 Drop-drop coalescence in eddies 11

2.2.4 Drop recovery by flotation 13

2.3 Evaluation of proposed mechanisms 14

2.3.1 Large drop-small drop coalescence 14

2.3.2 Drop-drop coalescence in eddies 15

2.3.3 Drop-interface coalescence 16

2.3.4 Drop recovery by flotation 16
2.4 Bubble driven flow 18
2.4.1 Interphase force term 19
2.4.1.1 Friction force 19
2.4.1.2 Added mass force 20
2.4.1.3 Lift force (Magnus force) 20
2.4.2 Loop reactors and locally aerated bubble columns 22
2.4.2.1 Momentum balance for the gas phase 22
2.4.2.2 Fluid flow 23
2.5 Spacial drop concentration distribution 24

3.0 EXPERIMENTAL 26

3.1 Qualitative measurements 27
3.1.1 Experimental apparatus and procedure for observing the coalescence of drops inside eddies 27
3.1.2 Apparatus and procedures for large drop-small drop coalescence experiments 29
3.1.3 Apparatus and procedures for drop liquid-liquid interface coalescence experiments 31
3.2 Semi-quantitative measurements 31
3.2.1 Experimental apparatus and procedure 31
3.3 Measurements of flow fields induced by gas bubbles and spacial drop concentration distributions 37
3.3.1 Velocity fluctuation damping close to the bubble street 39
3.4 Sources of error 40
3.4.1 Factors affecting image quality 40
3.4.2 Drop size calibration 43

4.0 RESULTS AND DISCUSSION 44

4.1 Qualitative assessment of the coalescence mechanisms 44
4.1.1 Large drop-small drop coalescence 44
4.1.2 Drop liquid-liquid interface coalescence 45
4.1.3 Drop-drop coalescence in eddies 45
4.2 Quantitative drop recovery measurements 46

4.2.1 The impact of different agitation methods 46
4.2.2 The impact of circulation patterns on fine drop recovery 51
4.3 Flow field in the upper liquid phase 53
4.3.1 Flow pattern within circulation loops 54
4.4 Spatial drop concentration distributions 57
4.4.1 Drop concentration distributions time dependence 57
4.4.2 Drop concentration contours 64
4.5 Re-entrainment of small vs. large drops 66
4.6 The effect of gas flux on fine drop recovery 67
4.7 Summary 70

5.0 PREDICTION OF DROP CONCENTRATION PROFILES AND DROP RECOVERY RATE 71

5.1 Introduction 71
5.2 Upper liquid phase flow field 72
5.3 Drop trajectory computation procedure 74
5.3.1 Overview of dispersed phase modeling procedures 74
5.3.2 Boundary inputs for the dispersed phase 76
5.3.3 Calculation procedures 78
5.3.4 Time step 79
5.4 Numerical results 79
5.4.1 Example Drop trajectory 79
5.4.2 Capture zone 80
5.4.3 The effect of drop size on drop trajectory 81
5.4.4 The effect of Lift force on drop trajectory calculations 83
5.4.5 Mixing action of rising bubbles 84
5.4.5.1 Mixing zone bandwidth 84
5.4.5.2 Predicted recovery rate for 100 μm diameter drops 85
5.5 Predicted spacial drop concentration distribution for 100 μm diameter drops 88
5.6 Summary 90

6.0 CONCLUSIONS 92

7.0 RECOMMENDATIONS **94**

8.0 REFERENCES **96**

APPENDIX A: Drop concentration and recovery rate model **103**

A.1 Introduction 103

A.2 FORTRAN implementation 104

A.3 Main programs 106

A.3.1 Drop trajectory calculation in circulation loops 106

A.3.2 Drop recovery rate prediction 108

A.3.3 Spacial drop concentration distribution 110

A.3.4 Random number probability distribution 112

A.3.5 Subroutines referred to in the main programs 113

LIST OF FIGURES

Figure 1.1 -The formation and evolution of batch gas-agitated liquid-liquid dispersions. .. 1

Figure 2.1 -Fine drop production at the liquid-liquid interface for a viscosity ratio case (0.063). The width of each frame is 4.5 mm: (a) the bubble approaches the interface; (b) the bubble stretches the interface and pushes a thin film of lower liquid phase; (c) the film peels off the bubble and a column of the lower phase is pulled up in the wake of the bubble; (d) the column of the lower phase liquid thins just below the bubble; (e) and (f) the necked region adjacent to the bubble disintegrates to produce fine drops. (Shahrokhi and Shaw 1994) 5

Figure 2.2 -The over-all effect of step changes in agitation intensity on measured fine drop number concentration. 6

Figure 2.3 -The over-all effect of step changes in agitation intensity on measured fine drop volume concentration. 7

Figure 2.4 -Possible mechanisms for fine drop recovery. 9

Figure 2.5 -Development of lift force on a particle. 21

Figure 3.1 -View cell used to observe fine drops inside wakes. 27

Figure 3.2 -Schematic of the view cell and camera set-up. 29

Figure 3.3 -Experimental set-up used for measurements of drop recovery rates. 30

Figure 3.4 -Drop concentration measurement location for semi-quantitative experiments. 32

Figure 3.5 -The configuration of the video analysis system. 32

Figure 3.6 -An example video still of fine water drops suspended in sunflower oil+decane (18 times magnification). 33

Figure 3.7 -Examples of initial drop size distributions for the semi-quantitative experiments. 33

Figure 3.8 -Experimental methods of drop injection inside the upper phase. 35

Figure 3.9 -Experimental methods of gas injection into the upper phase. 36

Figure 3.10 -View cell with 4 bubble ports. 37

Figure 3.11 -Rig used for spacial drop concentrations and spacial velocity distributions. ...38

Figure 3.12 -Locations where local velocities and drop concentrations were measured. ... 39

Figure 4.1 -Coalescence between a 5.6 mm diameter water drop and a 500 μm diameter water drop in a continuous decane + sunflower oil phase. 44

Figure 4.2 -Liquid circulation in the upper phase resulting from gas injection through a single injection port at the lower centre of the upper liquid phase. 45

Figure 4.3.a -Over-all fine drop removal by number percent. 47

Figure 4.3.b -Over-all fine drop removal by volume percent. 47

Figure 4.4 -Drop retention in the upper liquid phase (using equations 4.2 and 4.3). 49

Figure 4.5 -Drop retention in the upper liquid phase (Standard settling method, experimental results). 49

Figure 4.6 -The reproducibility of the bottom-center single bubbling injection port experiments, superficial gas flux = 2×10^{-4} m/s) 50

Figure 4.7 -The impact of gas bubble induced circulation loops in the upper liquid phase on fine drop recovery (semi-quantitative results of measurements at one location inside the upper liquid phase). 52

Figure 4.8 -The impact of large drop induced circulation loops in the upper-liquid phase on fine drop recovery(semi-quantitative results of measurements at one location inside the upper liquid phase). 53

Figure 4.9 -Experimental results of spacial velocity distribution in the right half of the upper liquid phase. 55

Figure 4.10 -Vertical (center line) development of bubble velocity ($v_{b\,max}$ =175 mm.s^{-1}) .. 55

Figure 4.11 -Local upper liquid vertical velocities. 56

Figure 4.12 -Local upper liquid horizontal velocities. 56

Figure 4.13 -The evolution of the percent relative number concentration distribution for 10-110 μm diameter drops across the width of the cell (Single bubbling port at the bottom-center of the upper phase, superficial gas flux = 2×10^{-4} m/s). 58

Figure 4.14 -The evolution of the percent relative number concentration distribution for 20 μm diameter drops across the width of the cell (Single bubbling port at the bottom-center of the upper phase. superficial gas flux = 2×10^{-4} m/s). 59

Figure 4.15 -The evolution of the percent relative number concentration distribution for 40 μm diameter drops across the width of the cell (Single bubbling port at the bottom-center of the upper phase, superficial gas flux = 2×10^{-4} m/s). 60

Figure 4.16 -The evolution of the percent relative number concentration distribution for 60 μm diameter drops across the width of the cell (Single bubbling port at the bottom-center of the upper phase, superficial gas flux = 2×10^{-4} m/s). ... 61

Figure 4.17 -The evolution of the percent relative number concentration distribution for

80 μm diameter drops across the width of the cell (Single bubbling port at the bottom-center of the upper phase, superficial gas flux = 2×10^{-4} m/s). 62

Figure 4.18 -The evolution of the percent relative number concentration distribution for 100 μm diameter drops across the width of the cell (Single bubbling port at the bottom-center of the upper phase, superficial gas flux = 2×10^{-4} m/s). 63

Figure 4.19 -Overall relative number concentration contours for drops between 10 and 110 μm in diameter in right half of the upper liquid phase (15 min. after starting mild agitation). 64

Figure 4.20 -Overall relative volume concentration contours for drops between 10 and 110 μm in diameter in right half of the upper liquid phase (15 min. after starting mild agitation). 64

Figure 4.21 -Relative drop number concentration contours for different size ranges in the right half of the upper liquid phase (after 15 min. mild agitation). 65

Figure 4.22 -The effect of gas flux on the overall recovery of fine drops (number %) as a function of time (center gas injection). 68

Figure 4.23 -The effect of gas flux on the overall recovery of fine drops (volume %) as a function of time (center gas injection). 68

Figure 4.24 -The effect of gas flux on the recovery of different drop size ranges as a function of time (center bubble injection). 69

Figure 5.1 -Experimental velocity distribution inside the upper liquid phase (Gas flux = $2x10^{-4}\ ms^{-1}$). 72

Figure 5.2 -Illustration of linear interpolation in two dimensions. 73

Figure 5.3.a -An annotated sketch of horizontal velocity distribution along the mixing zone boundary. 77

Figure 5.3.b -A comparison between normalized velocity distribution and normalized probability distribution at the point of re-entry of drops from the mixing zone into the circulation loops. 77

Figure 5.4.a -The trajectory of a 100 μm diameter drop in the right half of the upper liquid phase (bandwidth = 2 mm, time to capture = 342 s). 80

Figure 5.4.b -An annotated sketch of bubble induced mixing on the right half of the upper phase. 80

Figure 5.5 -The limiting trajectory of a 100 μm diameter drop, defining the capture zone (shaded area). 81

Figure 5.6 -Trajectories of 100 μm diameter drops and 20 μm diameter drops inside the, a) inner orbits and b) outer orbits. x marks the point of intersections of the trajectories for 20 and 100 μm diameter drops. 82

Figure 5.7 -A comparison between the trajectories of a 100 μm diameter drop, with and without the lift force for the inner and the outer orbit cases. 83

Figure 5.8 -The effect of variation of the parameter mixing bandwidth on the predicted region unaffected by the mixing action of the rising bubbles. 85

Figure 5.9 -The effect of mixing zone bandwidth on the recovery of 100 μm diameter drops using the current model compared with equation 4.3 and experimental results (center bubbling port at a gas flux of 2.0×10^{-4} m/s). 86

Figure 5.10-The effect of variations of velocities on liquid-liquid interface on the recovery of 100 μm diameter drops using the current model compared with equation 4.3 (bandwidth=2mm, gas flux=2.0×10^{-4} m/s). 87

Figure 5.11 -Grid scheme for drop binning. 88

Figure 5.12 -The spacial concentration distribution of 100 μm diameter drops after 30 seconds. The total number of drops left is 9473 (12382 drops initially), bandwidth is 2 mm. 89

Figure A.1 -Structure of the drop trajectory calculation program. 103

LIST OF TABLES

Table 2.1 -Collision efficiencies (E_c) for fine water drops with gas bubbles. 17

Table 3.1 -Physical properties of the liquid-liquid system. 28

Table 3.2 -Sources and purities of chemicals. 28

NOMENCLATURE

$A(r)\,dr$	Fraction of drops with diameters between r and $r+dr$
C	Number of drops per unit volume, m^{-3}
C_a	Constant in added mass force term, dimensionless
C_w	Friction coefficient
d	Drop diameter, m
d_b	Bubble diameter, m
d_p	Particle diameter, m
F_a	Added mass force, $kg.m.s^{-2}$
F_d	Force acting on a drop, $kg.m.s^{-2}$
E_c	Collision efficiency
F_{L_x}, F_{L_y}	Lift force in x-direction, y-direction, $kg.m.s^{-2}$
F_m	Lift force, $kg.m.s^{-2}$
F_s	Friction force, $kg.m.s^{-2}$
F_w	interphase force, $kg.m.s^{-2}$
g	Gas
G	Shear rate, s^{-1}
G_x, G_y	Shear rate component in x-direction, y-direction, s^{-1}
h	Critical rupture thickness of continuous phase film, m
k	Subscript denoting l or g
l	Liquid
N	Total number of drops present per unit volume of dispersion, m^{-3}
P	Dimensionless settling velocity of particle, *equation 2.7.*
r	Drop radius, m
Re	Reynolds number

Re_{L_x}	Shear Reynolds number in x-direction
Stk	Stokes number
t	Time, s
u	Relative velocity of particle or drop to continuous phase in x-direction, $m.s^{-1}$
u_c	Continuous phase velocity in x-direction, $m.s^{-1}$
u_d	Drop velocity in x-direction, $m.s^{-1}$
u_p	Particle velocity in x-direction, $m.s^{-1}$
$\bar{u}_{slip}$	Slip velocity between gas and liquid phase, $m.s^{-1}$
v	Relative velocity of particle or drop to continuous phase in y-direction, $m.s^{-1}$
v_c	Velocity of continuous phase in y-direction, $m.s^{-1}$
v_b	Bubble rise velocity, $m.s^{-1}$
v_d	Drop velocity in y-direction, $m.s^{-1}$
v_g	Gas velocity, $m.s^{-1}$
v_p	Particle velocity in y-direction, $m.s^{-1}$
v_s	Difference between gas and liquid velocities in Y-direction, $m.s^{-1}$
V	Volume of drop, m^3
V_p	Volume of particle, m^3
w	Velocity in z-direction, $m.s^{-1}$
x	Horizontal position, m
y	Vertical position, m
$z(r_1, r_2)dr_1\,dr_2$	Drop collision rate, number of drops of size r_1 and r_2 colliding per unit volume per unit time, $m^{-3}.s^{-1}$

GREEK LETTERS

ε	Energy dissipation per unit mass, $m^2.s^{-3}$
ε_g	Volume fraction of gas
η	Kolmogorov microscale, m
ρ_c	Density of the continuous phase, kg / m^3
ρ_d	Density of the dispersed phase, kg / m^3
ρ_p	Density of the particles, kg/m^3

μ_c	Viscosity of the continuous phase, $Pa.s.$
μ_d	Viscosity of the dispersed phase. $Pa.s.$
υ	Kinematic viscosity, m^2/s
σ_c	Continuous phase surface tension, N/m
σ_d	Dispersed phase surface tension, N/m
σ_i	Liquid-liquid interfacial tension, N/m
ω	Frequency of oscillation, s^{-1}
$\bar{\bar{\tau}}$	stress tensor, N/m^3

1 INTRODUCTION

Batch gas-agitated liquid-liquid systems are found in diverse contexts: metallurgical reactors (nickel and copper converters, slag cleaners); oil slick dispersion/emulsification in breaking waves, to cite but two examples. Despite their importance, the hydrodynamics of such systems has received comparatively little attention in the open literature (Hatzikiriakos et al., 1990 a & b; Shaw and Konduru, 1992 and Shahrokhi and Shaw 1994). Batch gas-agitated liquid-liquid systems possess diverse geometries but operate on the same basic principle. As illustrated in Figure 1.1, two immiscible liquids form stratified layers initially and return to this stratified state at the end of a batch. Liquid from the lower liquid phase is entrained and then dispersed by gas bubbles passing from the lower to the upper liquid phase. Over time a number of possible phase distributions arise depending on the ratio of the two liquid phases in the vessel and the physical properties of the fluids e.g. emulsions or dispersions (Konduru and Shaw,

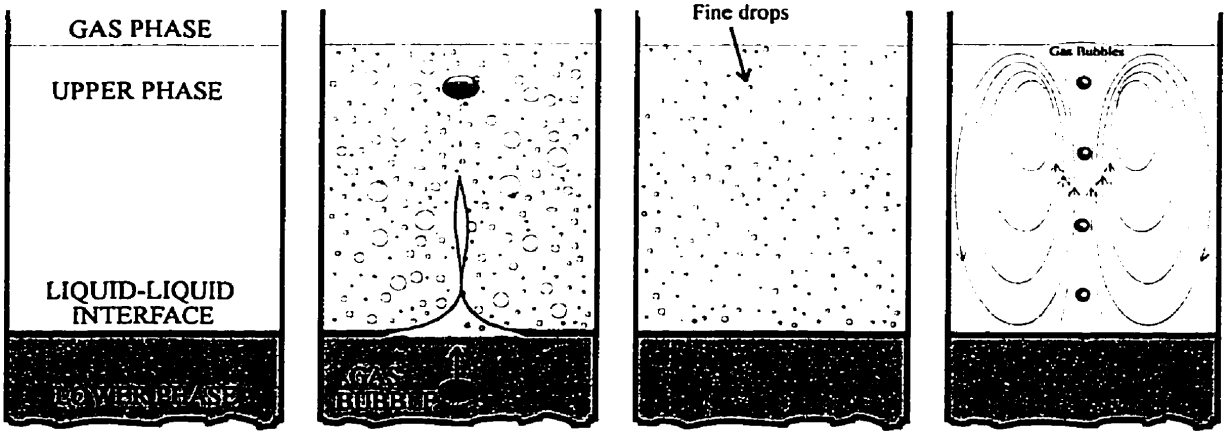

Figure 1.1 -The formation and evolution of batch gas-agitated liquid-liquid dispersions.

1990). At the end of a batch, agitation is stopped and the liquids separate under the influence of gravity. Fine drops separate slowly and consequently, a small amount of the more dense liquid phase remains dispersed in the less dense liquid phase in the form of fine drops long after agitation has ceased and the bulk liquid phases have separated. For industrial scale processes such as copper and nickel conversion, long settling periods reduce equipment productivity and entrained metal drops reduce metal yield, which has sparked interest in slag cleaning and other remedial measures.

The separation of suspended drops or particles is a common processing step applied on a huge scale in the chemical, mining and metallurgical industries, as well as in environmental emission control operations. Gravity, which is relatively ineffective when the drops or particles are small or have densities only slightly greater than the fluid, is the usual driving force. As a result, suspensions are left in very large diameter settling vessels and for long periods of time. Maintaining a large settling vessel can be costly, specially if the fluid is a valuable one. Any practical means of accelerating separation rates would be beneficial in reducing the size of new separation equipment and improving through put of existing vessels. Standard techniques for improving settling/separation rates such as the insertion of surfaces (Sharifi and Shaw, 1996), addition of flucculants and/or a second buoyant particulate phase (Weiland and McPherson 1979) are not applicable as limitations concerning the utilization of external objects and complicated structures for settling vessels are encountered particularly in metallurgical applications. Therefore improvements in recovery rates for fine drops must be realized by other techniques.

Based on previous studies (Shahrokhi 1993) and anecdotal industrial information, matte or metal drop recovery rates from slags can be improved in such cases by injecting streams of gas bubbles into the vessels, at moderate gas fluxes, once the principal agitation is stopped e.g.: at the end of a batch, and this has become part of standard industrial practice. However, an explanation for this phenomenon has been lacking and consequently it has not been possible to identify clear optimisation strategies.

1.1 Objectives

Over the past four years fine drop recovery in batch gas-agitated liquid-liquid dispersions has been explored both experimentally and computationally.

The specific objectives of the present work are:

1. To show how fine drop recovery rates from batch gas-agitated liquid-liquid dispersions can be improved by gas injection.

2. To identify the mechanisms for the recovery of fine lower liquid phase drops in batch gas-agitated liquid-liquid dispersions.

3. To show how passing bubbles through the upper liquid phase and the physical properties of the two liquids affect the recovery of fine drops.

4. To improve methods for the recovery of fine lower liquid phase drops suspended in the upper liquid phase of batch gas-agitated liquid-liquid dispersions.

2 LITERATURE REVIEW

2.1 Fine drop generation

Mass and heat transfer between two liquids is usually enhanced by dispersing one phase as drops in a second continuous phase. Numerous contacting devices have been developed expressly for this purpose. The most common contactors are continuous mechanically-agitated columns and bubble-agitated columns. Batch gas agitated liquid-liquid contactors have received comparatively little attention in the open literature (Sharifi and Shaw 1996, Shahrokhi and Shaw 1994, Shaw et al. 1992, Hatzikiriakos et al. 1990, Konduru and Shaw 1990).

In batch gas-agitated liquid-liquid contactors, the denser liquid is entrained into the less dense liquid by bubble passage through the liquid-liquid interface. As a bubble passes through the liquid-liquid interface a column of lower liquid is entrained. This column is stretched and then disintegrates. Fine drops are generated mainly in the necked region adjacent to the rising bubble and near the liquid-liquid interface but the finest drops are produced near the bubbles where the rate of extension is greatest. Close-up views of the region close to the bubble are shown in Figure 2.1 for a liquid-liquid viscosity ratio of 0.062 (Shahrokhi and Shaw, 1994). The column disintegration is not uniform and is characterised by the formation of large drops connected by thin filaments, which on further extension develop a secondary varicosity and disintegrate, leaving a myriad fine drops between the larger principal drops. At the end of the batch, the drops dispersed in the upper liquid phase return to the lower liquid phase.

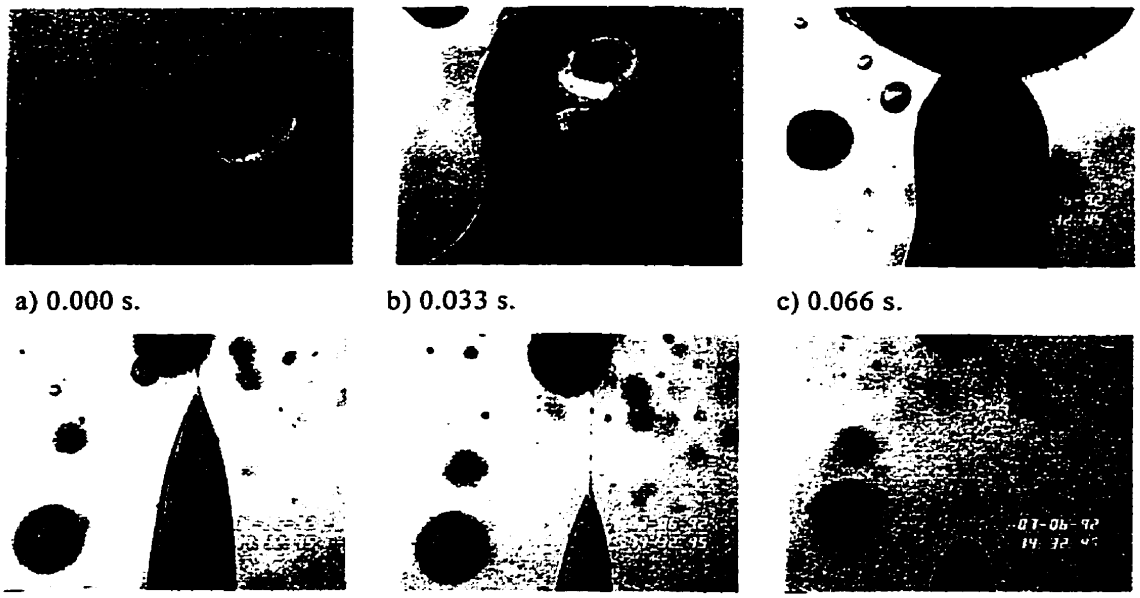

Figure 2.1 - Fine drop production at the liquid-liquid interface for a viscosity ratio case (0.063). The width of each frame is 4.5 mm: (a) the bubble approaches the interface; (b) the bubble stretches the interface and pushes a thin film of lower liquid phase; (c) the film peels off the bubble and a column of the lower phase is pulled up in the wake of the bubble; (d) the column of the lower phase liquid thins just below the bubble; (e) and (f) the necked region adjacent to the bubble disintegrates to produce fine drops. (Shahrokhi and Shaw 1994)

Experimental data on drop generation in liquid-liquid systems are sparse and have been confined mostly to mechanically agitated vessels at low volume fractions of the dispersed phase. Recently, Shahrokhi and Shaw (1994) reported that fine drops in gas-agitated liquid-liquid systems are generated by three distinct sources: the disintegration of liquid columns entrained by gas bubbles as they cross the liquid-liquid interface, drop breakage during collisions with gas bubbles and multiphase drop rupture at the upper liquid-gas interface. They showed that while multiphase drop rupture produces the finest drops, the relative importance of each of these mechanisms is affected by the physical properties of the liquid phases and system operating conditions.

2.1.1 Prior experimental work (Shahrokhi and Shaw, 1994)

The recovery of fine drops from a dispersion of water in oil using a low gas flux was investigated by Shahrokhi and Shaw in 1994. Experiments were performed in a rectangular perspex column filled with stratified layers of sunflower oil+decane over an aqueous sugar solution. During the experiments, a dilute dispersion of the lower phase was generated inside the upper phase by introducing large nitrogen gas bubbles into the aqueous phase for 30 minutes with a gas flux of 0.026 m/s. The gas injection was then reduced to a lower gas flow rate to evaluate fine drop recovery under new conditions. This experiment was repeated for four different low gas flow fluxes.

Figure 2.2 shows an overview of the effect of four different step changes in the gas flux, on the concentration of fine drops between 10 and 110 μm in diameter. As this figure

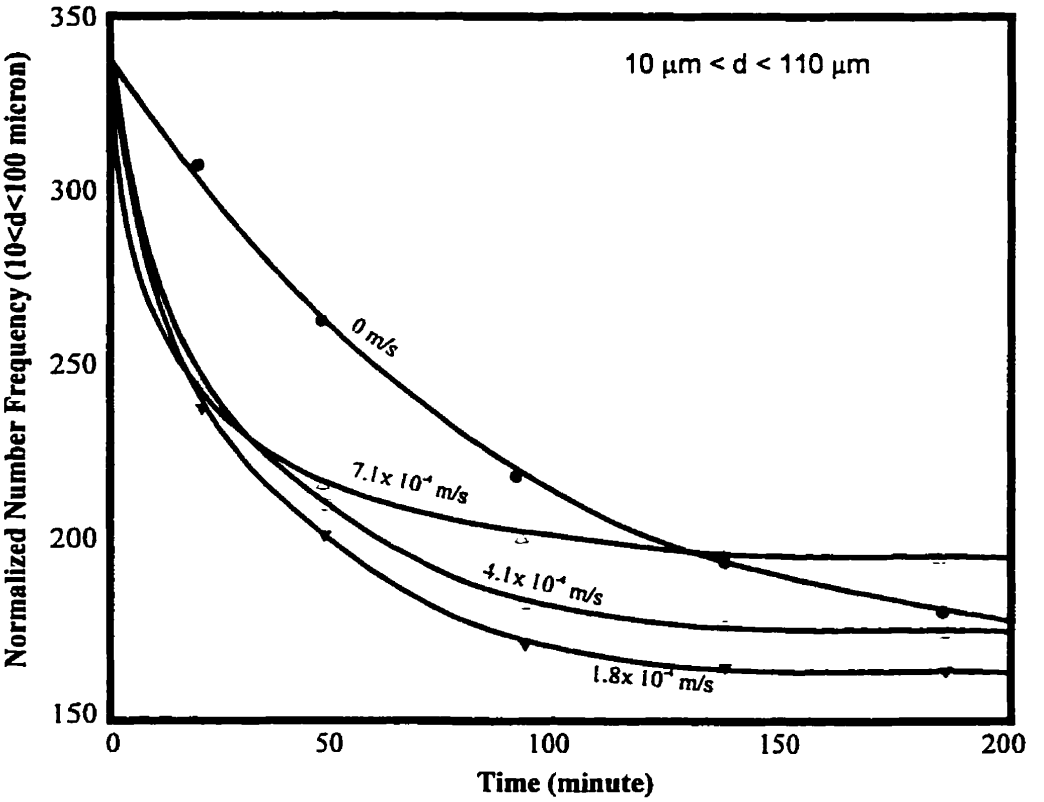

Figure 2.2 -The over-all effect of step changes in agitation intensity on measured fine drop number concentration.

shows, the new steady state conditions for each gas flow rate was achieved almost 2 hours after applying each step change. This figure also shows that almost any gas flux gives the same drop recovery result during the first 20 minutes. Figure 2.3 represents the same set of experiments based on the volume concentration of dispersed drops. A 4.1×10^{-4} *m/s* gas flux provides the best recovery of fine drops, by volume percent after the same time interval.

It should be noted that during mild agitation fine and large drops are still introduced into the upper phase as gas bubbles cross the liquid-liquid interface. In order to prevent production of fine drops, other means such as introducing bubbles directly into the upper liquid phase must be considered.

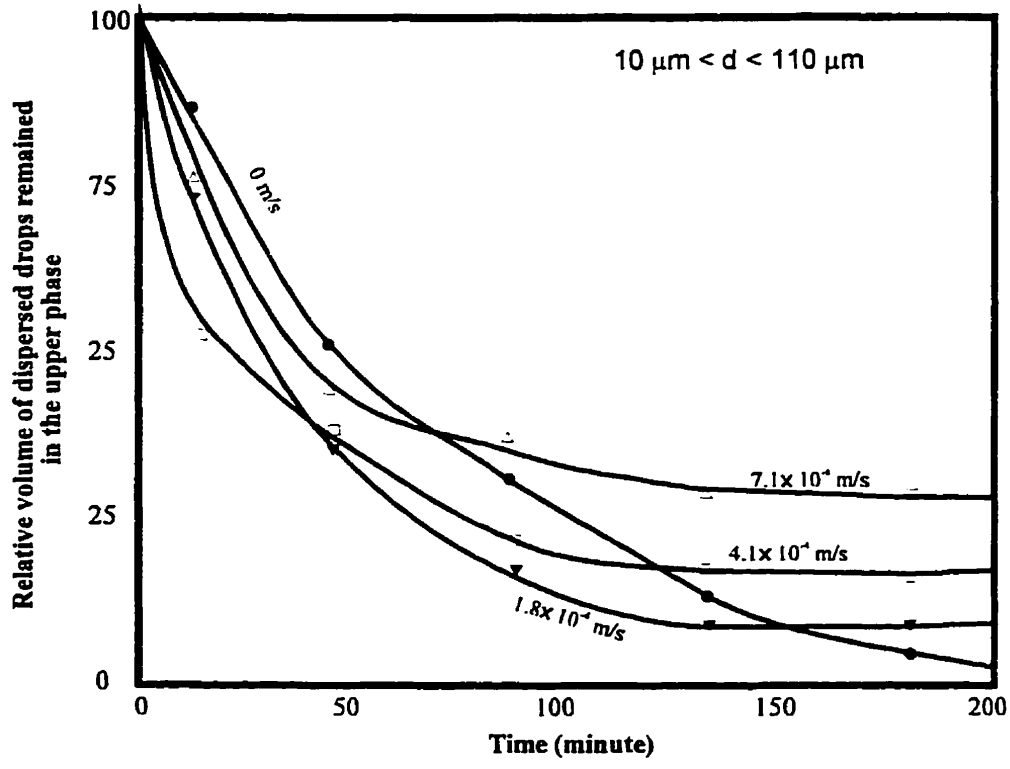

Figure 2.3 -The over-all effect of step changes in agitation intensity on measured fine drop volume concentration.

2.2 Possible mechanisms for fine drop recovery

The coalescence of two drops is accompanied by the draining and rupture of the film of the continuous phase separating them. When drops come into physical contact, they coalesce into a single but larger drop to minimise the surface area and surface energy of the contacted drops (Melik 1984). When drops approach one another, the mobility of their interfaces allows the fluid between them to be squeezed outward with much less resistance than for the rigid particle case. However, in a dynamic situation like drops colliding in a mixing vessel, there is the additional complication of a required contact time that depends on the physical properties and the kinematics of the collisions. As discussed by Davis, Schonberg & Rallison (1989), this allows for non-zero collision rates of non-deforming drops, even in the absence of attractive forces. At a flat interface, thinning eventually leads to coalescence, but this is not necessarily true for drops colliding in turbulent dispersions. Key factors affecting the coalescence process have been summarised by Jeffrey and Davies (1971).

The rate of coalescence between drops is a direct function of collision efficiency and the collision frequency between drops. Coulaloglou and Tavlarides (1977) described coalescence frequency as the product of the collision efficiency and the coalescence efficiency. Hatzikiriakos et al. (1990) presented a summary of collision frequency predictions, drop rupture and drop-drop coalescence in gas-agitated liquid-liquid dispersions. They noted that coalescence efficiency is assumed to be unity or less, and there is always a discrepancy between predicted and measured values. The frequency of contact between drops in turbulent flows increases substantially in comparison with the number of encounters in a motionless medium or in laminar flow. It should be noted that gravity can play an important role in determining collision rates for systems with large density differences. In turbulent liquid-liquid dispersions with small fluid density differences, gravity is not an important factor in determining collision rates.

As mentioned before, the focus of this work is on the recovery of drops sufficiently small (typically having diameters of 100 μm and less) that they remain spherical due to

their interfacial tension, and their inertia is small relative to viscous forces. Possible mechanisms that lead to drop recovery for this size range of drops include:

-Large drop-small drop coalescence
-Drop-liquid interface coalescence
-Drop-drop coalescence in eddies
-Drop recovery by flotation

2.2.1 Large drop-small drop coalescence

The contact between large and small drops under gravity arises if there is a significant difference between their velocities (Figure 2.4.a). For gravity-induced coalescence of drops with hydrodynamic and inter-drop forces, theoretical models have been developed by Davis (1984) and by Melik & Fogler (1984) to predict the rate of coalescence using trajectory analysis, and by Wen & Batchelor (1985) using an asymptotic method for solving the convective-diffusion equation. All of these studies show that the hydrodynamic resistance to relative motion for small drops in the same size range, causes the collision rates to approach zero as the attractive forces become insignificant. On the other hand, Zinchenko (1982) calculated the rate of gravity-induced coalescence of spherical drops of different sizes numerically, using a trajectory analysis for pairs of drops, without considering the effect of inter-drop forces. His results confirmed that, in

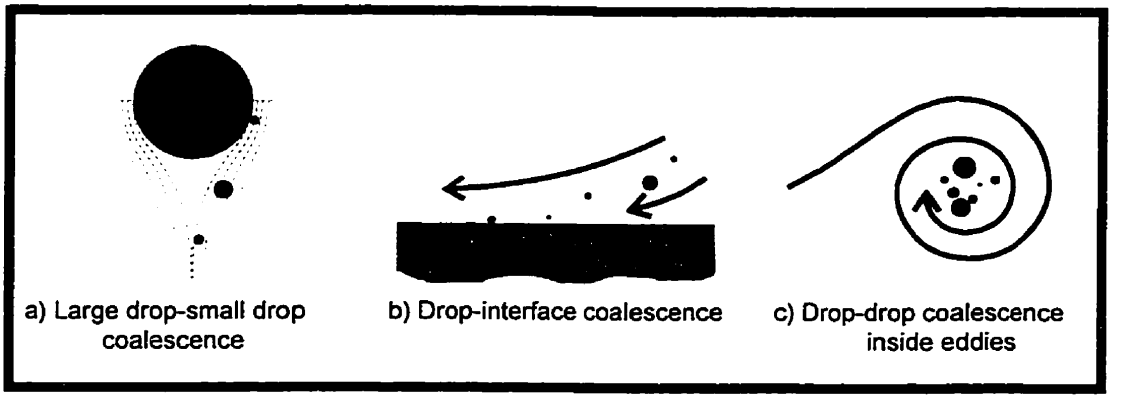

Figure 2.4 -Possible mechanisms for fine drop recovery

contrast to rigid spheres, drop collision is possible at finite rates under the action of a finite external force only. He also showed how the rate of drop collisions decreases with an increasing viscosity ratio between the drop and the continuous phase.

The other possibility of contact between two drops is when drops are moving in a medium with a velocity gradient. A simple example of such motion is laminar flow near a liquid-liquid interface. It is not difficult to see that the existence of the velocity gradient leads to contacts between drops of finite radius. A drop situated far from the interface moves with greater velocity than a drop situated close to the interface. If the distance between the two drops does not exceed the sum of their radii, the drops can collide.

2.2.2 Drop-interface coalescence

Fine drops may reach the horizontal interface between the two phases due to the circulation inside the upper phase (Figure 2.4.b). Drops approaching the interface may also collide with drops present on the interface. This may cause them to "bounce" or coalesce. Collision at low relative velocities, being associated with initially small film areas, are more likely to lead to coalescence than collisions at high relative velocities. In the former case, drops stay together for a longer period of time, i.e. enough time for the thinning film to rupture. In the latter case, the possibility of bouncing increases because of the greater surface distortions. Thus calmer regions i.e. zones far from the bubble street are suitable sites for this mechanism to be effective. The only difference between drop-interface coalescence and drop-drop coalescence is the time that is available for coalescence. Drops sitting on the interface stay in contact until coalescence occurs. In the drop-drop coalescence case, drops may be separated due to pressure fluctuations or velocity gradients in the continuous fluid and contact may or may not result coalescence.

It is well established that most of the time required for coalescence is the time needed for film drainage. Once the film has ruptured, coalescence is effectively instantaneous except that sometimes a secondary droplet is formed (Charles & Mason 1960). MacKay

& Mason (1963) found that the film thickness at the time of rupture is about 0.5 to 1 μm for drop diameters up to 2.5 mm sitting on a flat interface. Thomas (1981) estimated the critical film thickness to be about 0.24 μm in turbulent flow. Jones et. al. (1978) made similar estimations based on simple lubrication theory and accounted for the effects of circulation induced in the drop and the lower bulk fluid, which tends to speed up drainage, and the constriction in the film thickness at its periphery, which tends to slow it down. They calculated the minimum thickness explicitly in a film drainage problem for deformable and rigid spheres.

2.2.3 Drop-drop coalescence in eddies

The mechanism concerning encounters between drops suspended in a laminar fluid, as discussed in section 2.3.1, has very limited application in practice. In a turbulent flow, small drops follow the behaviour of the fluid eddies very closely. Drops larger than the microscale of turbulence (Kolmogoroff length scale $\eta = (\upsilon^3/\varepsilon)^{1/4}$) follow the mean flow. In turbulent flow, drops smaller than the microscale of turbulence collide with each other within eddies, and if they remain together for a long enough time, drops coalesce. In this case, the dynamics of the intervening film is then the same as for a film trapped between two drops in the stationary case. Shinnar (1961) proposed that there is a minimum drop diameter below which the eddies do not separate colliding drops and therefore do not prevent their coalescence. Thomas (1981) studied this case. He assumed that drainage takes place between bubbles steadily pressed together for a period due to pressure fluctuations. Based on dimensional analysis, he concluded that bubbles whose diameter exceeds

$$d_b \sim 2.4\left(\frac{\sigma_c^2 h^2}{\mu_c \rho_c \varepsilon}\right)^{1/4} \qquad 2.1$$

are much less likely to coalesce than smaller bubbles in a dispersion. He also found that

if energy dissipation rate (ε) exceeds a critical value, it is no longer possible to have coalescence in the mixing region.

The dependence of coalescence on σ_c , ρ_c, and μ_c cannot be deduced directly from equation 2.1 because the variation of h (the critical rupture thickness) with physical properties is unknown. Calderbank (1958), in a series of experiments on liquid-liquid and gas-liquid dispersions, found a weak dependence of maximum bubble size on continuous-phase viscosity. Pavlushenko and Yanishevkii (1959) in a set of stirred-tank experiments, found a weak inverse dependence of maximum bubble size on continuous-phase viscosity. Although there is some support in the literature for the viscosity dependence given by equation 2.1, the experimental evidence is not conclusive.

The collision of drops smaller than the microscale of turbulence is caused by two independent and essentially different mechanisms. These mechanisms differ depending upon whether drops have the same density or a different density from that of the surrounding fluid. Drops that have essentially the same density as the surrounding fluid follow the motion of that fluid completely. Thus, drop velocity fluctuations can be described by the continuous fluid velocity fluctuations. Under these conditions Saffman and Turner (1956) obtained the following expression:

$$z(r_1,r_2)dr_1\,dr_2=(8\pi/15)^{1/2}(r_1/2+r_2/2)^3\,(\varepsilon/\upsilon)^{1/2}\,NA(r_1)NA(r_2)dr_1\,dr_2 \qquad 2.2$$

where $z(r_1,r_2)dr_1\,dr_2$ is the number of binary collisions between drops of sizes r_1 and r_2 per unit volume of dispersion per unit time, N is the total number of drops of all sizes present per unit dispersion volume, $A(r_1)dr_1$ is the fraction of drops with diameters between r_1 and r_1+dr_1 and $(\varepsilon/\upsilon)^{1/2}$ is the turbulent velocity gradient. This equation shows a direct relation between collision frequency and energy dissipation rate and also an inverse relation with the kinematic viscosity of the continuous phase.

The second collision mechanism comes about only if there is a significant difference

between the densities of the fluid and the drops. Because of this significant difference, drops with different diameters move with different velocities, which results in collisions between them. Researchers East (1954), Levich (1962) and Pancher (1971) have accounted for this "acceleration collision" mechanism in their derivation of collision expressions for drops in air.

Contact between drops inside an eddy occurs on a scale less than the size of the eddy and arises when the drops are very small or the density difference between phases is small. Once a set of drops is trapped inside an eddy, the likelihood of coalescence is increased since the motion of the eddy does not separate them. The micro scale length (η) in the wake of a 4 mm bubble is about 450-500 μm which is large enough to carry drops in the size range of interest here. Figure 2.4.c shows this type of interaction schematically.

2.2.4 Drop recovery by flotation

Flotation processes are used widely throughout industry to remove solid particles from water. Bubbles and particles must come into physical contact for flotation to occur. Gas bubbles can generally overtake particles suspended in water. This leads to the possibility of bubble-drop contact in gas liquid-liquid contactors. Numerous studies have been made on flotation of solid particles more dense than water. Particle/water separation is slightly different from water/oil separation because of the difference between surface properties of solids and fluid drops. Nevertheless, some of the results of these studies can be extrapolated to liquid drops. Basically, it is important to know what parameters govern the contact. Flint and Howarth (1971) have calculated the collision efficiency of a single bubble rising in an infinite field of water containing a uniform spatial distribution of particles. Their results show that for small particles where inertia is unimportant (and this is the case for water drops smaller than 700 μm in collision with a 10 *mm* gas bubble) collision does not occur. However, they considered the particles to be point masses with no physical dimensions. Thus, their definition of collision is when the trajectory of the centre of the particle intersects the bubble surface. This omits the

possibility of oblique or acute collision caused by a particle's surface contacting the bubble as its centre passes near the bubble.

For the flotation process to be successful, drops must attach to gas bubbles after collision and must remain attached. The process is extremely complex because it involves hydrodynamics and surface chemistry. Once attached, the accumulation of drops on the surface of bubble may lead to coalescence between them. Flow around the bubble exerts tangential shear forces that tend to cause detachment, while the surface forces at the interface oppose this. Once the drops grow in size this shear force imposes higher tangential stress on attached drops to overcome the attachment force and larger drops are released.

2.3 Evaluation of proposed mechanisms

2.3.1 Large drop-small drop coalescence

Drops with different diameters move with different velocities, which can result in contact between them. The terminal velocity of small drops in stagnant medium is given approximately by Stokes equation:

$$v_d = \frac{2}{9} g \frac{{d_d}^2}{\mu_c} (\rho_c - \rho_d) \qquad 2.3$$

Based on this equation a 10 μm diameter water drop suspended in a continuous oil phase with 0.0047 $Pa.s$ viscosity and 184 kg/m^3 density difference, can travel 7.6 cm in about 2.5 hours whereas a drop with a 100 μm diameter travels the same distance in about 1.5 minutes. Therefore a larger drop with higher terminal velocity may come into contact with a smaller drop especially when the distance between their trajectories is less than the radius of the larger drop (Figure 2.4.a). In this case, the small drop with less inertia is carried along by forces of hydrodynamic interaction in the flow of liquid bending around the surface of larger drop which depends on the inertia forces of small drop, may reach

the surface of the larger drop.

The mechanism for contact between a small and a large drop is the same as the contact between fine particles and rising bubbles in flotation processes. In these types of processes the inertial forces are also small. Hence, under the influence of the hydrodynamic forces, the particles deflect from the rectilinear path in such a way that the trajectories coincide with the liquid streamlines around the bubble.

The inertial parameter, Stokes number:

$$Stk=\frac{2\rho_p d_p^2 v_b}{9 d_b \mu_c} \qquad 2.4$$

is the criterion allowing one to determine when inertial forces can be neglected (Noll (1970), Weber (1981) and Anfruns (1977)). It is usually assumed that when $Stk<0.1$, then inertial forces do not affect the deposition of the particles on the bubble surface. Flotation can proceed in such cases by the interception of particles. From the theory of flotation of fine particles, it can be assumed that the interaction between a large falling drop and a micron size drop should proceed according to the model of inertialess interception. In the cases studied in this work, the Stokes number values calculated are much smaller than the critical value of 0.1. The results of experiments performed concerning this mechanism are presented in chapter 4.

2.3.2 Drop-drop coalescence in eddies

Drop-drop coalescence inside eddies is limited to drops with a very low inertia force and also in the absence of surfactants. The restriction comes from the instability of eddies and their short life time which have a great effect on the time available for the drops to come into contact and coalesce. This mechanism, although it seems to be plausible, is

difficult to assess. The results of experiments performed concerning this mechanism are presented in chapter 4.

2.3.3 Drop-interface coalescence

Drop interface interaction is limited to drops with an inertia force, when the density difference between the dispersed phase and the continuous phase is significant. The possibility of contact comes from the calm regime close to the interface that allows fine drops to come into close contact with the interface. Large drops with greater inertia are expected to be recovered faster than smaller drops under this mechanism. Chapter 4 shows how this mechanism occurs and quantifies its impact on fine drop recovery.

2.3.4 Drop recovery by flotation

Reay and Ratcliff (1973) performed an analysis for the case where particle inertia is unimportant, and they included the effect of particle size. They considered both the particles and the bubble to be in the Stokes' flow regime. They calculated the collision efficiency to be

$$E_c = \frac{K^2}{(1+P)}(1 + P - \frac{3}{2K} + \frac{1}{2K^3}) \qquad 2.5$$

where

$$K = 1 + d_p / d_b \qquad 2.6$$

and P is

$$P = 2d_p^{\,2} g(\rho_p - \rho_c) / 9 v_b \mu_c \qquad 2.7$$

Values of E_c calculated for three drop sizes and three bubbles sizes are shown in Table

4.1. These results show that collision efficiency increases dramatically as drop size increases and as the bubble size decreases. For example, the efficiency of collision of a 0.5 mm gas bubble with a 100 μm diameter water drop is about 27 times greater than with a 20 μm diameter drop. Correspondingly, the efficiency of collision of a 20 μm diameter water drop with a 0.05 *mm* gas bubble is about two orders of magnitude greater than with a 0.5 *mm* gas bubble. Clearly, it is desirable to have large drops and small bubbles to increase collision efficiency.

Gas bubble diameter		Water drop diameter (μm)		
(*mm*)	*Re*	20	60	100
0.05	0.003	0.438	3.508	8.064
0.10	0.021	0.105	0.987	2.559
0.50	2.602	3.9×10^{-3}	0.037	0.105

Table 2.1 -Collision efficiencies (E_c) for fine water drops with gas bubbles

Reay and Ratcliff (1973) have shown from their analysis that the recovery rate should be proportional to $1/d_b^3$. Their analyses were based on the assumption of Stokes' flow which in fact is valid only for bubbles less than 1.0 mm in diameter. Thus, the values of collision efficiency obtained from Equation 2.5 are not accurate for the larger bubble size. These calculations are also limited to single bubbles and neglect the influence of adjacent bubbles. Flint and Howarth (1971) have shown that the collision efficiency of a bubble can be increased several times by the influence of adjacent bubbles. This is because adjacent bubbles force the streamlines closer to the bubble surface. Therefore, the effect of adjacent bubbles is to increase collision efficiency.

Clearly fine drop recovery under this mechanism necessitates a large flux of small bubbles. In this work only large bubbles (3.5-4.5 mm in diameter) are employed. Thus

bubble-drop interaction is unlikely to contribute significantly to fine drop recovery.

2.4 Bubble driven flow

Computational fluid dynamics is an important tool in the investigation of multi-dimensional two-phase flow. Phenomenological models have been used widely to describe such flows, but these models are not well suited for scale up and design in general, since they require prior knowledge of the flow structure. For single-phase flows, basic knowledge of simple flow is available from analytical and/or numerical solutions of the fluid mechanics equations. These solutions are supported and/or extended by experimental results yielding basic information on momentum transport in single-phase flows. Such information is not available to the same extent for two phase flows because analytical and/or numerical treatments of the basic two-phase flow equations are not readily available. This applies to two-phase flows in general and to bubble-driven liquid flows in particular. Because of this, bubble-driven liquid flows are not readily predicted.

Since no mass exchange is considered between gas and liquid, the continuity and momentum balance equations can be formulated for both phases independently without an exchange term:

$$\frac{\partial(\varepsilon_k \rho_k)}{\partial t} + \nabla.(\varepsilon_k \rho_k \vec{u}_k) = 0 \qquad 2.8$$

$$\frac{\partial(\varepsilon_k \rho_k \vec{u}_k)}{\partial t} + \nabla.(\varepsilon_k \rho_k \vec{u}_k \vec{u}_k) = \varepsilon_k \nabla.\vec{\vec{\tau}}_k - \varepsilon_k \nabla p + \varepsilon_k \rho_k \vec{g} \pm \vec{F}_w, \qquad 2.9$$

where $k = l, g$

The only difference between the two phases is the sign of the force term $\vec{F}_w$ which is positive for the gas phase and negative for the liquid phase. The first term on the right hand side of Equation 2.9 considers the molecular momentum transfer of laminar flow

where

$$\bar{\bar{\tau}}_k = \mu_k (\nabla \vec{u}_k + \nabla \vec{u}_k^t) \qquad 2.10$$

Because of the difference in the densities ρ_l and ρ_g, a gravity term must be considered in each phase. Buoyancy effects, leading to a slip between the two phases, are a result of the coupling of both phases through a pressure balance.

2.4.1 Interphase force term

The force term $\vec{F}_W$ describes the forces between the continuous phase and gravity forces acting on motionless bubbles and particles in a motionless liquid. Since there is usually a relative motion between bubbles and the liquid, the liquid flow around individual bubbles leads to local variations in pressure and shear stress. The resulting interaction forces due to these variations cannot be considered in detail within the framework of a two fluid model but have to be approximated through more or less empirical correlations. Usually three different contributions for the interaction force term are taken into account: a friction force term $\vec{F}_s$, an added mass force term $\vec{F}_a$, and a lift force term $\vec{F}_m$, leading to the following approximation for the force of the interaction:

$$\vec{F}_W = \vec{F}_s + \vec{F}_a + \vec{F}_m . \qquad 2.11$$

The three contributions are discussed briefly in the following subsections.

2.4.1.1 Friction force

A bubble that moves relative to a liquid accelerates part of the liquid around it and is in turn slowed down by the surrounding liquid. The friction force is the dominant force contribution and often it is the only one considered. It is common to describe the friction force $\vec{F}_s$ as

$$\vec{F}_s = -\varepsilon_g C_w (\vec{u}_g - \vec{u}_l) \qquad 2.12$$

where C_w is a friction coefficient for which a large number of correlations can be found in the literature, depending upon whether single bubbles or bubble swarms in stagnant or moving liquid are considered (Johansen, 1990). In general C_w depends upon the bubble size but this dependence is weak for air bubbles of 1-10 mm mean diameter in water. According to Schwarz and Turner (1988), the single value $C_w = 5 \times 10^4$ kg/m^3s can be used, leading to a mean bubble slip velocity of about 20 cm/s, which agrees well with experimental values of air bubbles in tap water.

2.4.1.2 Added mass force

The friction force takes account of the interaction forces between liquid and bubbles in a uniform flow field under non-accelerating conditions. If however the bubbles are accelerated relative to the liquid, part of the surrounding liquid has to be accelerated as well. Typical examples include the flow fields at the upper and lower end of a loop reactor. This additional force contribution is called the "added mass-force" and can be calculated from the additional force of acceleration as

$$F_a = -\varepsilon_g C_a \rho_l \frac{D(\vec{u}_g - \vec{u}_l)}{Dt} \qquad 2.13$$

where a number of different correlations can be found for C_a in the literature (e.g. Rietema, 1982). If the volume fraction of the dispersed phase is low, C_a = 0.5 is a common value. Cook and Harlow (1986) calculated this coefficient for a bubble volume fraction of 2.82 % (2 mm bubble radius) and they found that the value C_a = 0.25 is in good agreement with the measurements of Hulin et al. (1982). They recommended C_a = 0.5 only for drops with a rigid surface and this is the value used in the model (chapter 5).

2.4.1.3 Lift force (Magnus force)

If a drop with a rigid surface moves in a non-uniform flow field, the flow field may

induce drop rotation which in turn causes an additional force of interaction, perpendicular to the main flow direction. (The well known ping-pong ball, balancing on top of an air jet, is a typical example.) The lift force, often also referred to as "Magnus force", can be approximated for the case of potential flow as (Thomas et al., 1983)

$$\vec{F}_m = -\varepsilon_g C_m \rho_l (\vec{u}_g - \vec{u}_l) \times (\nabla \times \vec{u}_l) \qquad 2.14$$

The Magnus force has recently been used in the modeling of bubble columns to account for the experimentally well documented effect that in a uniformly aerated bubble column the rising bubbles tend to accumulate in the center of the column (Torvik and Svendsen, 1990; Grienberger and Hofmann, 1992; Svendsen et al., 1992; Jakobsen et al., 1993; Hillmer et al., 1994).

If a particle with a rigid surface is not neutrally buoyant then its speed will be different from that of the fluid thus giving rise to a "shear" lift. Figures 2.5.a-b show the cases when the particle is heavier than the fluid i.e. $\rho_p > \rho_c$ in upflow and downflow respectively. The terminal velocity is against the main flow in the upflow and with the

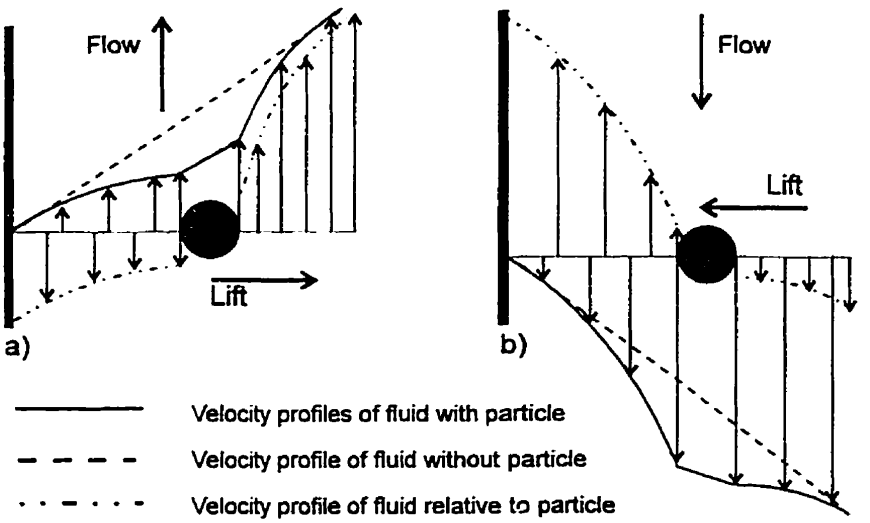

Figure 2.5- Development of lift force on a particle (Oshinowo 1972).

flow in the downflow. The resultant velocity of liquid relative to the particle is such that a pressure gradient is created and the "shear" lift on the particle is away from the wall in upflow and toward the wall in downflow (Oshinowo 1972).

2.4.2 Loop reactors and locally aerated bubble columns

In loop reactors, on the other hand, the fluid motion is a result of the feed momentum and of density differences between the aerated and the non-aerated parts.

2.4.2.1 Momentum balance for the gas phase

The flow pattern in gas driven liquid-flow depends directly upon the gas flux into the reactor. For the fluid flow, the gas velocity, as given by the gas momentum balance is of prime importance. However it is quite common to use different simplifications of the gas momentum balance. Usually the balance is only considered, in its quasi-steady state form since, due to the small gas density, the inertia force for the gas bubbles can safely be neglected against other terms in the gas momentum balance at low to medium pressure.

Different simplifications exist primarily with respect to the interphase force term. The added mass force term is often neglected since it is assumed that the slip velocity between both phases is constant. The lift force is also usually neglected since its physical importance for gas bubbles with a non-rigid surface is still unclear. An exception is the use of the Magnus force with the wrong sign in the simulation of bubble columns (section 2.4.1.3).

If the inertia force, the lift force and the added mass force are all neglected, the gas momentum balance turns into the well known slip relation

$$\vec{u}_g = \vec{u}_l + \vec{u}_{slip} \qquad 2.15$$

where the slip velocity $\vec{u}_{slip}$ between the two phases is either assumed constant or

calculated from the pressure gradients with a given friction coefficient C_w. Different correlations are used for C_w by different research groups.

The fact that small changes in the terms of the gas momentum balance used lead to substantially different flow profiles has been exploited by some research groups to obtain agreement between experiments and simulation results. It is therefore of great importance to test the validity of different assumptions in the gas momentum balance.

2.4.2.2 Fluid flow

From the different fluid-dynamic models found in the literature, multi-dimensional two-fluid models with balance equations for both gas and liquid phases presently allow for a detailed description of two phase flow. Only very recently papers appeared where the simulation is based upon a dynamic model (Sokolichin *et al.* 1994; Webb *et al.* 1992, Hjertager and Morud 1993; Becker *et al.* 1994; Lapin and Lubbert 1994; Lubbert and Lapin 1994). In a number of cases these simulations exhibit a substantially different behavior, which seems to be much closer to what is observed experimentally, than the steady state results. The equations of motion are usually derived from the conservation equations for mass and momentum for a volume element. They consist of the Navier-Stokes and continuity equations for the gas phase and the liquid phase, where the following additional assumptions have been made:

- isothermal conditions,
- constant liquid density,
- gas density depending on local pressure as described by the ideal gas law,
- no consideration of turbulence,
- all bubbles of one bubble class are generated with constant mass at the spargers and retain this mass as long as they are in the two-phase domain, that means that bubble coalescence and redispersion is neglected,
- the coupling between the two phases will be described through an interaction force.

2.5 Spatial drop concentration distributions

In two phase-flow, there is little information on the velocity of either phase in single port gas agitated vessels. Measurements concerning solid or droplet suspensions in fluids have been investigated mainly in pipe and jet flows to determine the effects of drop inertia, crossing-trajectories, drop-drop and drop fluid interactions, turbulence and drag, and the results have been reviewed. Laser-Doppler velocimetry has been employed for the measurement of the velocity of each phase. The use of amplitude discrimination for measurements of the dispersed phase is satisfactory but it is unable to distinguish perfectly between Doppler signals of large and small drops (Durst 1981). An alternative method was suggested by Durst and Zare (1975) and involves the phase shift between Doppler signals at different angles of observation. This technique still does not furnish an accurate measure of drop size.

The Phase Doppler anemometer (PDAs) is an extension of the laser Doppler anemometer that usually uses two receiving lenses and photodetectors. PDAs not only measure the particle velocity but, by comparing the phase of the signals seen by the two detectors, the particle size as well. Particle sizing as this is called is necessary in the analysis and monitoring of many industrial processes, products and of pollution. Although this technique seems to be an ideal tool for simple dispersed flows, it is subject to limitations and remains quite hard to master in real two-phase flows.

- Eligible inclusions: The phase-size relationships are well established for homogeneous spherical scatters. Extensions of size measurements have been investigated notably for ellipsoids, and distorted inclusions (Bachalo-1994). Difficulties linked with velocity measurements on large distorted inclusions have been found.

- Limitations due to turbidity: Errors in size measurement (Hardalupas et al. -1994), as well as in velocity measurement occur due to turbidity. Also, in order to collect data

in dense mixtures, endoscopic probes based on spatial filtering are required (Cartellier-1992).

- Flux measurements: Flux, number density, mass fraction and interfacial area concentration are potentially accessible from PDA. However, flux deviations from expected values of 100% or higher are currently reported in the literature. Among the various sources of error (Hardalupas et al. -1994), two are dominant : (i) the necessity to detect all inclusions crossing the probe (this requires a very careful adjustment of the PDA), and (ii) the effective probe volume depends on the size of the inclusions. More efficient correction schemes are now available (Sommerfeld & Qiu -1995). Most of the existing studies are concerned with particles smaller than the beam size. For inclusions larger than the beam diameter, specific difficulties arise in the determination of the effective probe volume, but also the true location of the measurements. Indeed, to recover the variables used in the PDA approach, measurements must be attached to the position of the inclusion centers.

3 EXPERIMENTAL

Attempts to isolate and predict the coalescence behaviour of dilute dispersions of fine drops have not been reported previously for batch gas-agitated liquid-liquid systems. Due to the dynamic conditions of batch experiments, special procedures are needed to determine drop size and local drop concentrations. Usually surfactants are added to extract samples to prevent drop coalescence (Kawecki et al. 1967). Some researchers have encapsulated drops through interfacial polymerisation (Mlynek et al. 1972). Other researchers choose wax as the dispersed phase and by freezing the drops have been able to measure the size distribution of samples. Drop size distributions also are obtained by microscopic examination, photography, or photomicrography (Mok et al. 1971, Shinnar, 1961).

Ross and Curl (1973) forced a stabilised dispersion through a capillary, where a specially designed photometer assembly measured the drop size distribution by determining the intensity of scattered light. Another approach is generating laser Doppler signals in a dual-beam LDA-system which can readily be explained by light scattering from particles penetrating a region in space common to both incident light beams. This region is usually referred to as the measuring volume of the LDA-system although signals may result from outside of this volume, Durst (1973). These additional signals are usually not considered in laser Doppler anemometry and are eliminated in actual measurements by designing the receiving optics to only collect light from the crossing region of the two incident light beams. Phase Doppler Anemometry extends the capabilities of Laser Doppler Anemometry to simultaneous measurements of velocity and size of the scattering particles. This technique makes use of sophisticated and expensive equipment.

In this work, drop sizes and concentrations were measured using a non-intrusive high magnification videography technique. The detailed procedures employed are outlined in this chapter.

3.1 Qualitative measurements

Qualitative observations are needed to support the existence of the proposed mechanisms. The following experiments were performed to confirm their possible occurrence and their relative importance with respect to fine drop recovery.

3.1.1 Experimental apparatus and procedure for observing the coalescence of drops inside eddies

One of the characteristics of wakes behind moving objects is the generation of eddies. Small drops are trapped within these eddies and coalesce. Since observing interactions between micron sized drops in the wake of rising bubbles is a very difficult task, a cell was designed and built to observe drop-drop interactions inside the primary wake behind stationary solid objects exposed to a flowing dispersion. The superficial velocities of the dispersion ranged between 0.1 and 0.3 m/s, and it is expected that the behaviour in such cases is similar to that arising behind moving bubbles (~0.17 m/s). Figure 3.1 shows the shape of this cell schematically. The cell comprises a small half cylindrical object placed between two parallel faces that are 6 mm apart.

A dilute dispersion of oil in water was pumped into the cells. Dispersed oil was generated by injecting a solution of sunflower oil and decane (40% sunflower oil + 60% decane) into flowing water at the inlet. The properties of the liquids used are tabulated in Table 3.1. Video stills were taken directly from the wake behind the half-cylindrical pieces of perspex which were mounted inside the cells. Experiments were repeated with different dispersion flow rates and different oil concentrations. Viscosities were measured using an Ostwald viscometer and interfacial tension was measured using a ring tensiometer. Sources and purities of chemicals are shown in Table 3.2.

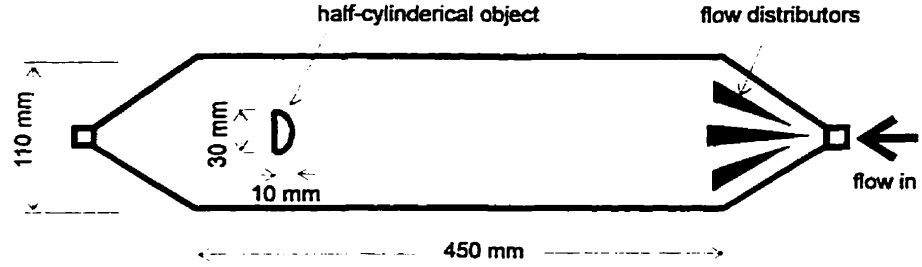

Figure 3.1 -View cell used to observe fine drops inside wakes.

ρ_d	ρ_c	μ_d	μ_c	σ_d	σ_c	σ_i
(kg/m^3)	(kg/m^3)	$(Pa.s)$	$(Pa.s)$	(N/m)	(N/m)	(N/m)
1000	816	0.00097	0.0047	0.0586	0.0245	0.0104

Table 3.1 -Physical properties of the liquid-liquid system.

Chemical	Purity	Source
Nitrogen	99%	CANOX
Sun-flower Oil	78% unsat., 22% sat.	UNICO
Decane	99.8%	Fisher Scientific

Table 3.2 -Sources and purities of chemicals

Video records were obtained using a high speed CCD camera (*Photron 11B*) at 60 times magnification. The camera frame rate was set to 744 frames per second at a shutter speed of 0.0001 *s*. The high shutter speed required background lighting which was provided by a 1 *kW* sodium lamp. The sodium lamp is powered by a 0-20 *kHz* variable high frequency series invertor *AC* power supply. A frosted glass was mounted between the lamp and the cell to give even illumination. The video sequences were stored digitally in a 32 *MB* of video memory. Digital images were then recorded on *S-VHS* video tapes for processing.

3.1.2 Apparatus and procedures for large drop-small drop coalescence experiments

A transparent Perspex cell with a rectangular cross section of 6×84 *mm* was used for these sets of experiments. This cell was designed based on the depth of field of the camera. A schematic view of the cell is shown in Figure 3.2.a. A series of video records were obtained using an Industrial Colour *CCD* Camera (*Panasonic GP-KR402*) with a shutter speed of 0.001 *second.* 80 times magnification was attained using extension tubes mounted between the camera and a 50 *mm* lens. Backlighting of the view cell was arranged by means of a 150 *W* projector lamp and a black cardboard with a 25 mm circular hole in the middle to eliminate spot lighting on the background. This configuration is shown in Figure 3.2.b.

The cell was filled with sunflower oil + decane over water + blue dye. The lower phase height was set at 170 *mm* and the upper phase at 86 *mm*. The physical properties and operating conditions associated with the experiments were the same as those listed in Table 3.1. A schematic view of the overall apparatus is shown in Figure 3.3. The

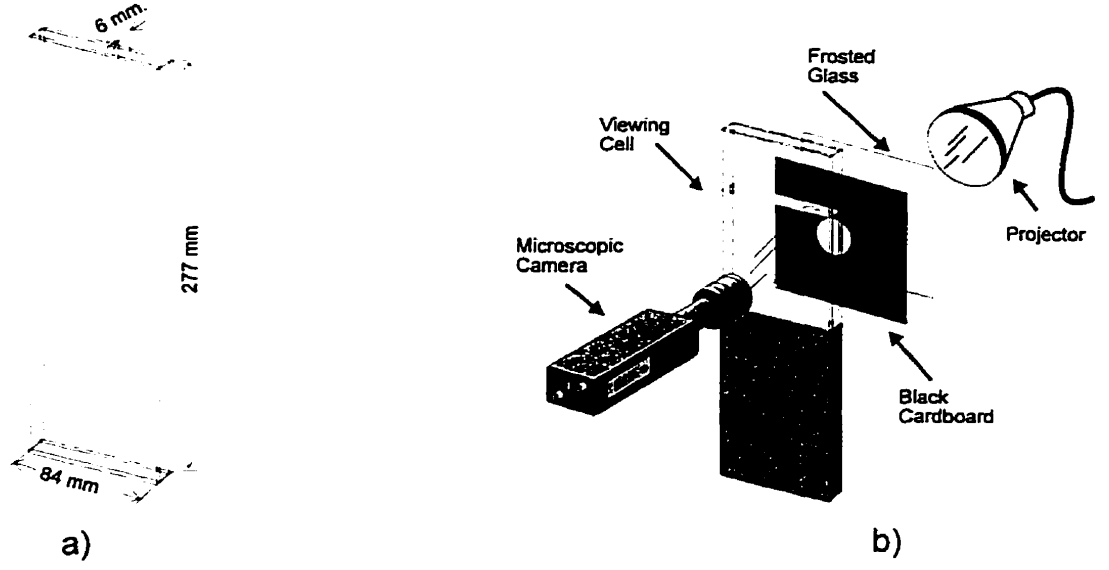

Figure 3.2 -Schematic of view cell and camera set-up.

apparatus was designed to produce bubbles which disperse the lower liquid phase in the upper liquid phase and to allow the dispersion to be video-taped in the upper and lower liquid phase regions. The bubbles were generated in the size range of 5-10 *mm* diameter at the base of the column using a 1 *mm* diameter nozzle. A saturator and a nitrogen gas cylinder were used to produce single bubbles at controlled frequencies. A Matheson 600 series rotameter, equipped with a glass float was used to measure and control the gas flow. The saturator was filled with water to minimise mass transfer between the lower phase and the gas bubbles. It should be mentioned that changes in physical properties of the liquids after long time gas injection was found negligible.

During a typical experiment, Nitrogen gas was injected into the column to produce a dilute dispersion of the lower liquid phase in the upper liquid phase. Then large drops of lower phase liquid were injected into the upper phase using a burette and video stills were taken of their interactions with fine drops.

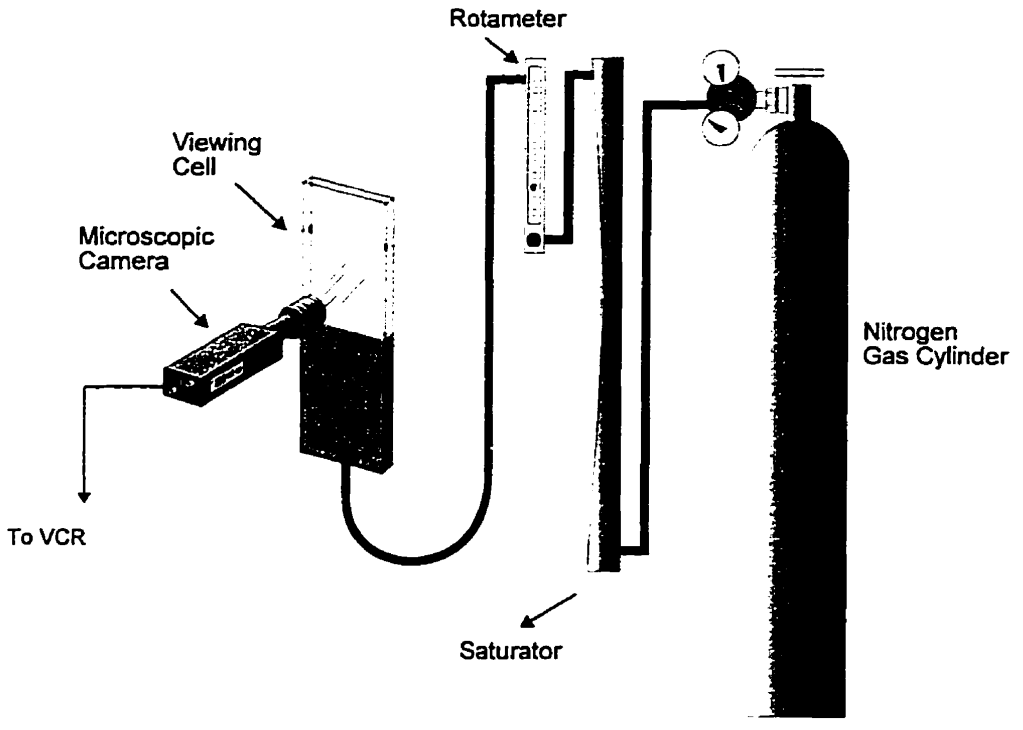

Figure 3.3 -Experimental set-up used for measurements of drop recovery rates.

3.1.3 Apparatus and procedures for drop liquid-liquid interface coalescence experiments

In these experiments, the same set-up described in section 3.1.2 was employed. The physical properties of the fluids were kept the same as in Table 3.1. Nitrogen bubbles were introduced at the base of the cell to produce a dilute concentration of fine drops in the upper phase. The gas injection was then stopped and, by means of a copper pipe (1 *mm ID*) gas bubbles were introduced directly into the upper phase. Video stills were taken of the movement of the fine drops along the liquid-liquid interface at 124 times magnification. These images were recorded and analysed at 60 frames per second on *S-VHS* video tape.

3.2 Semi-quantitative measurements

3.2.1 Experimental apparatus and procedure

The same cell described in Figure 3.2.a was used for semi-quantitative analysis of drop recovery mechanisms. For this part of study, a series of video records were obtained to investigate fine drop recovery under different methods of mild agitation. The cell was operated in a batch mode with respect to both continuous and dispersed phase liquids and in a continuous mode with respect to the gas phase.

During a typical experiment, video images were taken directly of the drops at the middle of the upper phase as shown in Figure 3.4. The number and sizes of drops less than 110 μm in diameter were measured using an image processing package (*MOCHA*) on a 486-66 personal computer equipped with an image digitizer card (Targa). The set-up of equipment for analysing the images is shown in Figure 3.5. Drops in a minimum of three video stills were counted per measurement.

In this way, the total number of drops measured was more than 2000. The drop size measurements were classified at 20 *μm* intervals. A sample frame with the actual dimensions of *3.28 x 2.40 mm* is shown in Figure 3.6.

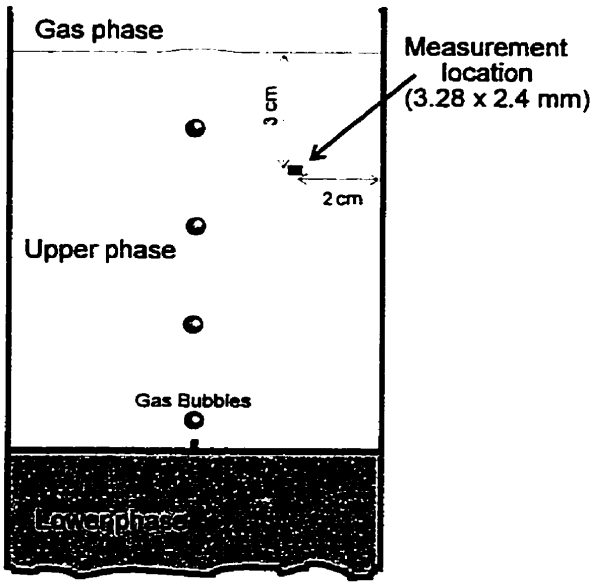

Figure 3.4 -Drop concentration measurement location for semi-quantitative experiments

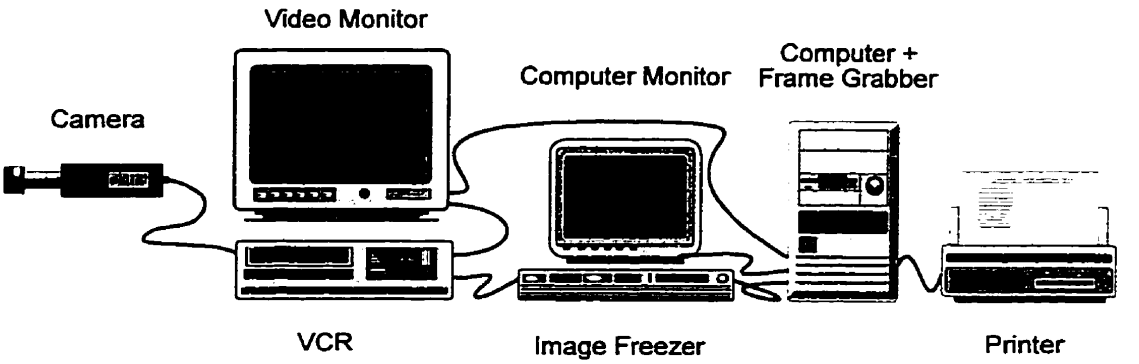

Figure 3.5 -The Configuration of the video analysis system.

Fine drop recovery arising from the introduction of a large number of drops and rising gas bubbles was examined separately. At the beginning of each run, a dispersion was made by introducing nitrogen gas into the lower phase for 15 minutes with a flux of $2\times10^{-3} m/s$. The total number and the size distribution of the drops within the upper phase was measured and checked to maintain similar initial conditions for all

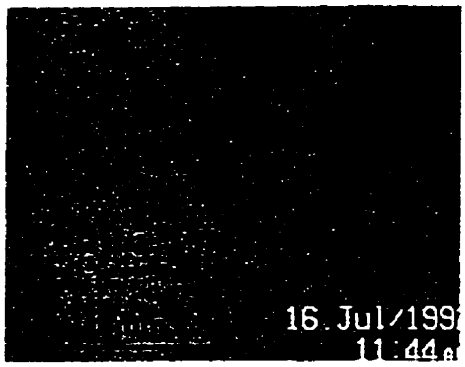

Figure 3.6 -An example video still of fine water drops suspended in a sunflower oil+decane (18 times magnification).

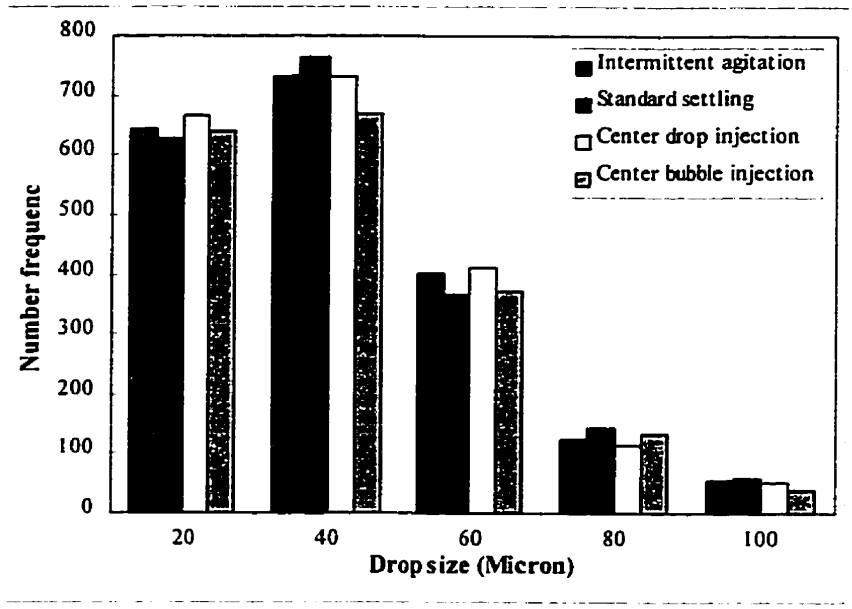

Figure 3.7 -Examples of initial drop size distributions for the semi-quantitative experiments.

experiments as shown in Figure 3.7. Then the gas was stopped and the following tests were performed:

1 Effect of intermittent agitation on fine drop recovery.

This test was performed to examine the effect of intermittent random mixing on fine drop recovery. In these runs, fine drop concentrations and drop size distributions were measured at 10 minute intervals following mixing inside the upper phase. The upper phase was mixed using an aluminium rod.

.2 *Effect of Standard Settling on fine drop recovery.*

This test was performed to examine fine drop recovery in the absence of agitation. Because of the nonhomogeneous concentration of fine drops within the upper phase, the average drop concentration could only be obtained by mixing the dispersion before making measurements. The mixing action disturbed the settling behaviour of the fine drops. Therefore, the experiments were repeated from the beginning using the same initial conditions for each time interval investigated.

.3 *Effect of large drops on fine drop recovery*

Two cases were examined. Large drops (~4 mm diameter) were released from fixed and variable positions along gas-liquid interface. These two types of tests illustrate the impact of coalescence per se and the interaction between flow pattern and coalescence.

.3.a. *Effect of large drops falling from fixed positions inside the upper phase.*

The large-drop small-drop coalescence mechanism was evaluated quantitatively by introducing large drops into the upper phase. A burette was used to produce large water drops at the top-middle of the upper phase (Figure 3.8.b). Drops were generated at the rate of 160 *drops/minute*.

Interactions between large drops and dispersed fine drops were recorded. This experiment was also repeated by introducing drops at the upper corner of the cell (Figure 3.8.a). These changes in the drop introduction positions were made to asses their effect on fine drop recovery rate.

.3.b. *Effect of dropping drops at random positions in the upper phase.*

By moving burette across the top of the upper phase, drops were again introduced at the rate of 160 *drops/minute*, at random positions (Figure 3.8.c).

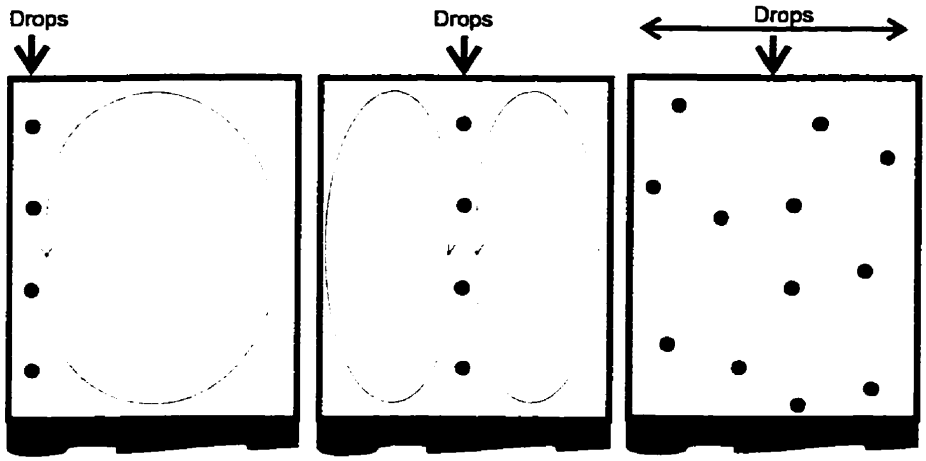

Figure 3.8 - Experimental methods of drop injection inside the upper phase

.4 *Impact of bubble injection on fine drop recovery*

Two cases were addressed. Bubbles were generated at a single fixed position and from multiple fixed positions above the liquid-liquid interface. It was not possible to inject bubbles at random positions without disturbing the liquid-liquid interface.

.4.a. *Effect of gas bubbles rising from fixed positions above the liquid-liquid interface.*

Two tests were again performed to examine the effect of gas bubbling position on recovery rate of fine drops. Bubbles were introduced once again at the middle (Figure 3.9.b), and at one side of the cell (Figure 3.9.a) just above the liquid-liquid interface. The change was made to examine the position dependency between gas injection location(s) and fine drop recovery rate. The total gas flux was set at 2×10^{-4} m/s (approximately 140 bubbles per minute).

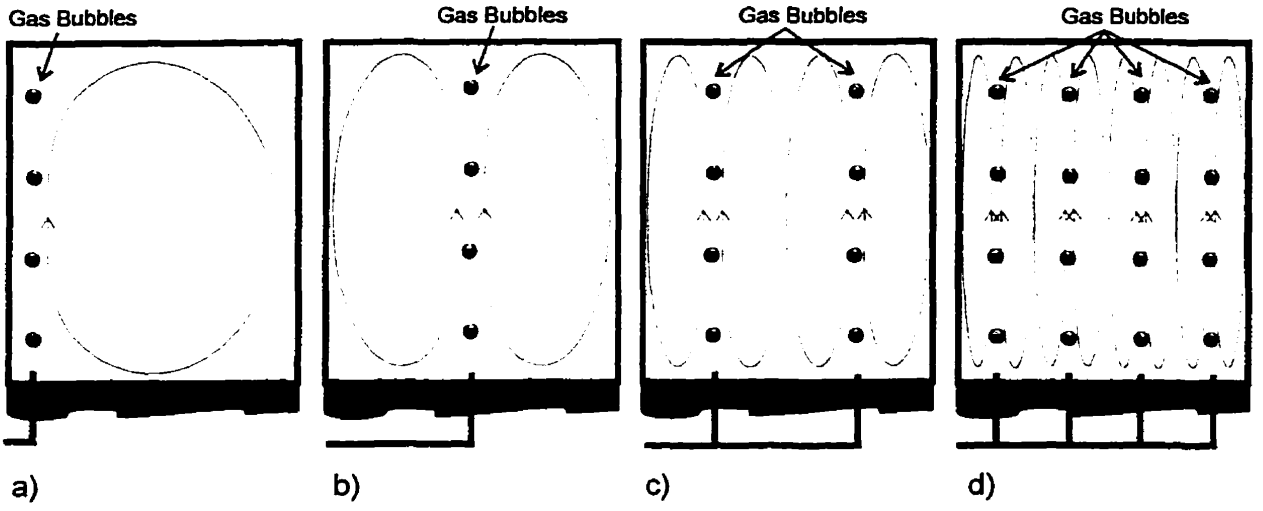

Figure 3.9 - Experimental methods of gas injection into the upper phase

4.b. Effect of multiport gas injection on fine drop recovery.

A cell was designed and built to generate gas bubbles from multiple ports. A schematic view of this cell is shown in Figure 3.10. This cell has the same dimensions as described in Figure 3.2.a. The cell contains four ports made of four copper tubes (1 *mm ID*) that are long enough to pass through the liquid-liquid interface. Two tests were performed. Bubbles were injected into the upper phase using two bubble ports (Figure 3.9.c) and

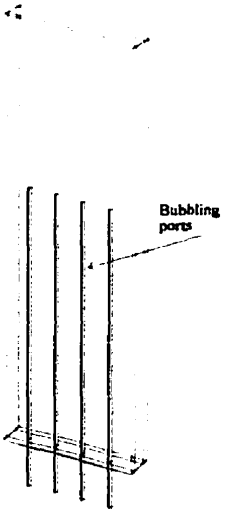

Figure 3.10 -View cell with 4 bubble ports.

another using four bubble ports (Figure 3.9.d). Bubbles were generated at 1.0×10^{-4} *m/s/port* for two bubble ports and at 0.5×10^{-4} *m/s/port* for four bubble ports to facilitate comparisons.

3.3 Measurements of flow field induced by gas bubbles and spacial drop concentration distributions

This section provides details of the experimental apparatus prepared to measure the spacial velocity distribution induced by rising bubbles and also the drop concentration gradients inside the upper phase.

Obtaining velocity distributions requires a particular experimental set-up to allow the microscopic camera to sweep the upper phase at any location. In order to permit transverses of the entire velocity field, the viewing cell was mounted on a two dimensional transversing arrangement which permitted movement of the viewing cell vertically and horizontally relative to the camera. The rig is shown schematically in

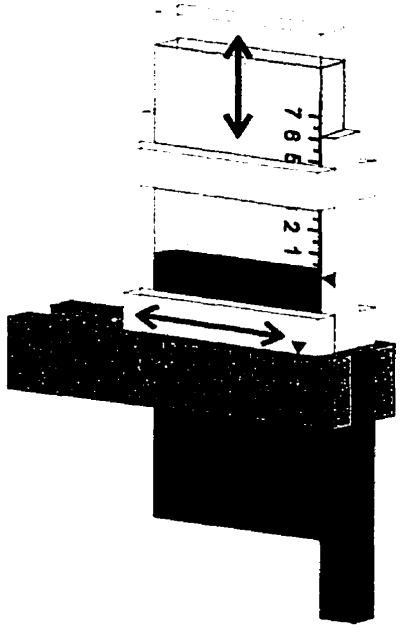

Figure 3.11 -Rig used for spacial drop concentrations and spacial velocity distributions.

Figure 3.11. The isometric view is sufficient to explain the major features of the set-up. The cell was initially filled with two phases of sunflower oil + decane over water + blue dye. The stratified layers of the two phases were agitated using the same procedure as before to produce the initial dispersion of water in oil. Nitrogen gas bubbles were then introduced directly into the upper phase.

The circulation patterns were established in the upper phase with bubbles formed from a

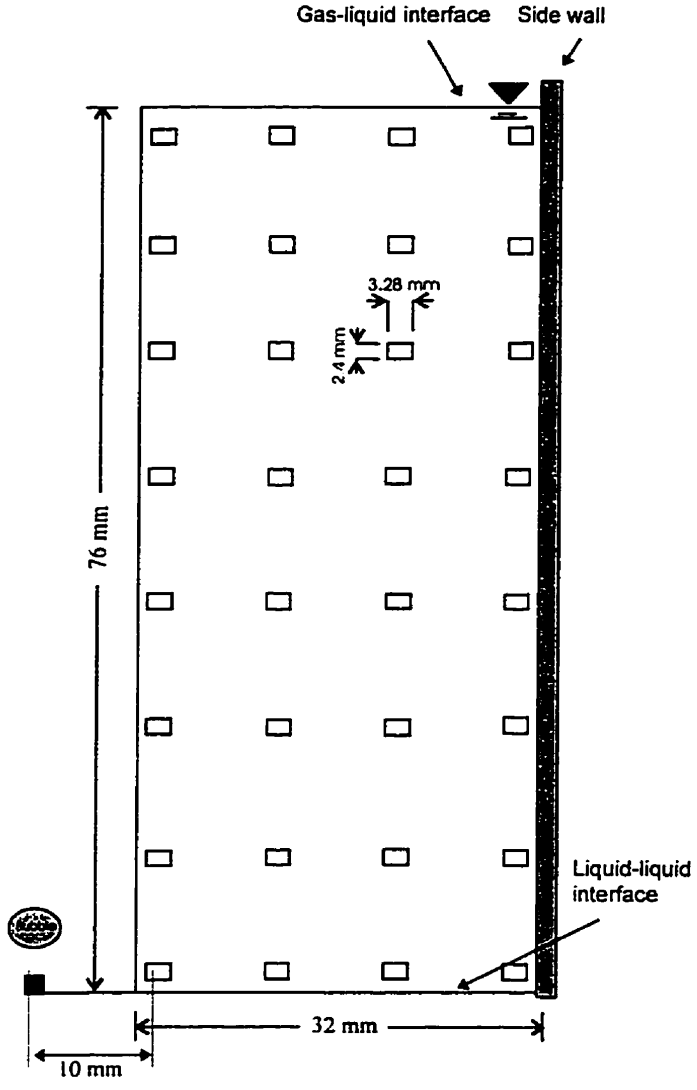

Figure 3.12 -Locations where local velocities drop concentrations were measured.

1 *mm* diameter nozzle located above and in the middle of the liquid-liquid interface. Nitrogen gas was set at a flux of 2×10^{-4} m/s. The cell was moved in the vertical and horizontal directions and video stills were taken at 32 grid points on a 4 × 8 matrix across and along the upper phase. The measurements of the velocities of drops and bubbles were obtained manually with the aid of a Panasonic (AG-1970P) SVHS-VCR at 60 frames per second. The 3.2 x 2.5 *mm* video stills were obtained at the locations shown in Figure 3.12. The spacial velocity distribution inside the upper phase was obtained by measuring the movement of drops less than 20 μm in diameter from still to still at the locations indicated. It took about 2 minutes to complete one sweep of the upper phase.

3.3.1 Velocity fluctuation damping close to the bubble street

The bubble street gives rise to a liquid velocity field where the viscosity of the liquid is responsible for the damping of the velocity fluctuations induced by each bubble. Quantitative assessment of the damping can be made from the analytical solution (Batchelor 1967) of the flow due to a boundary which oscillates in its own plane. The velocity fluctuations propagate away from such a boundary, into the fluid, as damped transverse waves such that the amplitude of the velocity fluctuations falls off with distance (y) from the disturbance as:

$$amplitude \propto \exp(-(\omega / 2\upsilon)^{1/2} y) \qquad 3.1$$

where ω is the angular frequency of the oscillation. The magnitude of this damping term is such that velocity fluctuations penetrate less than one wave-length into the fluid, which (at least for plane flow) is of the order of $(\upsilon / \omega)^{1/2}$ and therefore:

$$y = \frac{\ln(\upsilon / \omega)^{1/2}}{-(\omega / 2\upsilon)^{1/2}} \qquad 3.2$$

In the present case (*gas flux* = $2x10^{-4}$ *m/s*), y is about 13 *mm* from bubble center line. Experiments showed that the velocity fluctuations due to the passage of bubbles are

small at a horizontal displacement of 10 *mm* from the bubble path. This was the closest distance to the bubble street where the measurements of velocity and drop concentration could be carried out reliably and could be the hard boundary for the experimental velocity and concentration measurements.

3.4 Sources of error

3.4.1 Factors affecting image quality

Background intensity

When images are obtained through a camera, intensity values are affected by variations in lighting. Consistent lighting conditions must be maintained if intensity measurements are to produce consistent results. Every frame captured by the camera should be calibrated for background intensity any time there has been a change in lighting conditions. Errors in area or size measurements are caused by changes in background intensity which results from different thresholds.

For consistent measurements, the camera was warmed up for at least fifteen minutes before making measurements. Cold starting caused the recorded image to have different background grey intensity and especially the gray intensity of drops out of camera's depth of field. A significant (up to 10%) warm-up drift of pixel intensities was observed within the first fifteen minutes, but changes could occur for as long as forty-five minutes.

Most video cameras take an image by interlacing two scans, each captured in 1/60 second. One image is composed of all even lines (the two frames are interleaved to form the complete image). Fluorescent lighting turns on and off 60 times per second. Consequently, when using fluorescent lighting to illuminate a subject the lighting can vary greatly between the two frames. This problem becomes apparent in the intensity histogram for an image where striations appear. The effect can also be visible when intensities are measured along a vertical line where the intensities show a saw-tooth

form. The zigzag effect can be substantially diminished by applying a smoothing filter to the image.

Threshold

The intensity resolution in MOCA is 1/256 of the total intensity range. The translation of gray levels into actual light and dark intensities is determined by the equipment and by hardware adjustments. To count and measure the area of drops, they should be isolated from the background. This task is done by defining gray intensity of the interest. Measurements of the size and number of drops are very sensitive to changes in background intensity, depth of field and initial set-up of the hardware. Each one of these parameters has a considerable effect on the measurements obtained. Since the cores of drops appear darker than their edges, a minor change in threshold value also causes some of the drops present in a size range to shift to another size range. Drops that are a few pixels in size can disappear at lower thresholds and can appear to be larger at higher thresholds.

Based on measurements performed on a single frame, in Figure 3.6, an average standard deviation of 2 μm for 40 μm diameter drops was obtained for every unit change in threshold. The deviation was much higher when background intensity between frames was different. This error was less important when drops were binned coarsely and when a large number of drops were classified. The threshold was adjusted to 210 for all the measurements.

Resolution

Image resolution is determined by the quality and setup of the system used. To a certain extent, resolution can be improved by using more expensive frame grabbers, cameras and lenses; however, this is no guarantee of improved performance. Each piece of hardware imposes its own resolution limits on the system. The image source, e.g. camera or VCR,

determines the maximum resolution. Images are digitized both spatially and by intensity, and their spacial and intensity resolutions are determined at this stage.

- *Spacial resolution*

  The optics in the camera can resolve details down to a specific size, anything smaller cannot be distinguished. Objects close to the limit of resolution of the instrument may appear blurry and be difficult to distinguish. If the image is out of focus, the resolution of finer drops suffers.

- *Intensity resolution*

  Intensity resolution (how difference in light intensity can be detected) is determined by the image source, the frame grabber, and the configuration and adjustment of the hardware. Depending on the quality of the camera and lighting, variations in brightness on the subject will be translated into significant differences in the digitized image.

Other factors, such as poor electrical connections or outside interference with the electrical signals at the time an image is captured can also affect resolution. The combined effect of these errors is such that area measurements on drop size measurements obtained for drops in the 10-30 μm diameter size range is least accurate. Drops less than 10 μm are not resolved reliably by the apparatus and they were not counted in data processing.

3.4.2 Drop size calibration

Before any geometric measurement, the Frame grabber Aspect Ratio, FGAR, must be set in order to obtain accurate measurements. The FGAR is used to specify the ratio of a pixel's vertical and horizontal dimensions. The accuracy of a measurement, i.e., how closely it reflects the true value, is a function of the precision with which the measurement is made, the precision of the system, and the accuracy of calibration. When

calibrating the image processing package, a relationship between the number of pixels representing an object in a frame and the real size of that object is specified. This can be done by calibrating the number of pixels in a row which corresponds to $100\,\mu m$, or the number of pixels corresponding to the area of a 100 μm diameter drop. If the calibration is inexact, then each measurement based on the calibration reflects the error systematically. In these experiements, the calibration was done by measuring the cross section of a 1.783 *mm* diameter wire. The following correlation was obtained:

$$d = 6.3076 \times 10^{-6} \, (Number\ of\ pixels)^{1/2} \qquad 3.3$$

4 RESULTS AND DISCUSSION

4.1 Qualitative assessment of the coalescence mechanisms

4.1.1 Large drop-small drop coalescence

In static settlers, the possibility of contact between large and small drops increases when the smaller drops move in the same vertical direction as the larger ones. Video stills obtained clearly show this type of interaction. Small drop-large drop coalescence was readily observed as shown in Figure 4.1. However, the number of contacts that led to coalescence was few. Thus the industrial practice of injecting gas bubbles below the liquid-liquid interface which introduces large lower-liquid drops into the upper liquid phase in addition to smaller ones (Shahrokhi and Shaw, 1994), is a possible but inefficient mechanism for enhancing fine drop recovery.

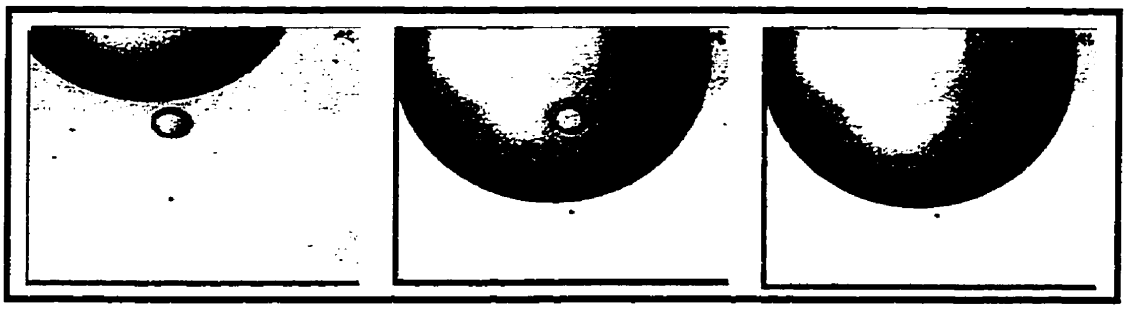

a) 0 s. b) 0.233 s. c) 0.267 s.

Figure 4.1 - Coalescence between a 5.6 mm diameter water drop and a 500 μm diameter water drop in a continuous decane + sunflower oil phase.

4.1.2 Drop liquid-liquid interface coalescence

Gas bubble injection generates circulation loops in the upper liquid phase that are in a plane perpendicular to the liquid-liquid interface as shown in Figure 4.2. This flow is characterized by bubbles rising along the centerline and the resultant flow is axi-symmetric. Under high magnification a shear flow was detected along the liquid-liquid interface. The video records show that drops are propelled toward the liquid-liquid interface by these circulation loops and start to roll and coalesce once contact is made. Re-entrainment of drops in contact with the liquid-liquid interface was not observed. Injection of large lower phase liquid drops from a fixed location along the top of the upper liquid phase induces a similar though less intense flow pattern of opposite sign.

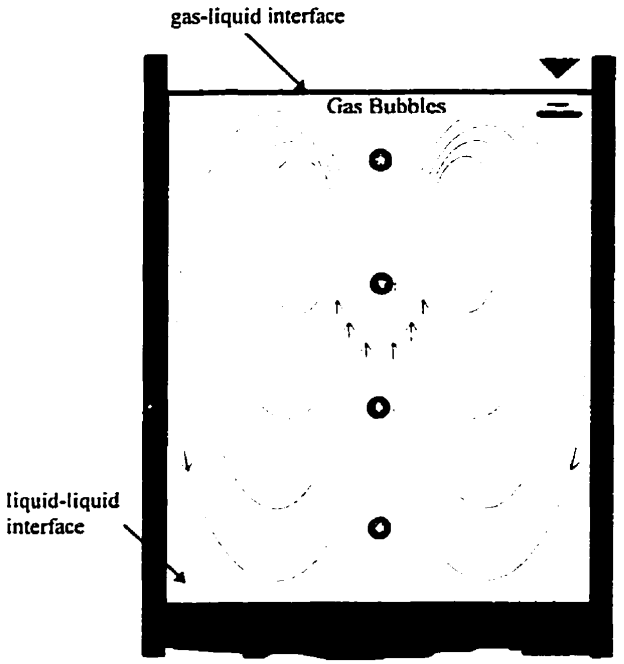

Figure 4.2 -Liquid circulation in the upper phase resulting from gas injection through a single injection port at the lower centre of the upper liquid phase.

4.1.3 Drop-drop coalescence in eddies

In general, drops tend to become trapped within the enclosed wake behind bubbles and can coalesce over time as the motion of eddies does not separate them. Video records

were taken which show the circulation of liquid and the movement of fine drops in the primary wake of half-cylinder objects. Experiments were repeated for different dispersion flow rates and concentrations. Increasing the flow rate of continuous phase generated larger primary wakes and more drops were trapped in this region. At lower flow rates the size of the primary wake decreased but the number of collisions also decreased. While collisions between small drops were noted no indication of coalescence was observed. These observations plus the sparse small-drop large-drop coalescence data discussed above show that drop-drop coalescence is a drop recovery mechanism of secondary importance and coalescence between small-drops in particular can be neglected.

4.2 Semi-quantitative drop recovery measurements

4.2.1 The impact of different agitation methods

The results from the fine drop (< 110 μm diameter) recovery experiments are summarized in Figures 4.3.a and 4.3.b. The measurements were done from a single point as shown in figure 3.4. As expected, at long settling times most of the fine drops are recovered regardless of the action taken. The greatest differences in the drop recovery results, for different agitation methods, arise at short times.

.1 Intermittent agitation

Random intermittent agitation of the upper phase yields the lowest rate of fine drop recovery. This arises because as drops settle the concentration of drops varies with elevation in the upper liquid phase. The dispersion thins out from the top and thickens close to liquid-liquid interface. Random disturbances (intermittent agitation) in the upper liquid phase reduce the net drop settling rate below the undisturbed standard settling case and Figures 4.3.a and 4.3.b clearly show that agitation per se inhibits fine drop recovery.

.2 Standard settling

Settling rate for single drops or particles can easily be calculated using the Hadamard-

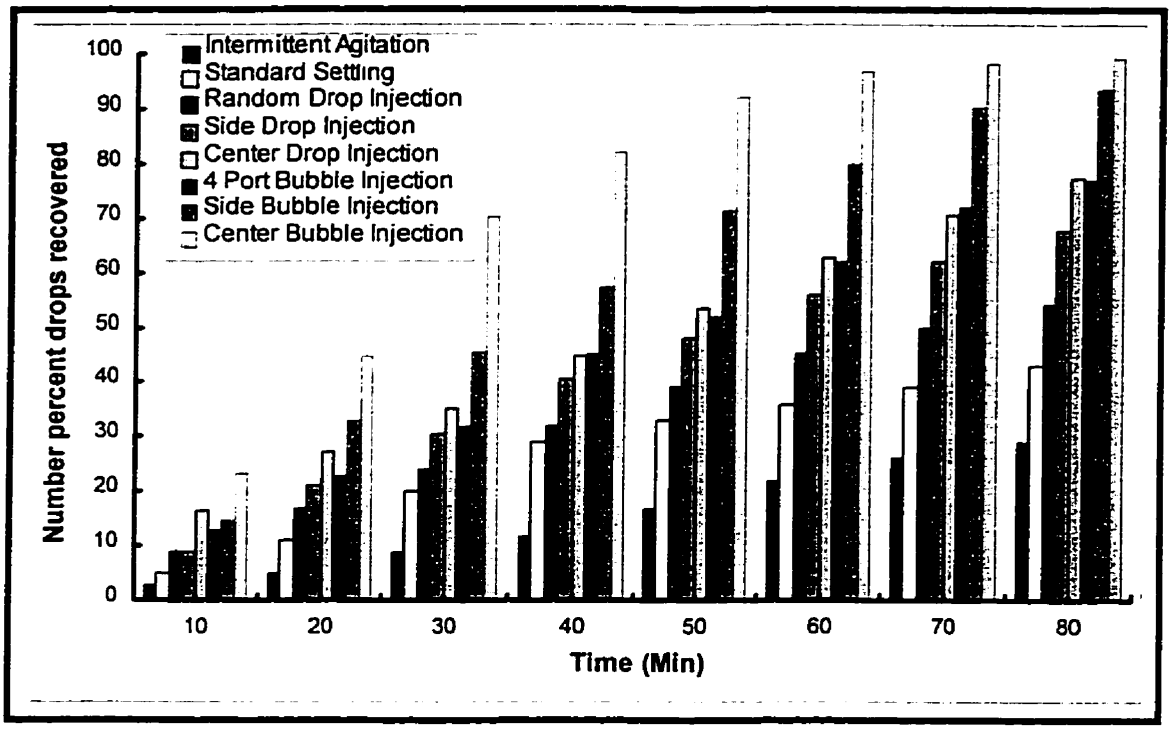

Figure 4.3.a -Overall Fine drop removal by number percent.

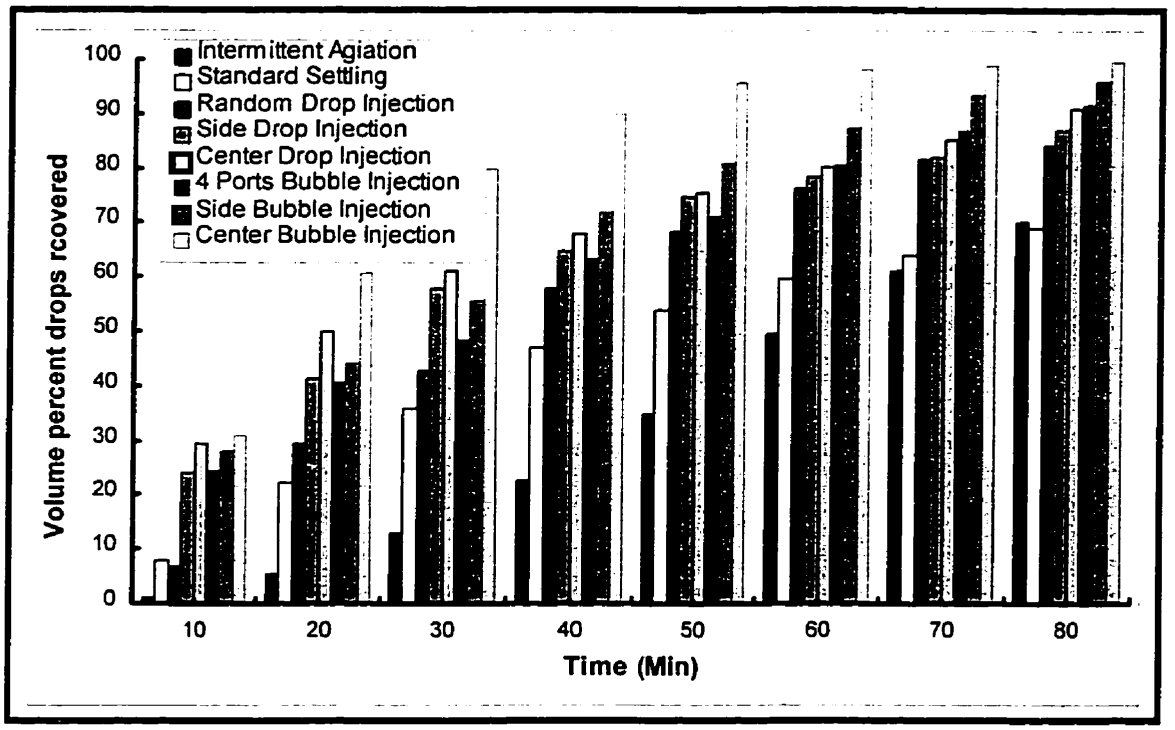

Figure 4.3.b -Overall Fine drop removal by volume percent.

Rybczynski equation (4.1). This equation gives the terminal velocity of a fluid drop in creeping flow by equating the total drag to the net gravity force,

$$U_t = \frac{2gd^2\Delta\rho}{3\mu_c}\left(\frac{1+p}{2+3p}\right) \qquad p = \frac{\mu_d}{\mu_c} \qquad 4.1$$

In equation 4.1 the fluid particle is assumed to move relative to a fluid of infinite extent with its interface completely free from surface-active contaminants. The presence of surface active agents eliminates internal circulation and equation 4.1 reduces to:

$$U_t = \frac{2gd^2\Delta\rho}{9\mu_c} \qquad 4.2$$

Using this latter equation (Stokes law), the fraction of drops remaining dispersed at any given time can be obtained using:

$$\%\,Remaining = \left(1 - \frac{t}{H/U_t}\right) \times 100 \qquad 0 \le t \le H/U_t \qquad 4.3$$

where H = the height of the upper phase

Results of sample calculations are shown in Figure 4.4. Experimental results for standard settling are shown in Figure 4.5, where the data were obtained by measuring drop concentrations at 28 grid points at 15 minutes intervals. Clearly, hindered settling and electrostatic forces reduce the settling speed below that of individual drops and the results are quantitatively different from the behaviour of a single drop in an infinite pure fluid. The difference is less pronounced for smaller size drops.

.3 Mild agitation with large drops

With reference to Figures 4.3.a and 4.3.b, results from the large drop injection experiments show that large-drop small- drop coalescence is a coalescence mechanism of secondary importance. This can be concluded by comparing random drop injection to the

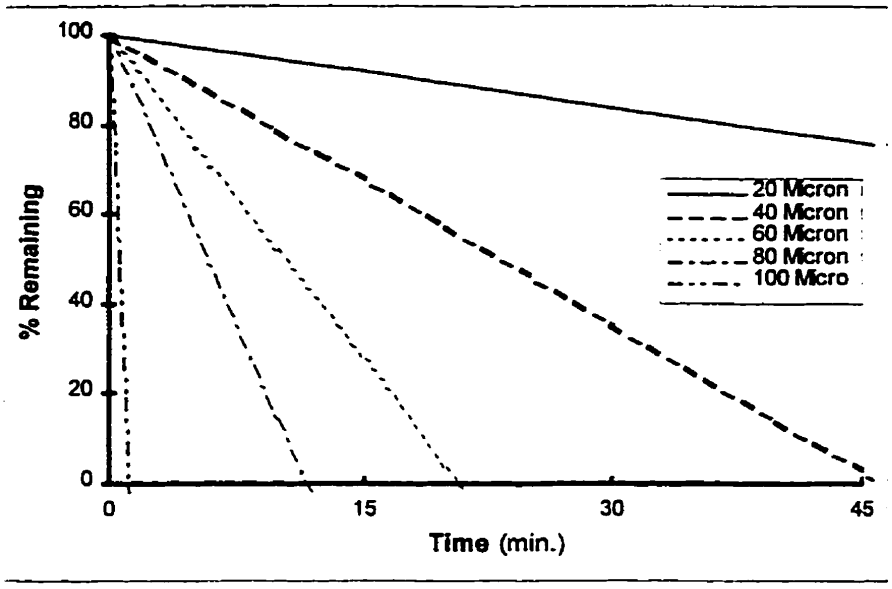

Figure 4.4 -Drop retention in the upper phase (using equations 4.2 and 4.3)

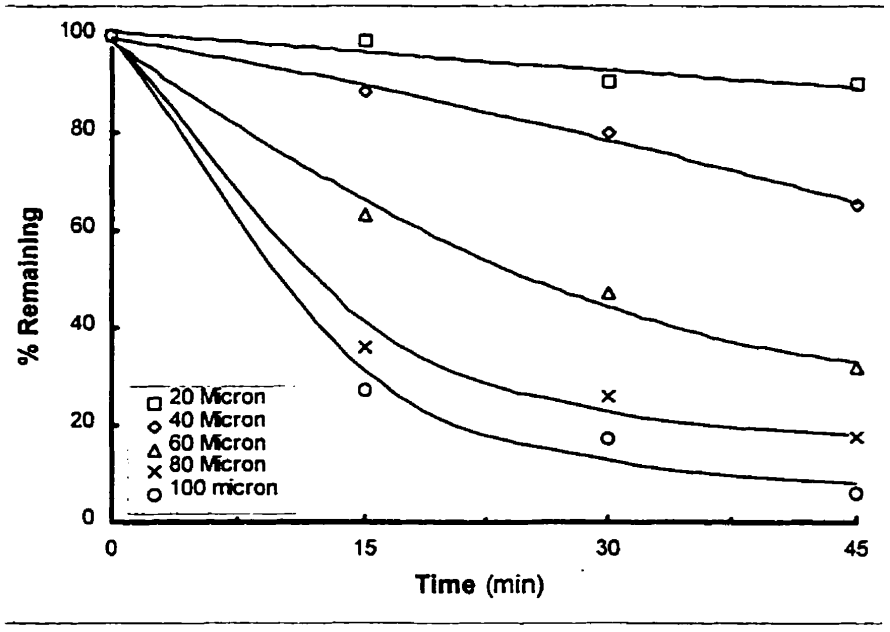

Figure 4.5 -Drop retention in the upper phase (standard settling method, experimental results).

impact of the circulation loop(s) generated by injecting large drops from fixed positions (center and side), at the same drop flux. When drops are injected at the top corner of the

upper liquid phase (side drop injection) one loop is formed. Injection at the middle of the upper edge generates two loops. Random drop generation simply disturbs the upper liquid phase. At 20 minutes, for example, the volume percent recovery for side and center drop injection are approximately 40 and 50 percent respectively. Random drop injection is about 30 percent and standard settling is 25%. Clearly, large drop-small drop coalescence is a much less effective mechanism in drop recovery than circulation loops in the upper liquid phase.

4 Mild agitation with large bubbles

As noted, drops may undergo collision and coalescence in the wake of bubbles, but this was not observed. Three sets of experiments were performed to assess the impact of bubble injection on the rate of fine drop recovery at fixed values of gas flux. The results are shown in Figures 4.3.a and 4.3.b. The number of circulation loops depends on the number and position of gas injection ports. Four ports generate 8 loops, center bubble injection 2 loops and side bubble injection 1 loop. Bottom-center bubble injection has the greatest impact on fine drop recovery at the experimental gas flux (2×10^{-4} ms^{-1}). Comparing these results with the standard settling case shows a *three* to *five* fold improvement in fine drop recovery after 20 *minutes*, based on volume and number percent respectively. The bottom-center gas injection experiment was repeated to check

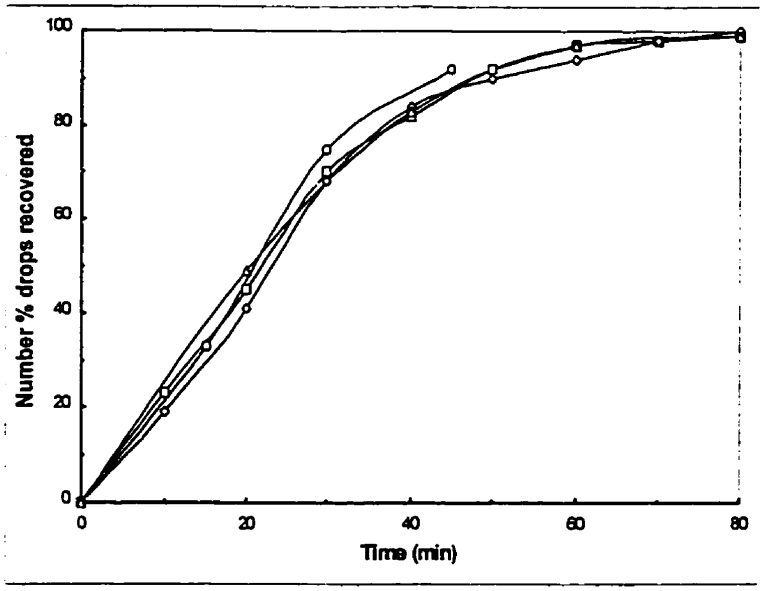

Figure 4.6 -The reproducibility of the bottom-center single bubble injection port experiments, superficial gas flux = 2×10^{-4} m/s).

the reproducibility of these experiments. As shown in figure 4.6 a maximum difference of 4 number percent for the mean was obtained (at 20 minute). Other experiments were not repeated.

The results of different drop and bubble injection options show that fine drop recovery can be improved several fold depending on the number and position of drop or gas injection ports. This factor can only be related to the flow pattern that each technique imparts in the upper liquid phase. Each flow pattern has a direct impact on the flow close to the liquid-liquid interface which is a function of number of circulation loops. The experiments with bubble injection confirm the importance of circulation loops, particularly with respect to the recovery of smaller drops, and therefore the dominance of the drop liquid-liquid-interface coalescence mechanism in fine drop recovery process.

4.2.2 The impact of circulation patterns on fine drop recovery

Rising bubbles or falling drops generate convection flows in the shape of circulation loops inside the upper phase. The results summarized in Figures 4.3.a and 4.3.b point to an optimum number of loops per unit length of interface. For the apparatus in this study, the value of the optimum is two to four loops for gas injection and at least two loops for drop injection over a 0.086 *m* distance.

The impact of the number of recirculation loops on the recovery rates of various drop sizes for the gas bubble injection experiments is shown in Figure 4.7 and for the large-drop injection experiments in Figure 4.8. In both experiments the rate of drops and gas bubbles injection was the same in term of numbers. A similar pattern emerges in both cases. The latter figure shows that the lower speed large-drop induced recirculation loops are less effective with respect to fine drop recovery than the higher speed bubble induced recirculation loops. These results address the importance of circulation speed and the number of circulation loops on fine drop recovery. It should be noted that these results are semi-qualitative as drop concentration was only measured at one location for these experiments.

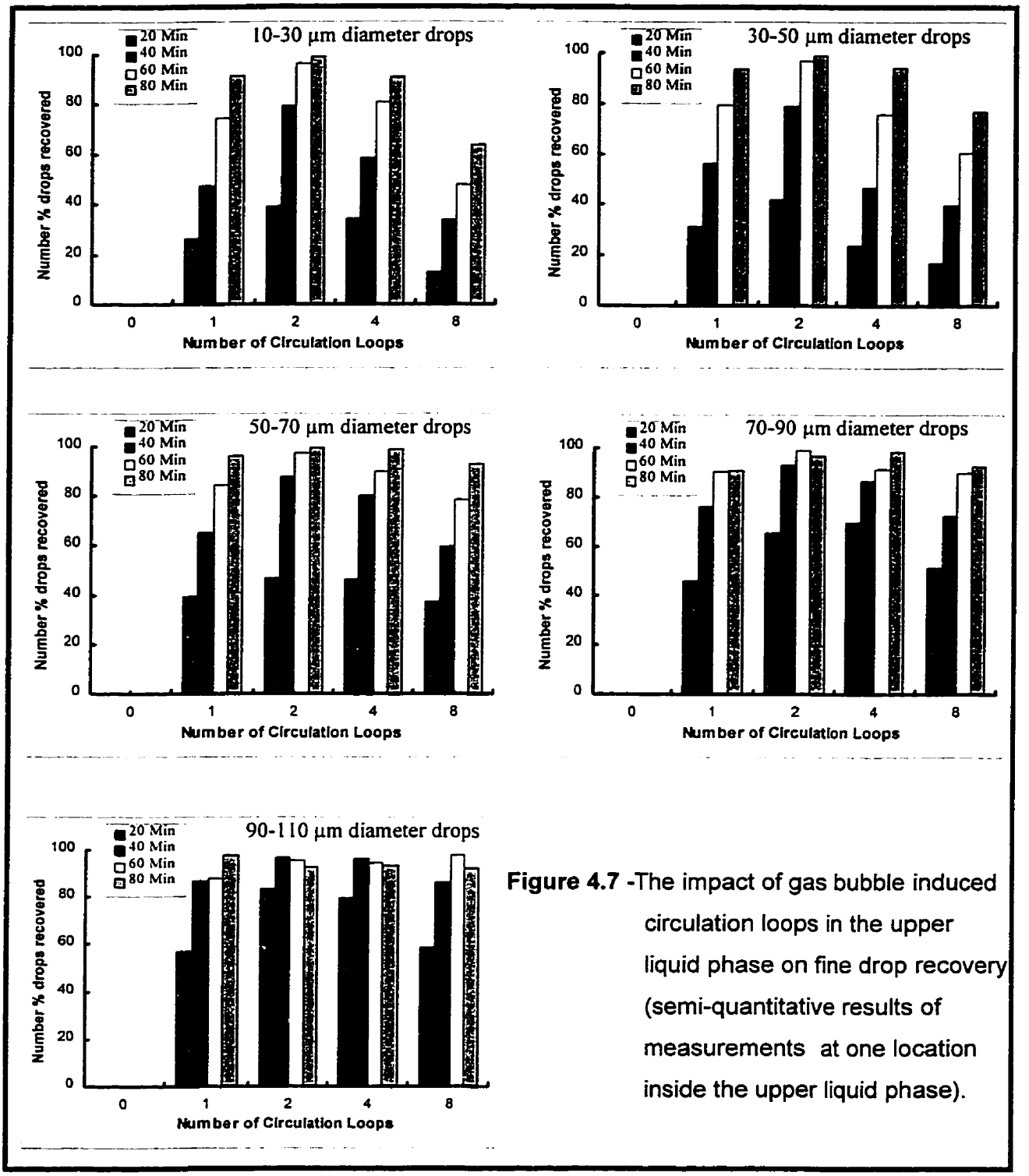

Figure 4.7 -The impact of gas bubble induced circulation loops in the upper liquid phase on fine drop recovery (semi-quantitative results of measurements at one location inside the upper liquid phase).

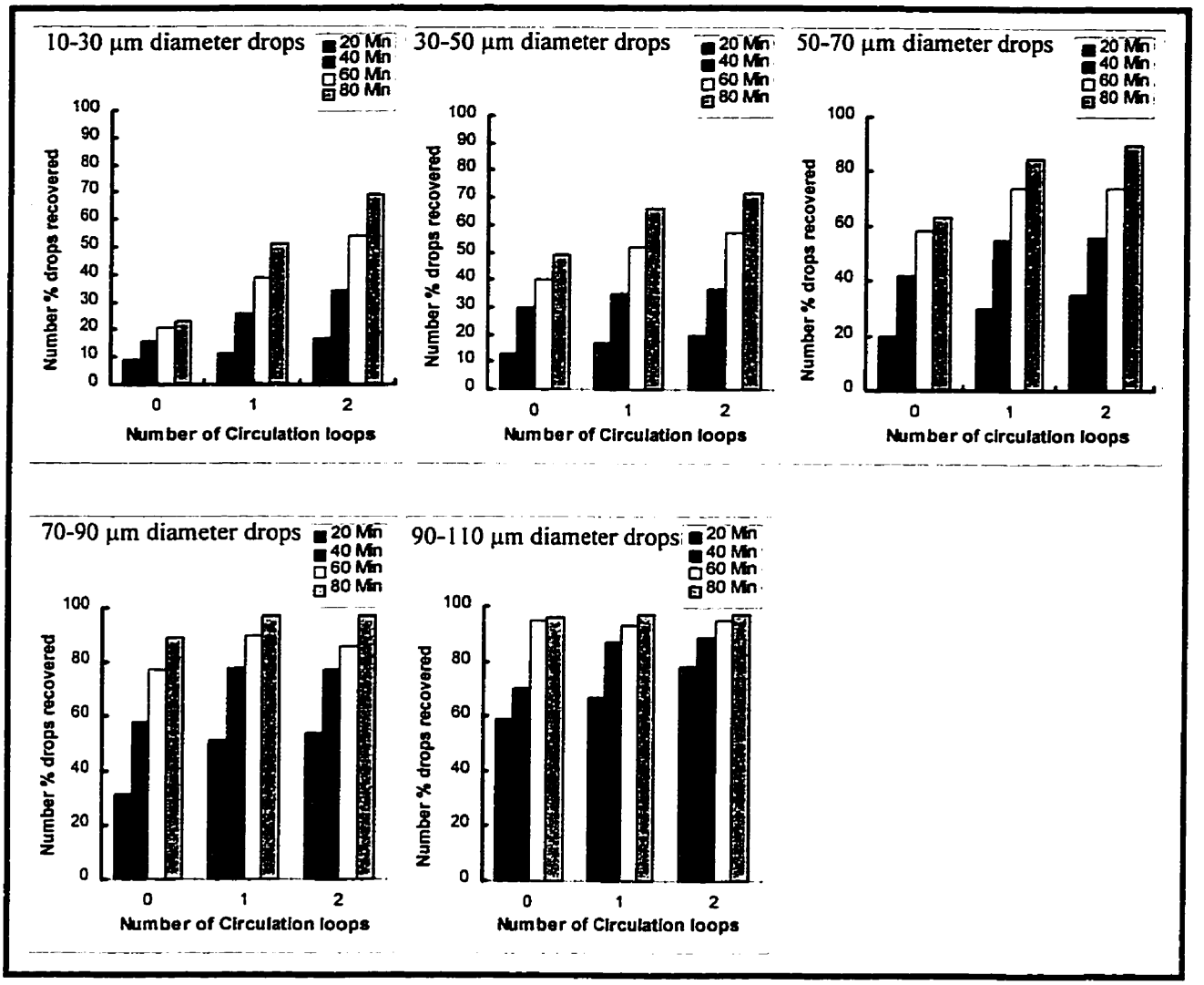

Figure 4.8 -The impact of large drop induced circulation loops in the upper liquid-phase on fine drop recovery (semi-quantitative results of measurements at one location inside the upper liquid phase).

4.3 Flow field in the upper liquid phase

Given the importance of circulation loops in fine drop recovery, the flow pattern in the right half of the cell for a single centrally located bubble port was investigated. The cell was mounted on two sliding rails, and was moved in the vertical and horizontal directions so that video records could be obtained at 28 grid points over a two minute period. The velocities of drops and bubbles were measured manually from successive video stills recorded at 30 frames per second. Bubble speeds were measured directly. The

flow field was dominated by a single recirculation loop where the maximum recorded liquid speed was ~ $5.51 \times 10^{-2}\ ms^{-1}$. Reliable liquid velocity measurements could not be obtained near the bubble street and the upper-liquid air interface due to fluctuations and the speed of the flow, respectively.

4.3.1 Flow pattern within circulation loops

The bubble driven liquid flow studied in this work is characterized by bubbles rising along the centerline of the view cell with the resultant flow being axi-symmetric. The general flow pattern, in the right half of the cell, which is induced by the bubble street is shown in Figure 4.9. The flow is dominated by a single circulation loop. Rising bubbles in the cell carry liquid upward. This effect was first reported in bubble columns by De Nevers (1968), who stated that the liquid circulation pattern is induced by density differences caused by maldistribution of the bubbly phase across the cross sectional area of the column.

The vertical variation of the bubble velocity is shown in Figure 4.10. The bubbles move at a Reynolds number ($d_b v_b / \upsilon$) of approximately 126. The figure shows that the bubble velocity increases until it reaches its terminal velocity. The measured terminal velocity for a single 4 *mm* diameter bubble rising in a stagnant upper liquid phase is about 135 $mm.s^{-1}$. The experiments show the bubble street rises at velocities of about 175 $mm.s^{-1}$ relative to a fixed reference frame. This difference is due to the liquid motion in the cell. However, the appropriate value of the terminal velocity is uncertain due to the tolerance on the diameter of the bubbles and other factors. For example, it is well known that the hydrodynamics of rising bubbles is strongly influenced by the impurity content of the interface layer between the gas inside the bubbles and the surrounding liquid. This dependence was reported by Brankovic et al. (1984). Durst et. al. (1986) showed that the bubble velocity decreases with increasing distance from the bubble generating nozzle as surfactants accumulate at the interface. Figure 4.10 shows that bubbles accelerate near the nozzle and decelerate near the gas-liquid interface. The maximum bubble velocity is

achieved about six bubble diameters away from the nozzle and deceleration starts about three bubble diameters from the free liquid surface.

Drops with $d \leq 20\ \mu m$ are sufficiently small to follow the main flow and, hence, fluid velocity measurements can be carried out by measuring the velocity of drops in this size range. Detailed liquid-velocity profiles were measured and the profiles in the vertical and

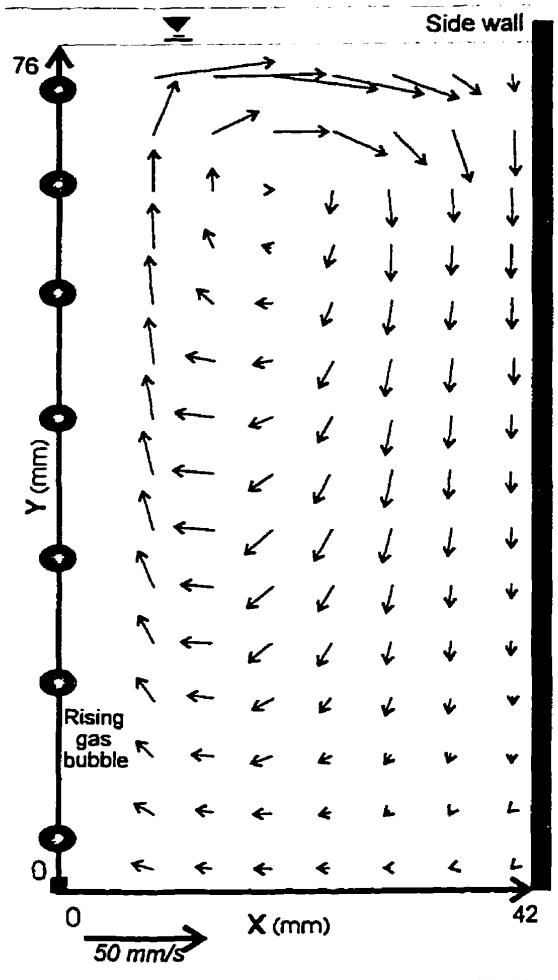

Figure 4.9 -Experimental results of spacial velocity distribution in the right half the upper liquid phase.

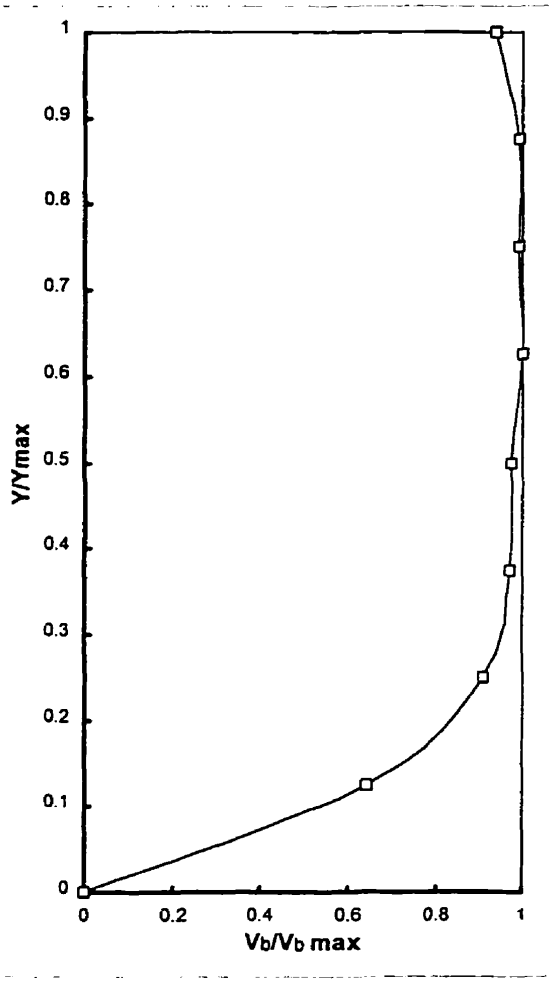

Figure 4.10 -Vertical (center line) development of bubble velocity of ($v_{b\ max}$= 175 mm.s^{-1}).

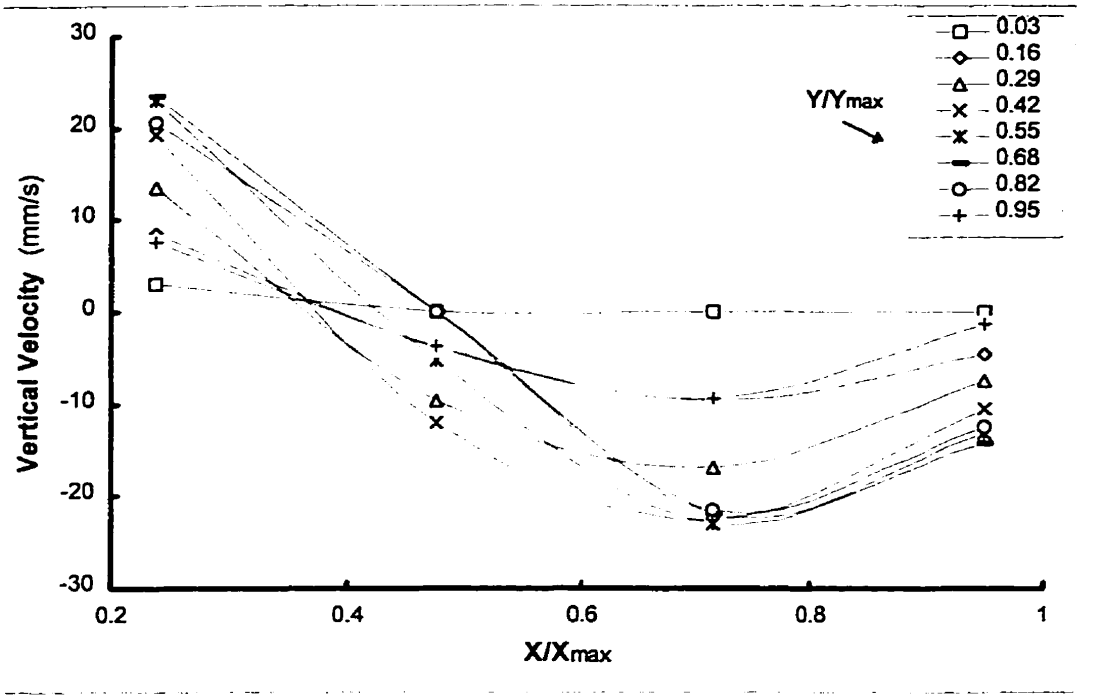

Figure 4.11 -Local upper liquid vertical velocities.

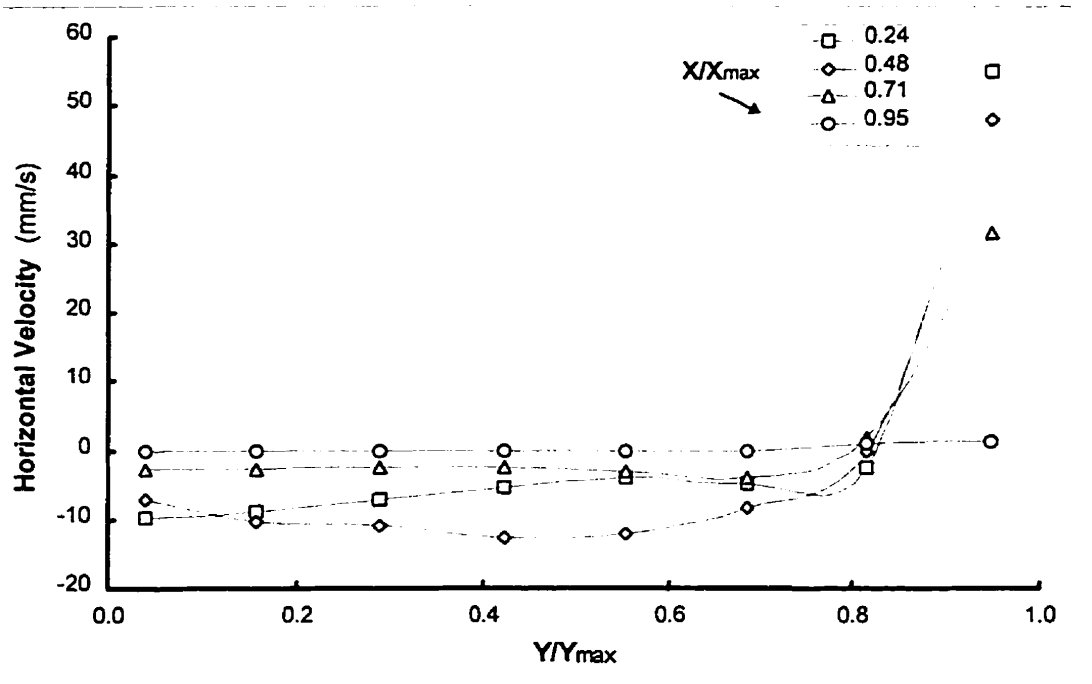

Figure 4.12 -Local upper liquid horizontal velocities.

horizontal directions are presented in Figures 4.11 and 4.12 respectively. The horizontal velocity profiles in Figure 4.12 exhibit a maximum near the free surface where the vertical flow, entrained by the bubble column, approaches the free surface and is deflected horizontally. It was not possible to obtain measurements of the liquid velocity in the vicinity of the bubble street and the free surface. This was because of the velocity fluctuations (bubble street) and the high speed of drops (gas-liquid interface).

Experimental velocity values were obtained from the average of 7 highest values among 15 measurements at each measuring point. The highest deviations are in measurement of velocities close to the rising bubbles (1 cm distance) of up to 9.4% (midway between liquid-liquid interface and gas-liquid interface) and the lowest deviations are in low speed regions, down to 0.31% at left-bottom corner of the cell.

4.4 Spatial drop concentration distributions

4.4.1 Drop concentration distributions time dependence

The relative local concentration of drops as a function of time is presented in Figures 4.13.a-d for four measurement times (4, 15, 30 and 45 minutes). Figure 4.13.a shows a relatively homogenous drop concentration distribution over the upper liquid phase after 4 minutes. Figure 4.13.b shows that relative drop concentrations after 15 minutes are lower near the side wall and close to the bubble street. The relative concentrations reach a maximum value around the position of $x/x_{max} = 0.5$ at any elevation. This issue is addressed in Chapter 5. Figure 4.13.c shows a slight shift in the location of the maximum relative concentrations at higher elevations toward the side wall at 30 minutes. Figure 4.13.d shows the relative drop concentration profile after 45 minutes of mild agitation. Drop concentration is nearly uniform.

The detailed relative drop concentration profiles by size range are presented in Figures 4.14 to 4.18. These figures show the evolution of concentration profiles for each drop size range. Figures 4.14 to 4.16 have similar patterns as in Figure 4.13. Figures 4.17 and 4.18 again show a shift in maximum concentrations from left to the side wall. The only

difference between these latter two figures which represent the concentration of larger size drops, and other figures, is the tendency for such drops to concentrate close to the side wall and at the liquid-liquid interface.

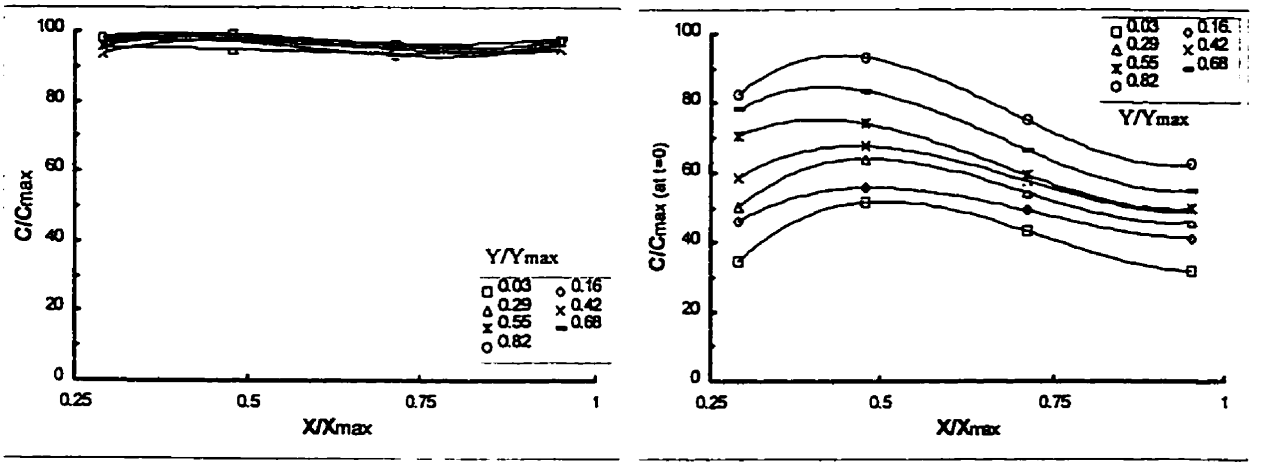

a) t = 4 min.

b) t = 15 min.

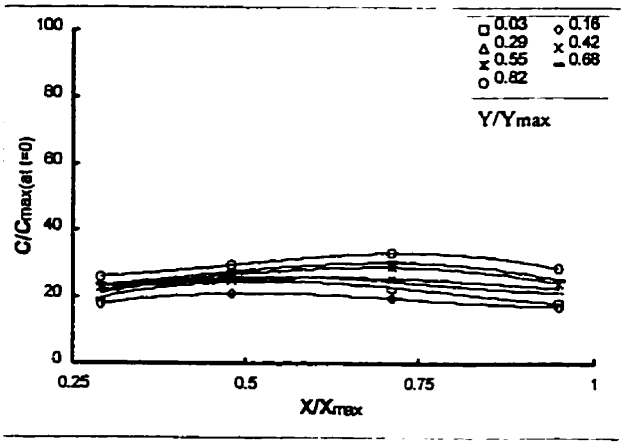

c) t = 30 min.

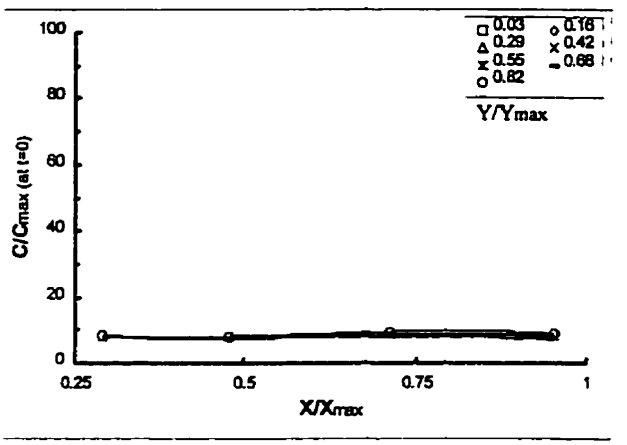

d) 45 min.

Figure 4.13 -The evolution of the percent relative number concentration distribution for the 10-110 μm diameter drops across width of the cell (Single bubbling port at the bottom-center of the upper phase, superficial gas flux = 2×10^{-4} m/s).

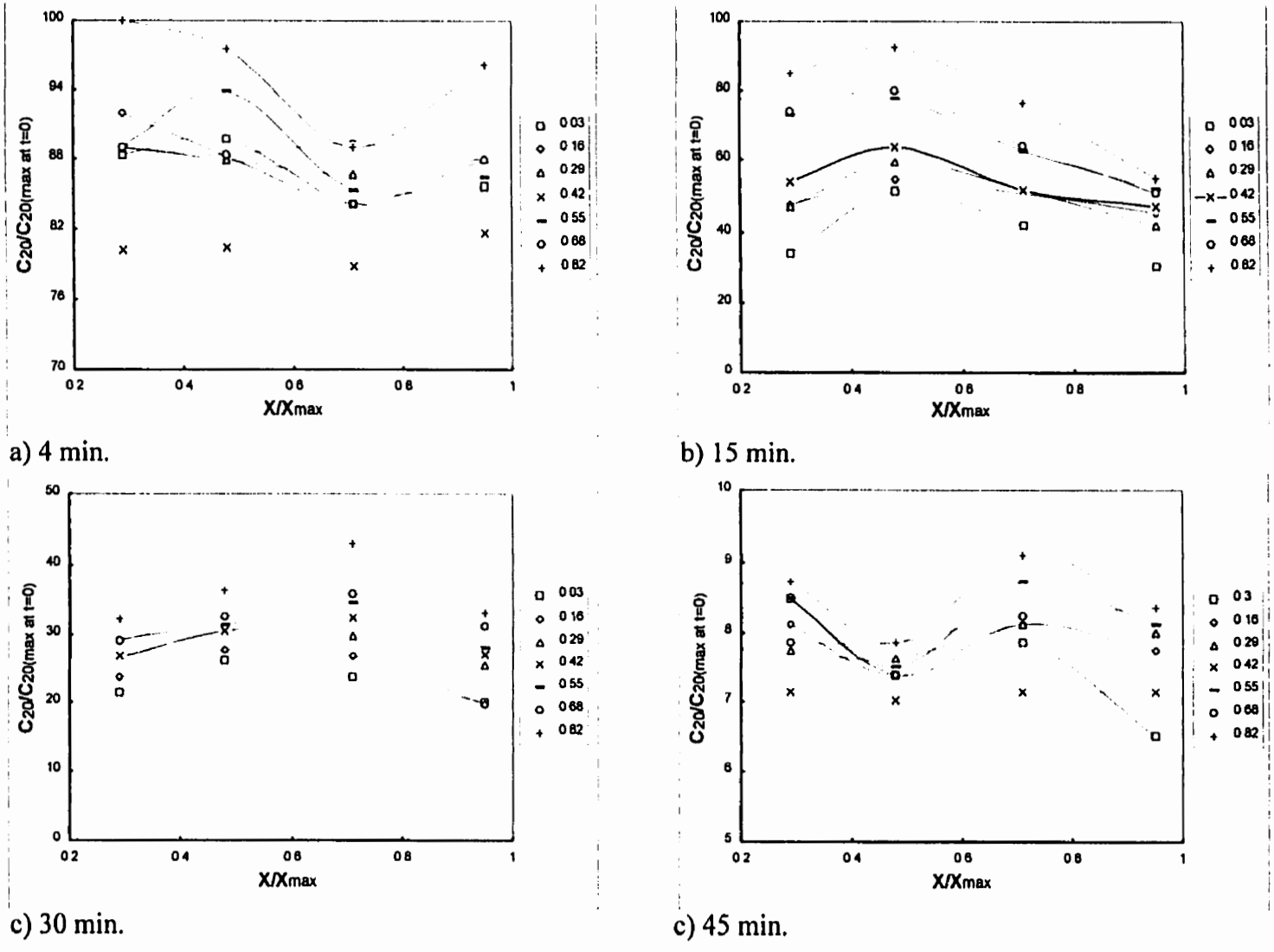

Figure 4.14 - The evolution of the percent relative number concentration distribution for 20 μm diameter drops across the width of the cell (Single bubbling port at the bottom-center of the upper phase, superficial gas flux = 2×10^{-4} m/s).

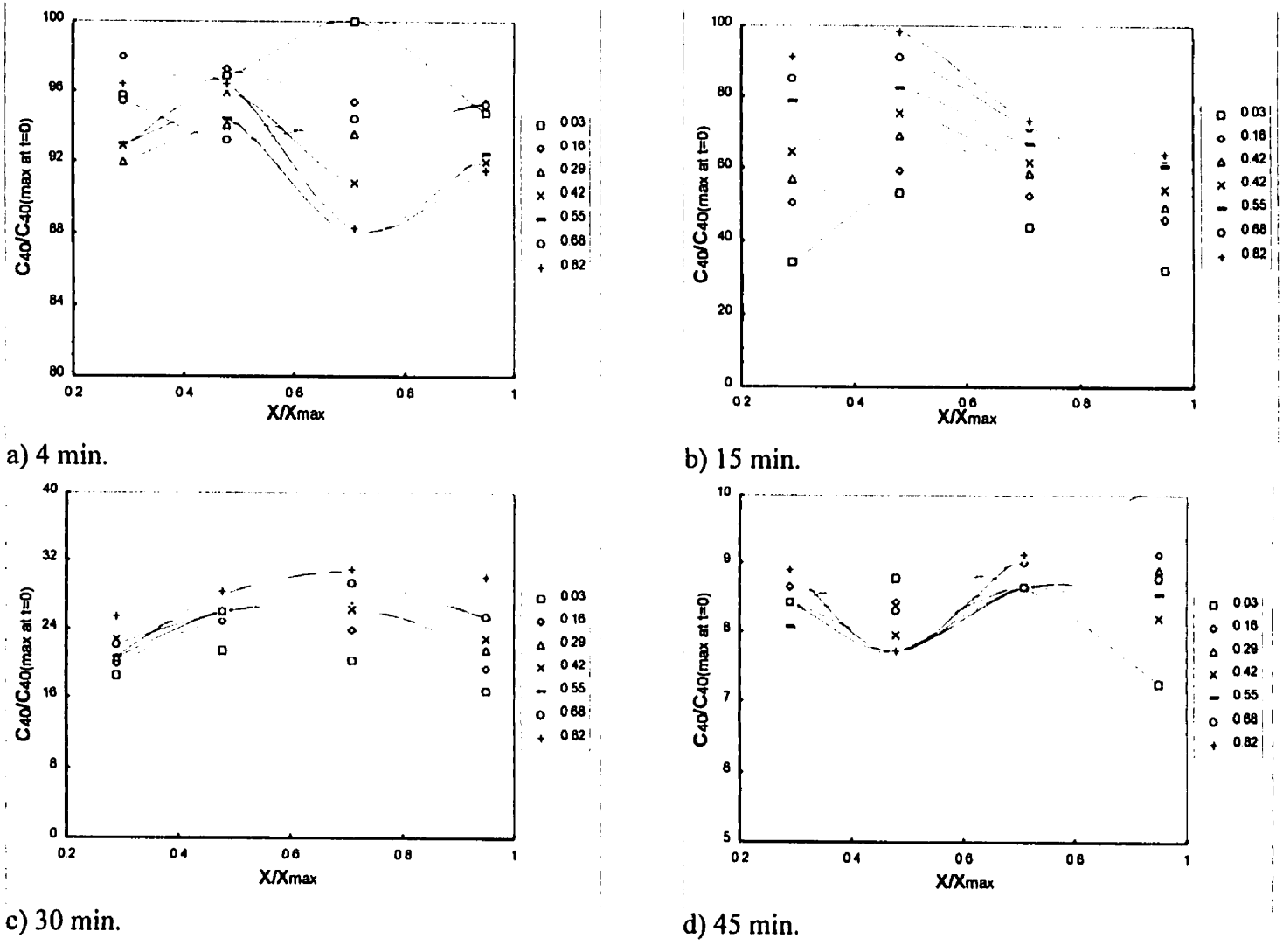

Figure 4.15 - The evolution of the percent relative number concentration distribution for 40 μm diameter drops across the width of the cell (Single bubbling port at the bottom-center of the upper phase, superficial gas flux = 2×10^{-4} m/s).

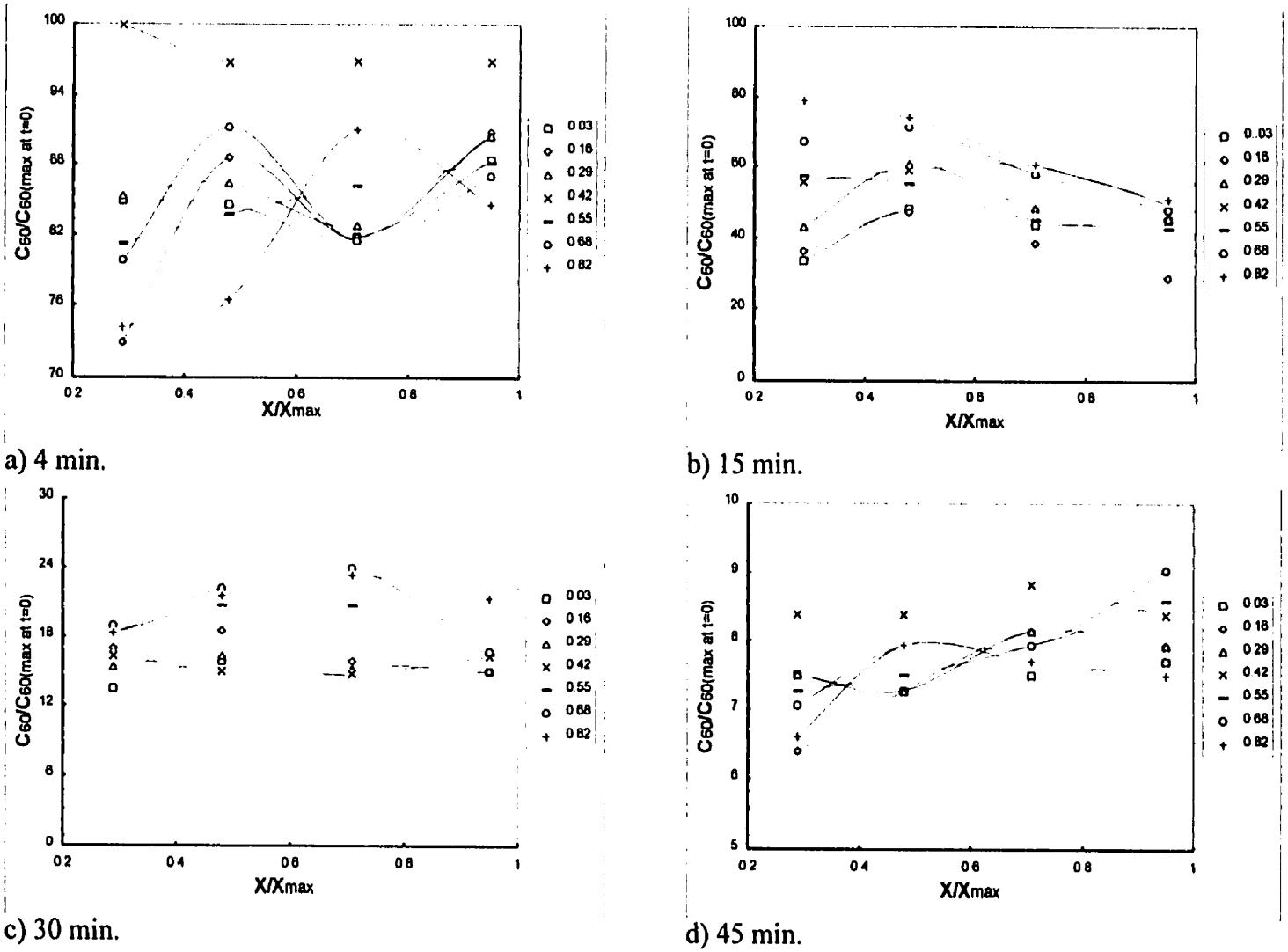

Figure 4.16 - The evolution of the percent relative number concentration distribution for 60 μm diameter drops across the width of the cell (Single bubbling port at the bottom-center of the upper phase, superficial gas flux = 2×10^{-4} m/s).

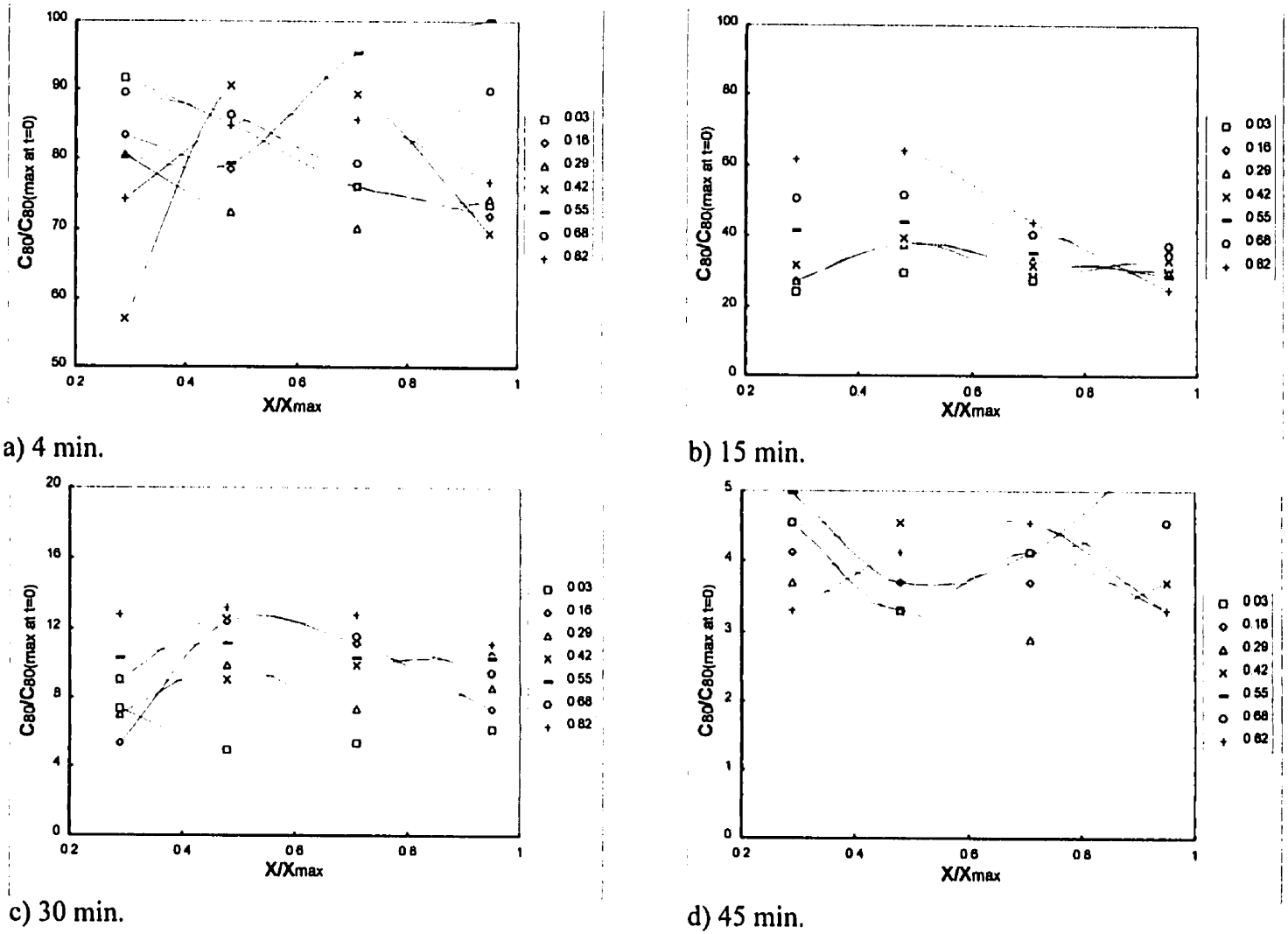

Figure 4.17 - The evolution of the percent relative number concentration distribution for 80 μm diameter drops across the width of the cell (Single bubbling port at the bottom-center of the upper phase, superficial gas flux = 2×10^{-4} m/s).

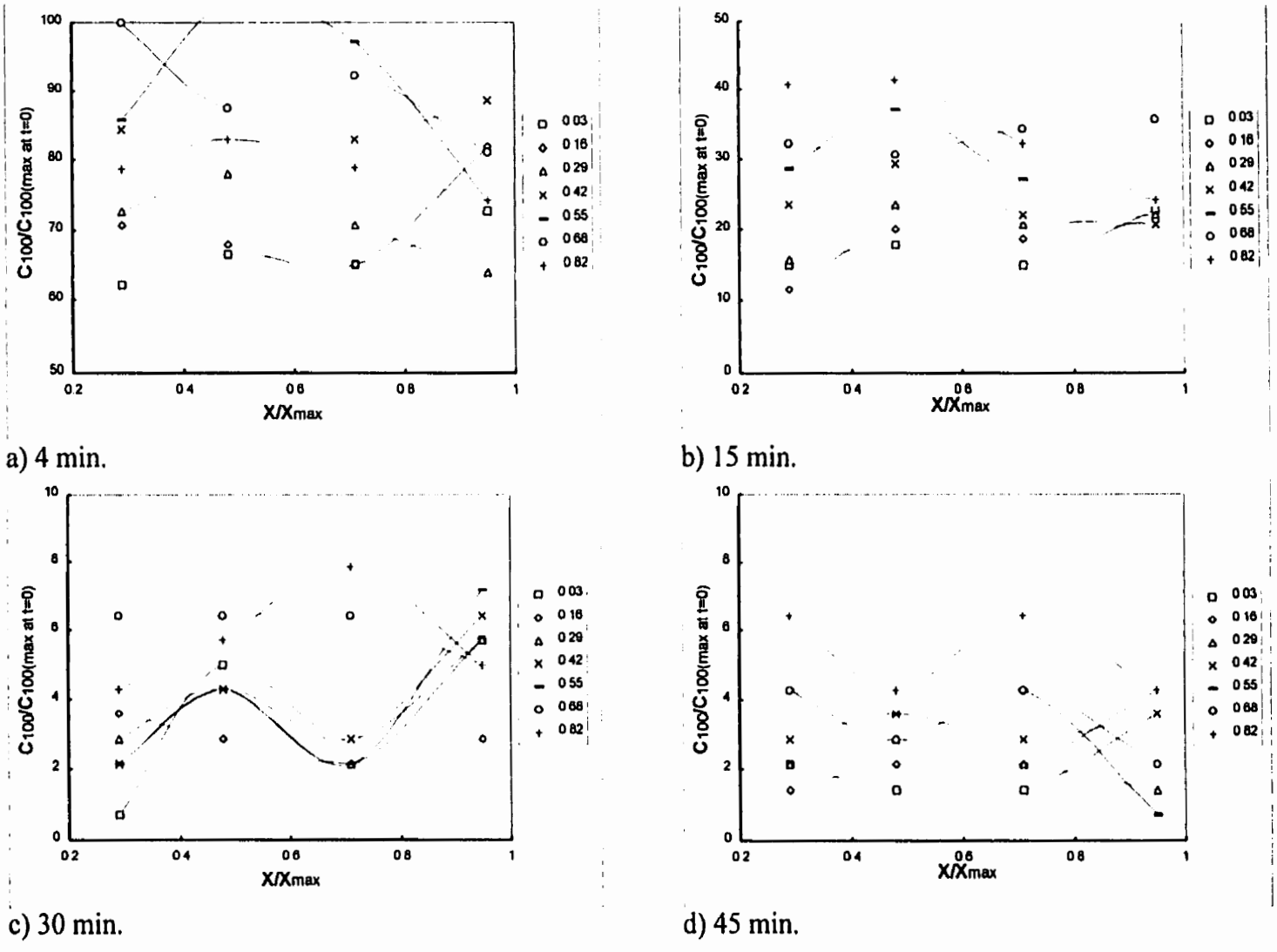

Figure 4.18 -The evolution of the percent relative number concentration distribution for 100 μm diameter drops across the width of the cell (Single bubbling port at the bottom-center of the upper phase, superficial gas flux = 2×10^{-4} m/s).

4.4.2 Drop concentration contours

Figures 4.19, 4.20 and 4.21 show the relative drop concentration contours inside the upper phase after 15 minutes of mild agitation (gas flux = $2x10^{-4}$ ms^{-1}). In general drops are concentrated at higher elevations with a centroid at X/X_{max} between 0.4 and 0.5. Large spatial drop concentration variation along the upper phase are evident. A small additional zone is present down near the side wall with higher concentration than adjacent regions. This is shown most clearly in Figure 4.21 where the relative

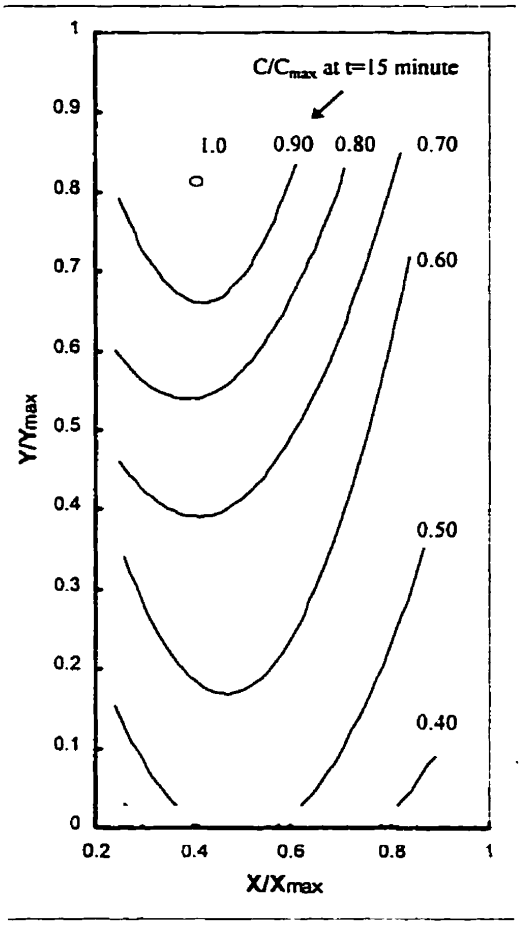

Figure 4.19 -Overall relative number concentration contours for drops between 10-110 μm in diameter in right half of the upper liquid phase (15 min. after starting mild agitation).

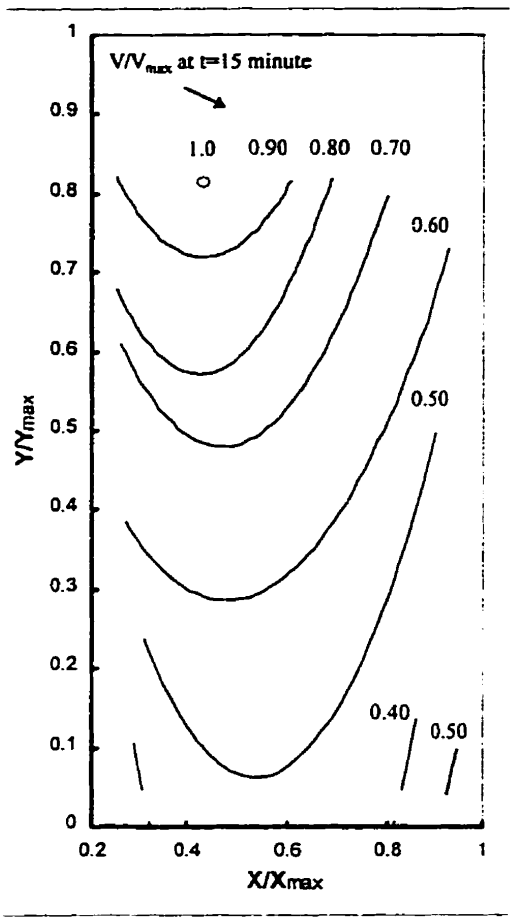

Figure 4.20 -Overall relative volume concentration contours for drops between 10-110 μm in diameter in right half of the upper liquid phase (15 min. after starting mild agitation).

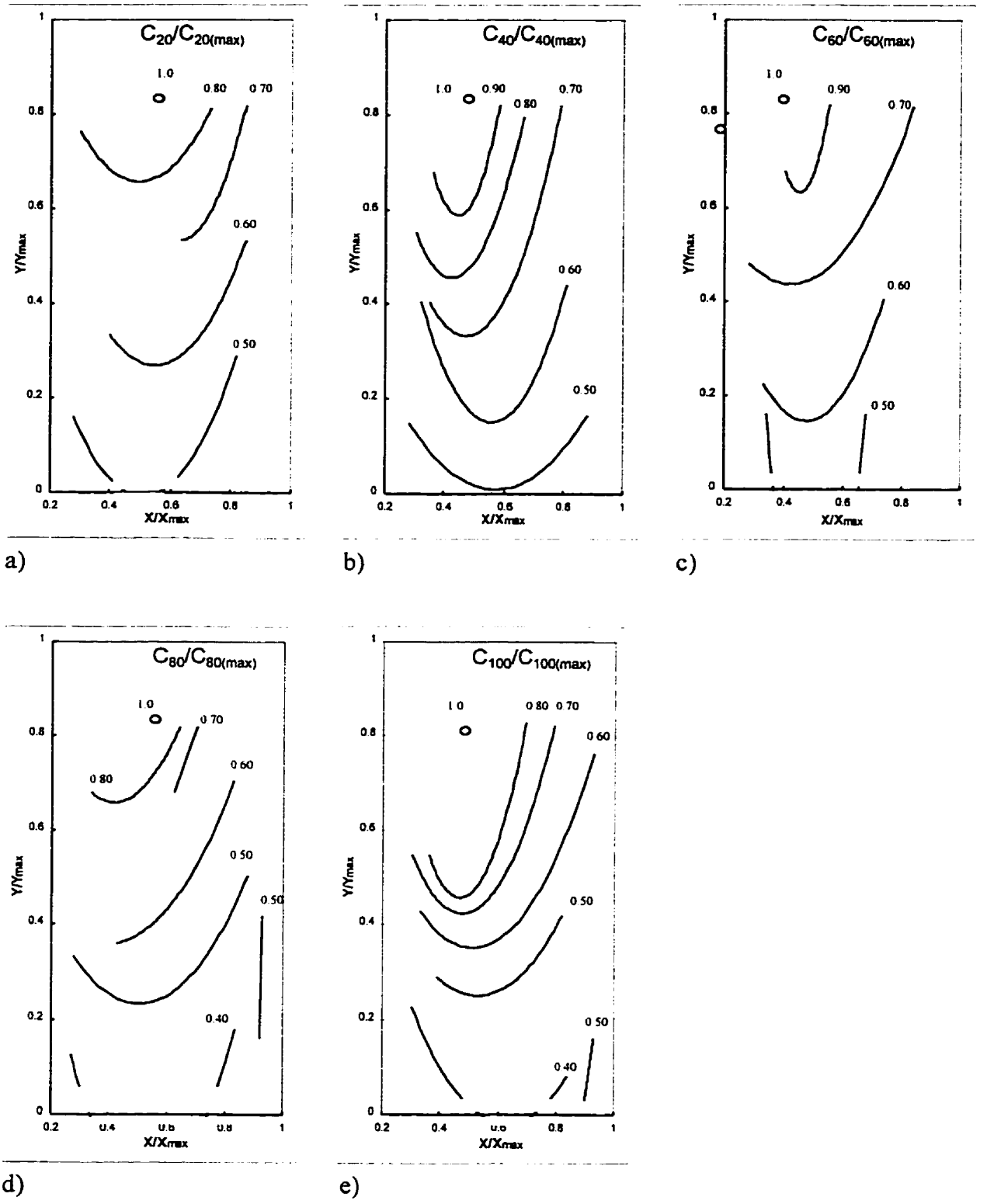

Figure 4.21 - Relative drop number concentration contours for different size ranges in the right half of the upper liquid phase (after 15 min. mild agitation).

concentration contours by drop size range are shown. The relatively high concentration zone near the wall is most pronounced for large drops (Figures 4.21.d and 4.21.e). These important results provide a clear indication of how the circulation loops facilitate drop recovery. They appear to drive drops preferentially into a segment of the liquid-liquid boundary remote from the gas injection port which as a consequence of mathematical modeling , chapter 5, is to become known as the drop "capture zone".

Downward flow in the boundary near the side wall is an important aspect of this phenomenon. Han et al. (1994) measured the distribution of insoluble particles within a few millimeters of a tube wall in a downward flowing liquid in order to examine the effect of velocity gradients on particles less than a few hundred μm in diameter. Their experimental results showed that particles that are more dense than the liquid, concentrate near a solid surface depending on the density and size range of the particles and the flow speed. This lateral motion of particles is as a result of the velocity gradient that causes particles to rotate due to the external couple exerted upon them and they are pushed closer to the side wall. Generally, a drop close to the side wall experiences not only gravitational force and a drag force parallel to the stream velocity, but a lateral lift force as well, at right angles to the stream.

In this work, lateral velocity gradients arise remote from bubble ports in multiport cases and a velocity gradient is also established close to the side wall. One can expect that the drops within the wall boundary layer are pushed close to the side wall. Thus drops which are trapped in this region are transferred close to liquid-liquid interface. The observed concentration profiles reflect this effect. The horizontal boundary adjacent to the liquid-liquid interface also contributes to drop recovery in a similar manner.

4.5 Re-entrainment of small vs. large Drops

When drops close to the side wall reach the liquid-liquid interface, they can coalesce or get re-entrained. Re-entrainment of a drop by the continuous phase flow above the

liquid-liquid interface does not occur when the vertical component of external forces acting on the drop, moves the drop down to the interface before it reaches the bubble street. Re-entrainment of drops that reside on the interface was not observed.

4.6 The effect of gas flux on fine drop recovery

Figures 4.22, 4.23 and 4.24 show the effect of gas flux on fine drop recovery. Results from individual experiments have been normalized for the sake of comparison as the initial concentrations varied somewhat. It should be noted however that great care was taken to establish initial conditions with minor variations for each experiment. As seen in all three figures, the most favorable gas flux appears to arise at about 5.0×10^{-4} *m/s* initially and the highest drop recovery rate is attained by reducing gas flux, on both a number and a volume basis as drop recovery proceeds.

Additional insight can be gained by investigating the effect of gas flux on the recovery of drops in specific size ranges (Figures 4.24.a-e). The optimal gas flux for all five size ranges is similar. Further, at the optimal gas flux, the recovery rate for drops in all five size ranges is also similar. This contrasts dramatically with the standard settling case, where drop recovery exhibits a strong size dependence.

It is not clear why the optimum gas flux decreases at long times. One can speculate on the role of the concentrated dispersion region in the boundary layer adjacent to the liquid-liquid interface and near the side wall, but it was not possible to measure drop concentrations in these regions (within 2 mm of the interfaces). At longer settling times it is anticipated that the concentration in these boundary layers decreases thus decreasing the apparent viscosity of the dispersion locally. At lower apparent viscosities, a thinner boundary layer with higher velocity is obtained for a fixed gas flux. The higher velocity close to the liquid-liquid interface gives less time to drops to travel down toward the interface under gravity. Thus lowering gas flux provides a calmer regime of flow for fine drops to reach the liquid-liquid interface. The velocity gradient close to the liquid-liquid

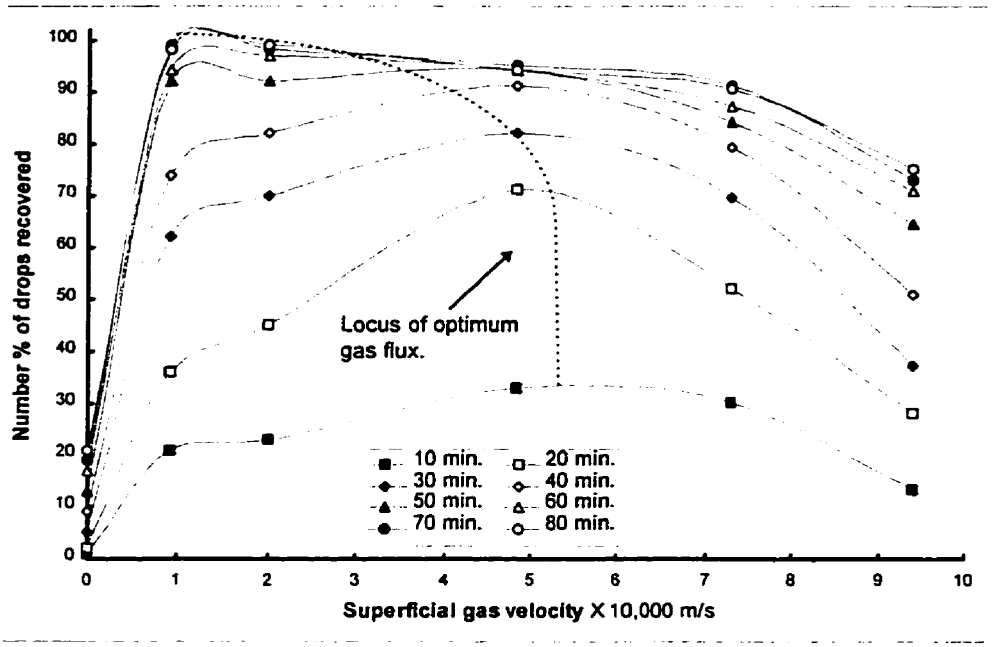

Figure 4.22 -The effect of gas flux on the overall recovery of fine drops (number %) as a function of time (center gas injection).

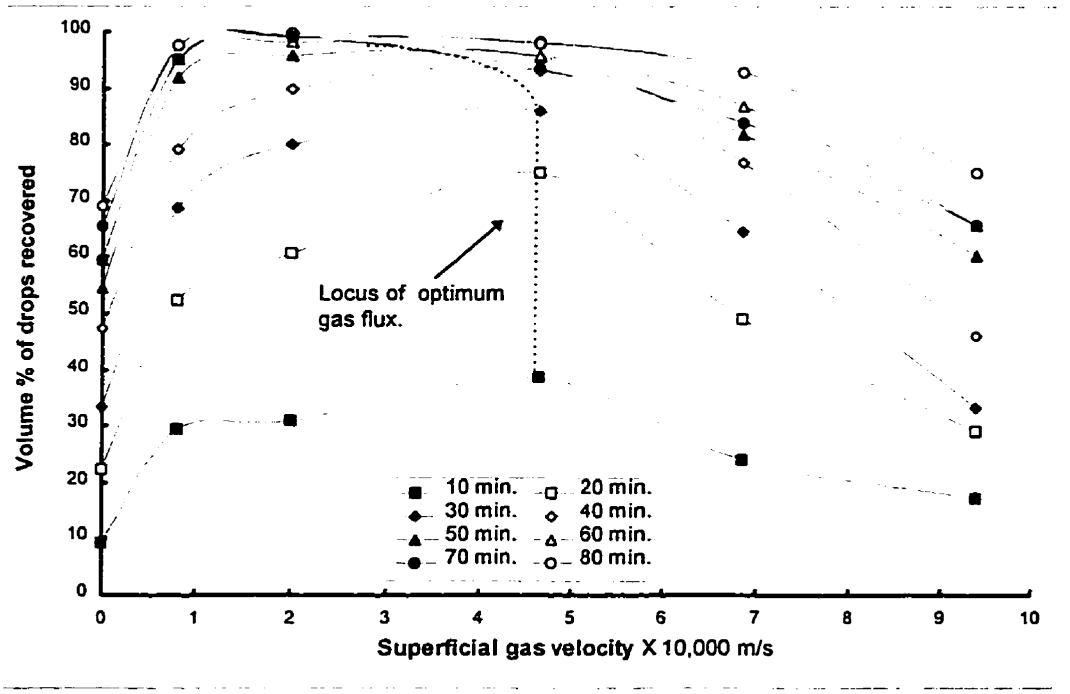

Figure 4.23 -The effect of gas flux on the overall recovery of fine drops (volume %) as a function of time (center gas injection).

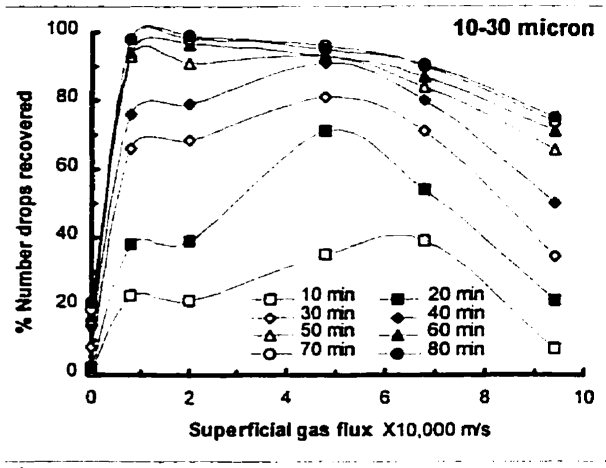

a)

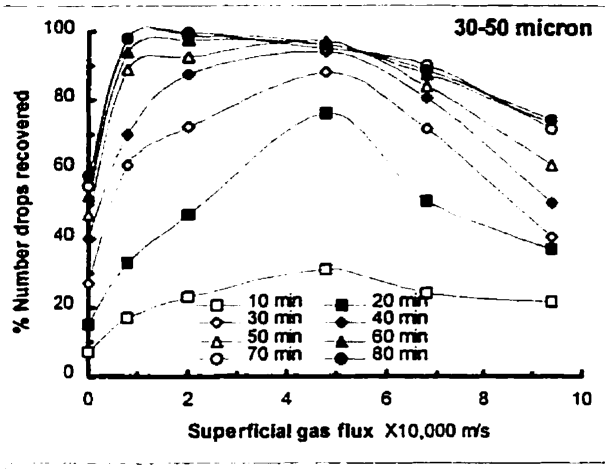

b)

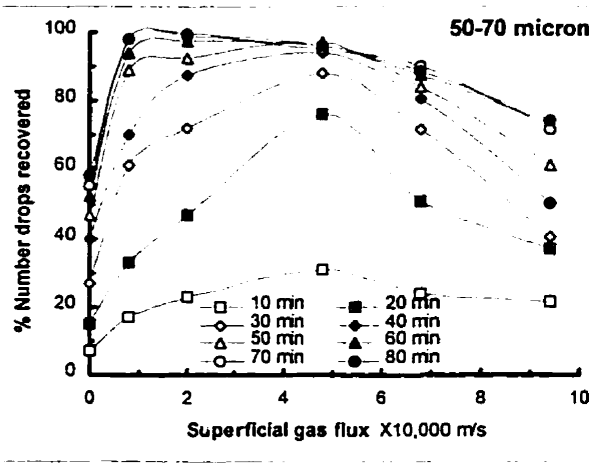

c)

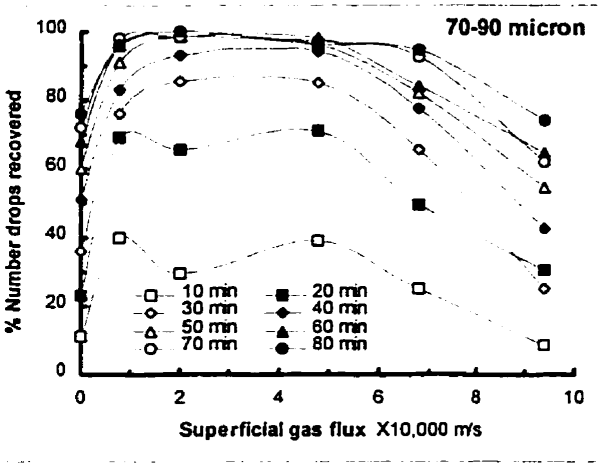

d)

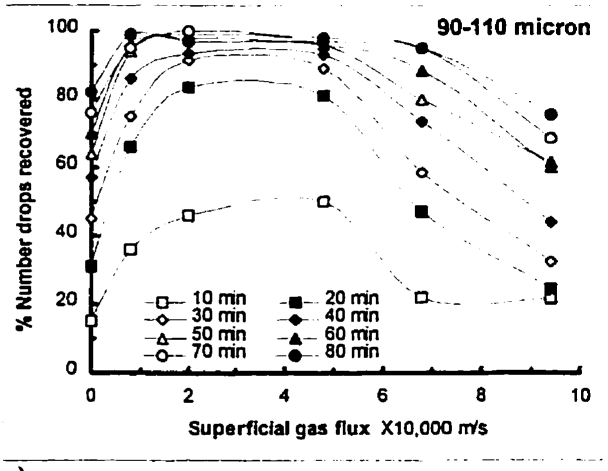

e)

Figure 4.24 - The effect of gas flux on the recovery of different drop size ranges as a function of time (center bubble injection).

interface also causes drop spinning which acts against gravity and drops are pulled down slower. This issue is discussed in more detail in chapter 5.

4.7 Summary

The results of these experiments clearly show that drop liquid-liquid interface interaction is the primary mechanism for fine drop recovery in batch gas-agitated liquid-liquid dispersions. Large-drop small-drop coalescence is shown to be a secondary mechanism. One of the key findings is that fine drop recovery is largely independent of drop size at the optimum gas flux and that the rate of drop recovery is significantly greater than under the influence of gravity alone. It would appear that circulation loops are quite efficient at transporting drops from the bulk to the liquid-liquid boundary layer, and that the transport process is not sensitive to drop size.

A physical picture of this transport process emerges from the experimental data. Circulating drops regardless of size enter the bubble street at random locations below the eye of the circulation loops and emerge from the bubble street close to the liquid-gas interface. A significant fraction of the emerging drops then follow the streamlines within the shear boundary layers adjacent to the wall and liquid-liquid interface where they coalesce with the lower liquid phase. The importance of these boundaries is addressed in chapter 5.

In the next chapter we explore our understanding of the physics of drop movement in the experimental velocity field shown in Figures 4.11 and 4.12 where emphasis is placed on the role of dispersion mixing in the bubble street and the flow profile adjacent to the liquid-liquid interface in the delivery of drops to the lower liquid phase.

5 PREDICTION OF DROP CONCENTRATION PROFILES AND DROP RECOVERY RATES

5.1 Introduction

Computational fluid dynamics is an important tool in the investigation of multi-dimensional two-phase flow. Phenomenological models have been used widely to describe such flows, but these models are not well suited for scale up and design in general, since they require prior knowledge of the flow structure. For single-phase flows analytical and/or numerical solutions of the fluid mechanics equations are available. These solutions are supported and/or extended by experimental results yielding basic information for specific cases. Such information is not available to the same extent for two phase flows because analytical and/or numerical treatments of the basic two-phase flow equations are not readily available. This applies to two-phase flows in general and to bubble-driven liquid flows in particular. Because of this, bubble-driven liquid flows are not readily predicted.

The initial goal of this modeling work was to calculate the bubble induced flow field in the upper liquid phase in the absence of fine drops and then to track the trajectory of drops introduced at arbitrary positions based on the velocity field obtained. Such computations were expected to shed light on the mechanism(s) involved in the recovery of drops at the liquid-liquid interface and on the spatial drop concentration distributions. Spatial drop concentration distributions can only be predicted accurately if the flow structure is available prior to drop trajectory calculations. Thus the model was simplified and a two dimensional drop trajectory model was imposed on an experimental velocity field. The flow field selected corresponds to that induced by center bubble injection at a gas flux of 2×10^{-4} *m/s* as illustrated in Figure 4.9.

5.2 Upper liquid phase flow field

A computer code was written to interpolate the flow field velocities between the 28 experimental grid points and to extrapolate the flow field to the boundaries. The experimental velocities are reported in Figure 5.1 where the x any y axis origins are centered on the bubble injection port. To extrapolate the flow field to the bubble street and gas-liquid boundaries where it was not possible to make velocity measurements, the mass conservation equations in the vertical and horizontal planes were applied to the experimental data to obtain values for $u(y)$ and $v(x)$ at the center of the bubble street and at the gas-liquid interface (equations 5.1).

$$\int_0^{Y\,max} u(y)dy = 0 \qquad \text{and} \qquad \int_0^{X\,max} v(x)dx = 0 \qquad 5.1$$

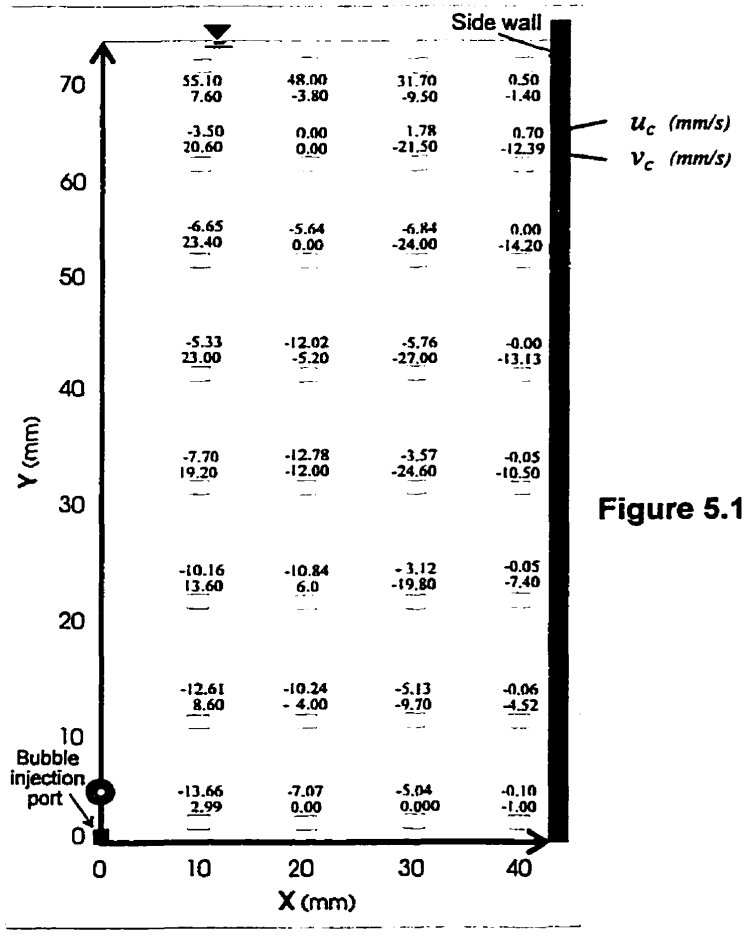

Figure 5.1 - Experimental velocity distribution inside the upper liquid phase (Gas flux = $2x10^{-4}\ ms^{-1}$).

The velocities at the wall and liquid-liquid interface were assumed to be zero. Thus the computational flow field is based on a total of 60 grid points. The model uses linear interpolation to obtain velocities at intermediate points. To compute the velocity at an arbitrary point *(x,y)* which falls between the grid points let $x_i \le x \le x_{i+1}$, *and* $y_i \le y \le y_{i+1}$, as shown in Figure 5.2. The symbol □ indicates points at which velocities are available. The model first interpolates linearly through f_{ij} and $f_{i+1,j}$, and through $f_{i,j+1}$ and $f_{i+1,j+1}$, to obtain approximations f_A and f_B to $f(x,y)$ at the point A and B. Then it interpolates linearly through f_A and f_B to obtain the final approximation for $f(x,y)$ given in equation 5.2.

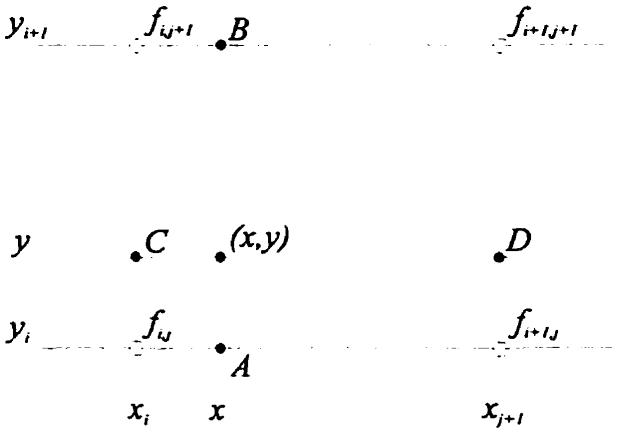

Figure 5.2 -Illustration of linear interpolation in two dimensions.

$$f(x,y) \cong (1-\alpha)(1-\beta)f_{ij} + \beta(1-\alpha)f_{i,j+1} + \alpha(1-\beta)f_{i+1,j} + \alpha\beta f_{i+1,j+1} \qquad 5.2$$

where,

$$\alpha = (x - x_i) / (x_{i+1} - x_i) \qquad 5.3$$

$$\beta = (y - y_i) / (y_{j+1} - y_j) \qquad 5.4$$

are weighting factors.

5.3 Drop trajectory Computation Procedure

This section describes how trajectories for individual dispersed phase drops are modeled in detail. The modeling approach is based on the inertia, hydrodynamic drag, lift and gravity forces applied to dispersed phase drops.

5.3.1 Overview of dispersed phase modeling procedures

The initial position, velocity and the size of a drop must be defined. These initial conditions, along with other inputs defining the physical properties of the dispersed phase, are used to initiate trajectory calculations. The trajectory calculations are based on a force balance on the drop using the local continuous phase conditions as the drop moves through the flow. This force balance equates the drop inertia with the forces acting on the drop, and can be written as:

x-direction

$$-F_{d_x} = 6\pi \mu_c r_d u + \frac{V\rho_c}{2}\frac{du}{dt} + 6r_d^2\sqrt{\pi \rho_c \mu_c}\int_{-\infty}^{t}\left(\frac{du}{dt}\right)_{t=s}\frac{ds}{\sqrt{t-s}} \qquad 5.5$$

y-direction

$$-F_{d_y} = -g\Delta\rho V + 6\pi \mu_c r_d v + \frac{V\rho_c}{2}\frac{dv}{dt} + 6r_d^2\sqrt{\pi \rho_c \mu_c}\int_{-\infty}^{t}\left(\frac{dv}{dt}\right)_{t=s}\frac{ds}{\sqrt{t-s}} \qquad 5.6$$

These are the equations for the unsteady motion of a rigid particle in creeping flow. The solution to this equation was developed by Basset (1888) with refinements by Landau and Liftshitz (1959). The first term of equation 5.5 is the Stokes drag for steady motion at the instantaneous velocity. The second term is the "added mass" or "virtual mass" contribution which arises because acceleration of the particle requires acceleration of the adjacent fluid. In general, the instantaneous drag depends not only on the instantaneous velocities and accelerations, but also on conditions which prevailed during development of the flow. The final term includes the "Basset history integral", in which past

acceleration is included, weighted as $(t\text{-}s)^{1/2}$, where $(t\text{-}s)$ is the time elapsed since the past acceleration. The form of the history integral results from diffusion of vorticity from the particle.

Due to the possible impact of lift on dispersed drops close to the side wall and the liquid-liquid interface, lift force was also included in the equation of motion. Equation 5.7 used in this program was developed by Saffman (1965) who showed that the lift force (for the x-direction) applied to a sphere rotating in a fluid in simple shear is given by:

$$F_{L_x} = 1.615\mu_c r_d v_c \sqrt{Re_{G_y}} \qquad 5.7$$

where

$$Re_{G_y} = G_y r_d^2 / \upsilon \qquad \text{and} \qquad G_y = \partial v_c / \partial x \qquad 5.8$$

As an equivalent expression arises for the Y-direction, the equations of motion using equation 5.5 and 5.6 in x and y directions are:

x-direction:

$$\frac{du_d}{dt} = \left(\frac{1}{(\rho_d + \rho_c/2)V}\right)\left(-6\pi\,\mu_c r_d u - 6r_d^2\sqrt{\pi\,\rho_c\,\mu_c}\int_{-\infty}^{t}\left(\frac{du}{dt}\right)_{t=s}\frac{ds}{\sqrt{t-s}} - 1.615\mu_c r_d v_c\sqrt{Re_{G_y}}\right)$$

5.9

y-direction:

$$\frac{dv_d}{dt} = \left(\frac{1}{(\rho_d + \rho_c/2)V}\right)\left(g\Delta\rho V - 6\pi\,\mu_c r_d v - 6r_d^2\sqrt{\pi\,\rho_c\,\mu_c}\int_{-\infty}^{t}\left(\frac{dv}{dt}\right)_{t=s}\frac{ds}{\sqrt{t-s}} - 1.615\mu_c r_d u_c\sqrt{Re_{G_x}}\right)$$

5.10

Equations 5.9 and 5.10 are solved by step-wise integration. Particle location and velocity are updated according to these equations of motion after each time step. Care was taken to ensure that any reduction in time-step value gave the same drop trajectory. For the case of a 100 μm diameter drop the time step was set at 10^{-4} seconds. For any time step larger than this value different drop trajectories result.

5.3.2 Boundary inputs for the dispersed phase

When a drop reaches a physical boundary, the model must possess a dispersed phase boundary condition to determine the trajectory at that boundary.

The boundary conditions are:

Gas-liquid interface:

drop-interface collision energy is absorbed and drops stay attached to the boundary until they fall under the influence of gravity. The interface acts as a non-rigid boundary therefore this appears to be a suitable assumption. Reflection was also considered but the impact on the results is not significant.

Side wall:

drops rebound off the side wall boundary with a change of sign in their horizontal speed. Alternatives such as setting the horizontal drop velocity to zero at the side wall were also considered. However this boundary condition remains inactive as results of a test simulation with 1000 drops of 100 μ*m* in diameter showed. By the end of this simulation all of the drops were recovered at the liquid-liquid interface. Not one of the drops touched the side wall.

Liquid-liquid interface:

drops are assumed to sorb when they contact the liquid-liquid interface. Contact terminates the trajectory calculation. Experimental observations showed that the liquid-liquid interface remained immobile during gas injection. The horizontal

velocities at this boundary were assumed to be zero. However conditions at this boundary play an important role in predicted fine drop recovery rates and this issue is addressed again in sections 5.4.2 and 5.4.5.2.

Bubble street:

Due to the turbulence arising in the bubble street, drops entrained into the individual bubble wakes are assumed to mix randomly. The radius of this mixing zone is unknown but bounded. The value is of the same order as the average bubble radius or ~2 *mm*. This is a key assumption in the model and cannot be verified experimentally due to its idealized nature. Drops entering the mixing

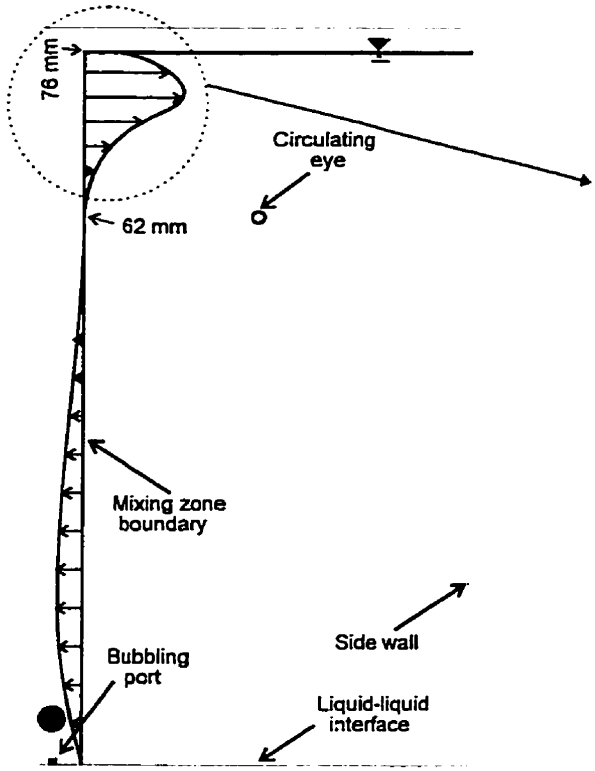

Figure 5.3.a -An annotated sketch of horizontal velocity distribution along the mixing zone boundary.

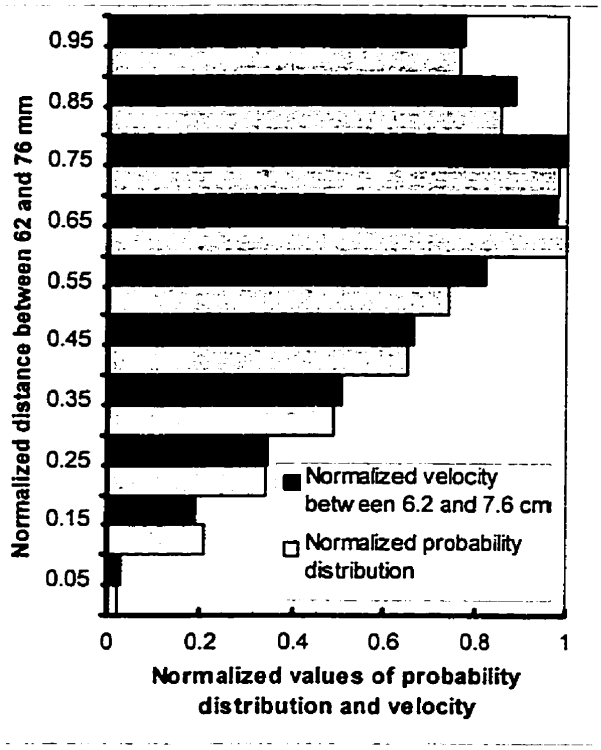

Figure 5.3.b - A comparison between normalized velocity distribution and normalized probability distribution at the point of re-entry of drops from the mixing zone into the circulation loops.

zone in the lower left of the flow field can emerge at the upper left where the horizontal velocity changes sign (Figure 5.3.a). While individual drops emerge at random points in that interval, on average, they must follow the velocity profiles in order to ensure uniform drop concentration at the emergence plane. A distribution function was designed for this purpose and is shown in figure 5.3.b where the normalized velocity distribution above the circulating eye and the normalized probability distribution of 3000 emergence points generated by the program are compared.

Since the normalized velocity distribution is not a function of mixing zone bandwidth, the same random number distribution can be used for all the bandwidth values. The importance of this parameter is addressed in section 5.4.7.

5.3.3 Calculation procedures

Drop trajectories are computed by integrating the force balance on a drop. The effect of drops on the continuous phase is not considered. This is an adequate approximation when the dispersed phase is present at a low mass and momentum loading.

This computation procedure is expanded as follows:

- Interpolation of u and v at any x and y position prior to introduction of a drop;
- Introduction of the dispersed drop by calculating the drop trajectory starting from an arbitrary initial position;
- Calculation of the position of the drop after one time step;
- Interpolation of u and v at the new x and y position;
- Recalculation of the drop trajectory at each time step until the drop reaches the liquid-liquid interface, or a total time constraint is reached.

The detailed breakdown of the computer program is presented in Appendix A.

5.3.4 Time step

In the dynamic simulation of buoyancy driven flows, small time steps are required. For the present case when the time step is less than 10^{-4} seconds for a 100 μm diameter drop, the trajectory calculations are repeatable. The program was run in UNIX, on a SGI work station with 100 MHz processor and Iris operating system (version 5.3). The time to capture for a 100 μm diameter drop is about two minutes. The time varies depending on the output of the random number generator, and the extent of drop tracking information requested.

5.4 Numerical Results

5.4.1 Example drop trajectory

A typical trajectory for a 100 μm diameter drop, starting from $x=15$ *mm* and $y=62$ *mm*, is shown in Figure 5.4.a. The drop trajectory is elliptical with the centeroid at the upper center. All drops move in clockwise direction. The figure clearly shows that drops emerge from the bubble street above an elevation of 62 *mm*. An annotated sketch of the zone affected by the mixing action of bubbles is shown in figure 5.4.b. The boundary distinguishes inner orbits (unaffected by bubble induced mixing) and outer orbits (where drops enter and exit the mixing zone once per cycle). Once drops enter the outer orbits they do not return to inner loops.

As mentioned in section 5.3.2, the elevation that drops emerge from the mixing zone is specified by the random number generator. Only drops that are close enough to the gas-liquid interface enter the calm region at the bottom of the upper phase where they are recovered at the liquid-liquid interface. Drops otherwise recirculate. It is worth noting that for the sample calculation shown, over 74% of the drop recovery time is predicted to be spent in inner orbits. The impact of bandwidth (which defines the boundary of mixing zone) on drop recovery rate and the boundary between the inner and outer orbits is addressed in sections 5.4.5.1 and 5.4.5.2 respectively.

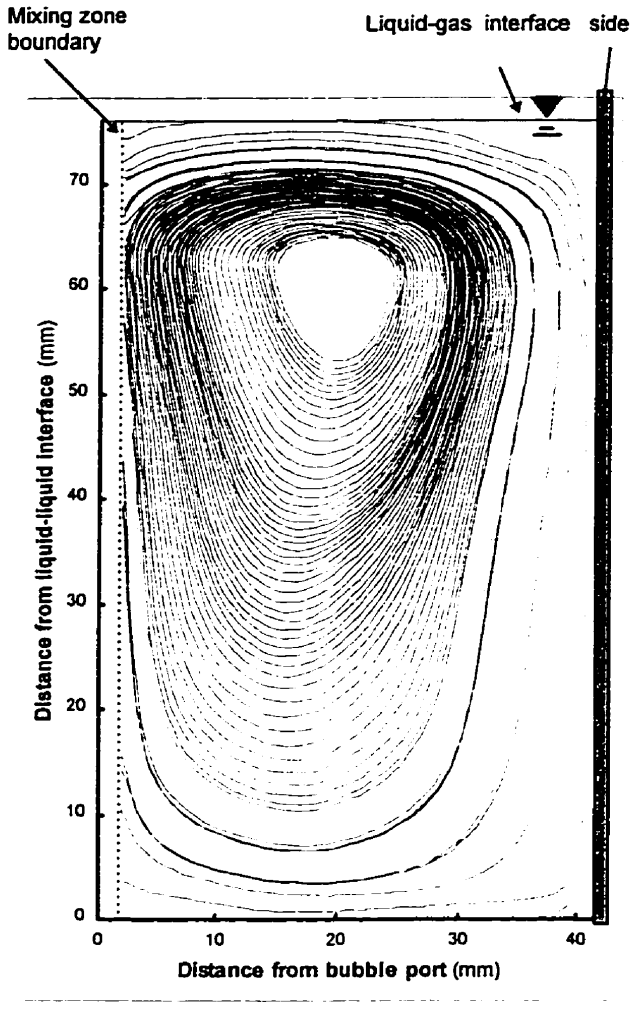

Figure 5.4.a -The trajectory of a 100 μm diameter drop in right half of the upper liquid phase (bandwidth = 2 mm, time to capture = 342 s).

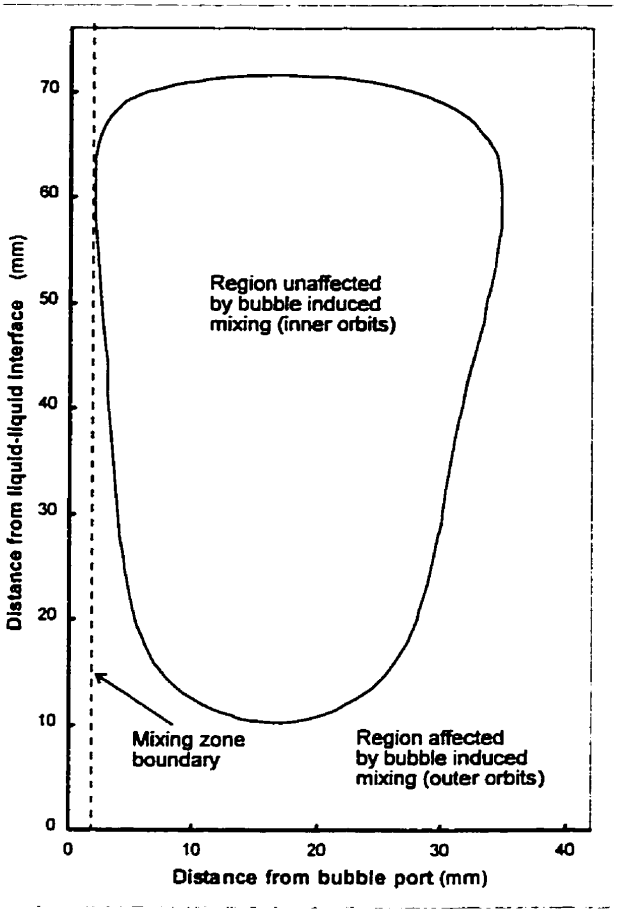

Figure 5.4.b - An annotated sketch of bubble induced mixing on the right half of the upper phase.

5.4.2 Capture zone

Drops exiting the bubble street may be close enough to the gas-liquid interface, so that their trajectory takes them to the liquid-liquid interface. Such trajectories define the boundary of the *Capture Zone* which varies with drop size. This zone is shown in Figure 5.5 for a 100 μm diameter drop. A portion of the capture zone boundary adjacent to the liquid-liquid interface falls outside of the range of the experimental data. Due to restrictions in measuring the velocities of drops close to the liquid-liquid interface, the

experimental velocity distribution within 2 mm of this boundary is not defined. Consequently, the predictions of the model are sensitive to the assumed continuous velocity gradient in this region and the velocity value assumed for the liquid-liquid interface. In the model, the velocity gradient close to this boundary is assumed to be linear with a zero velocity at the liquid-liquid interface. Higher order velocity gradients (e.g. polynomial velocity distribution functions) and non zero velocities at this boundary reduce the size of the capture zone and reduce fine drop recovery rates. The importance of this boundary is discussed in section 5.4.5.2.

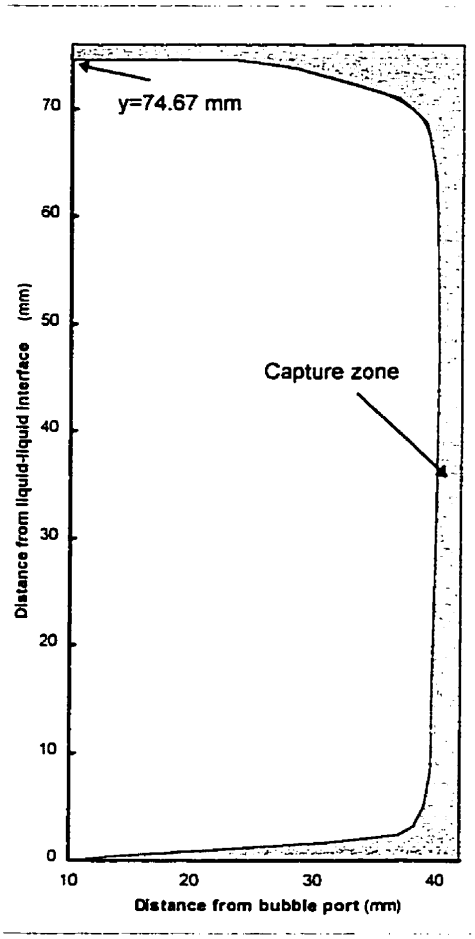

Figure 5.5 - The limiting trajectory of a 100 μm diameter drop, defining the capture zone (shaded area).

5.4.3 The effect of drop size on drop trajectory

Figures 5.6.a and b show the results of drop trajectory calculations for small and large drops in arbitrary inner and outer orbits. The starting positions for each pair of drops is

the same. Figure 5.6.a shows that larger drops in inner orbits move out slower than smaller drops. As one expects, large drops diverge from the streamlines under the influence of gravity more so than small drops. As a consequence the trajectories of large drops fall within the trajectories of small drops at high elevations. At low elevations, if there is sufficient time, the trajectories of large drops cross those of the small ones, as is clearly shown in Figure 5.6.b. The trajectories otherwise approach one another but do not cross before the drops return to the higher elevations. Therefore small drops move out of the inner orbits more quickly than large drops. An example calculation where the starting

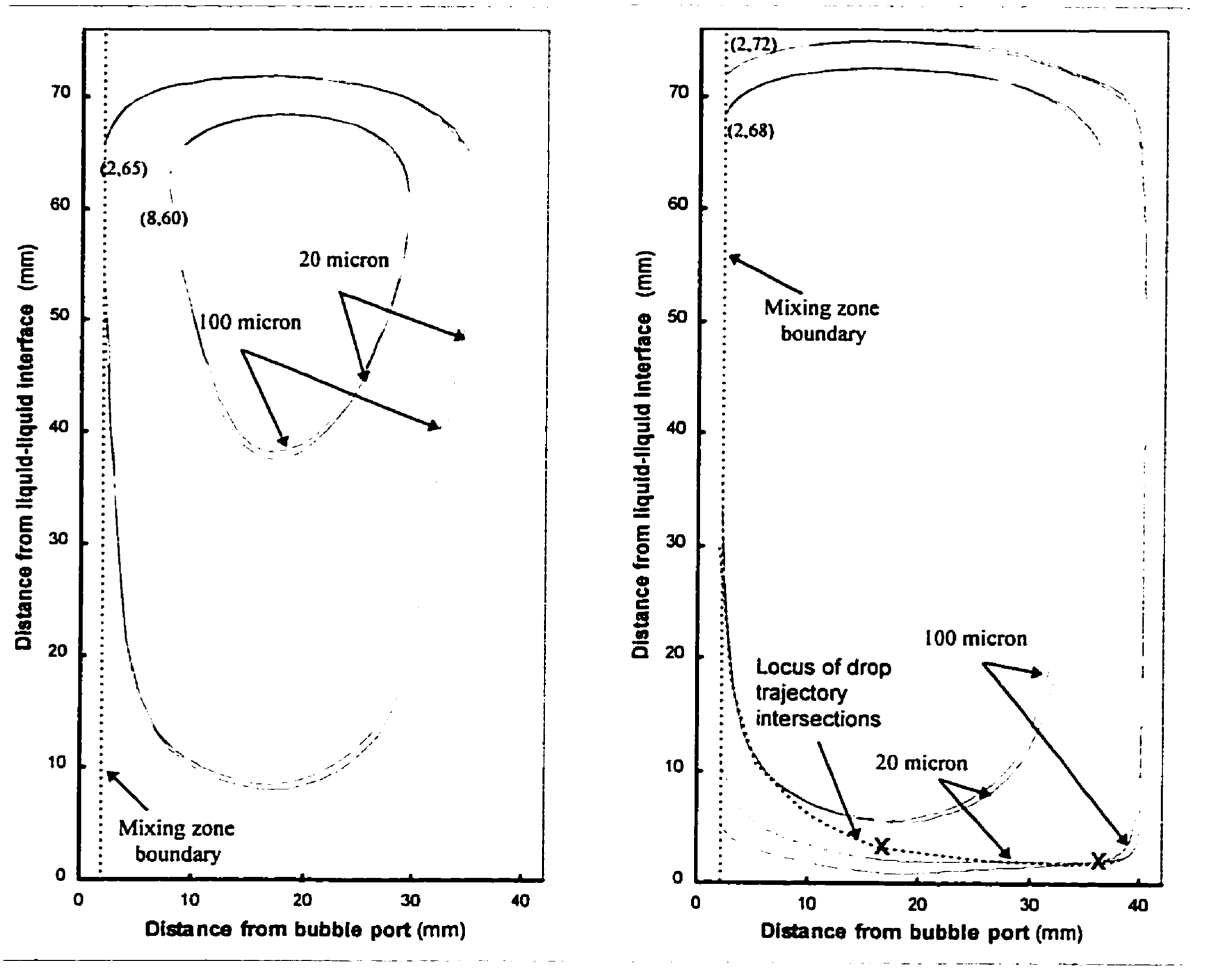

a) b)

Figure 5.6- Trajectories for 100 μm diameter drops and 20 μm diameter drops inside the, a) inner orbits and b) outer orbits. x marks the point of intersections of the trajectories for 20 and 100 μm diameter drops.

point for both drops is $x=10$ *mm* and $y=60$ *mm* reveals that a 20 μ*m* diameter drop is transferred to the outer orbits within 111 seconds whereas a 100 μ*m* diameter drop takes 181 seconds.

5.4.4 The effect of lift force on drop trajectory calculations

As discussed in section 2.4.1.3, if a particle moves in a non-uniform flow field, the flow field may induce drop rotation which in turn causes an additional force perpendicular to the main flow direction. Figure 5.7 shows the effect of lift force on the trajectory of a

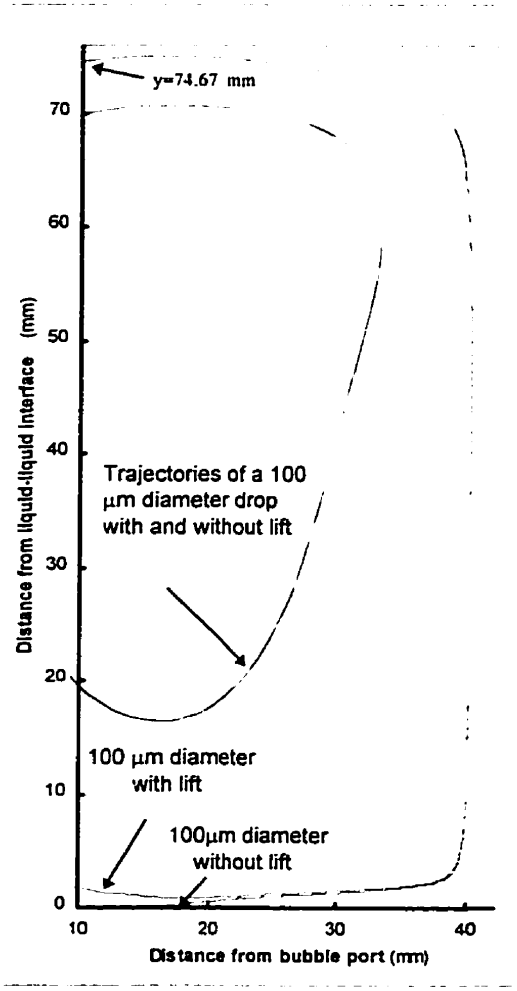

Figure 5.7 - A comparison between the trajectories of a 100 μm diameter drop, with and without the lift force for the inner and the outer orbit cases.

100 μm diameter drop. This figure shows that, the difference between the trajectories inside the inner orbits, with and without the lift is minor. But the effect appears to play a significant role in drop capture at the liquid-liquid interface. Since drops lag the fluid close to the liquid-liquid interface, the direction of lift force is toward the inner orbits and the direction of lift force close to the wall is toward the outer orbits. Thus the capture zone for 100 μm diameter drops is closer to smaller drops than would be expected based on gravity alone. In the absence of lift, the starting point for the capture zone is at 74.67 mm. This value drops to 74.65 mm without the lift. The difference is about 0.02 mm. This seems rather small to be significant but the two trajectories diverge close to the liquid-liquid interface. The lift force effect on smaller drops is expected to be less than for larger drops.

The type of flow between the faces of the viewing cell is expected to be Couette flow. Since the maximum velocities between the two faces, at any x-y coordinate, are on the central plane, drops are expected to move closer to this plane of reference. Larger drops are affected more by the lift force and tend to accumulate closer to the central plane. This additional force speeds up the movement of the larger drops to outer orbits, compared to the drop movement under circulation in two dimensional case. The lift force effect on different drop size in z-direction can not be predicted by the present model.

5.4.5 Mixing action of rising bubbles

5.4.5.1 Mixing zone bandwidth

As noted before, the bandwidth of the mixing zone was set at 2 mm for most of the simulations, i.e. drops crossing a vertical line 2 mm away from the center line of the bubble street are mixed randomly before they re-enter the circulation orbit. Figure 5.8 shows the parts of the upper phase that are unaffected by bubble induced mixing. By decreasing bandwidth, the portion of the upper phase affected by bubble mixing is decreased.

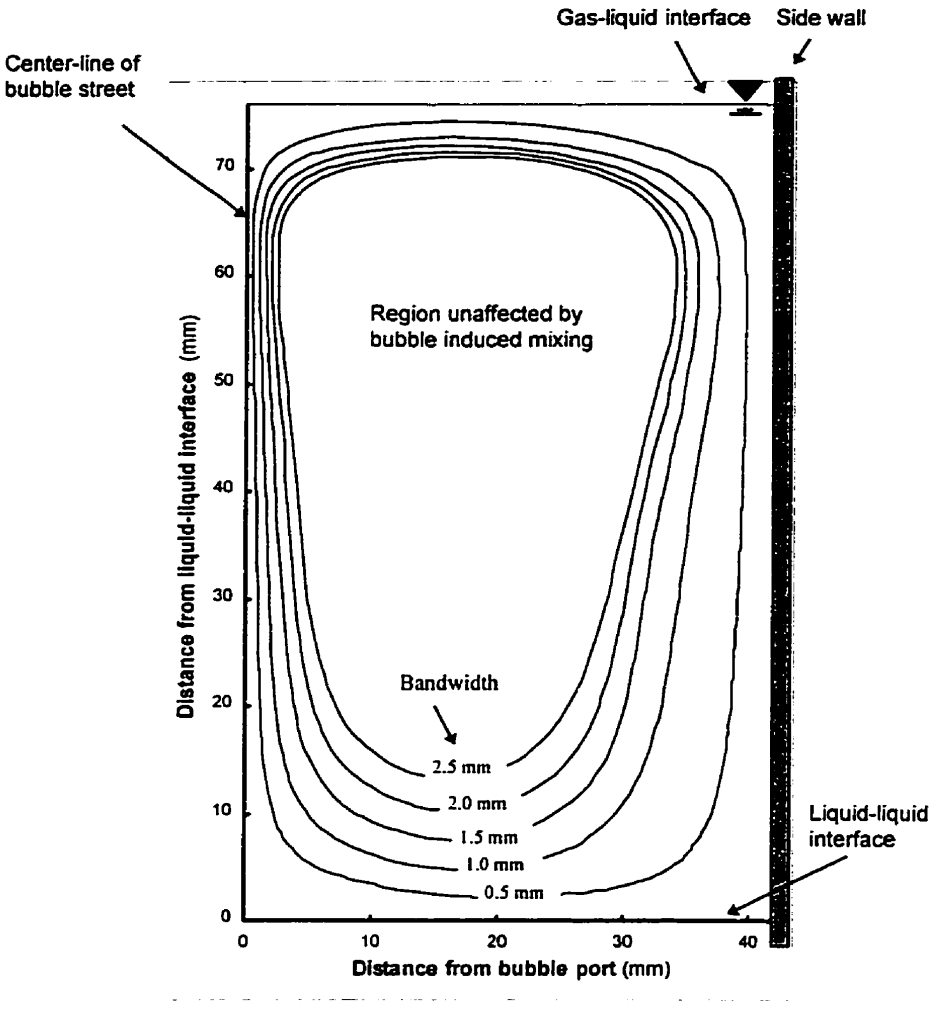

Figure 5.8 - The effect of variation of the parameter mixing bandwidth on the predicted region unaffected by the mixing action of the rising bubbles.

5.4.5.2 Predicted recovery rate for 100 μm diameter drops

In chapter 4 it was found that fine drop recovery where a single bubble port is employed (center gas injection) enhances drop recovery rates compared to gravity settling. This result was explored with the present model by comparing predictions obtained with equation 4.3. The program was run for 966 drops of 100 μm diameter located homogeneously in the experimental flow field. The rates of drop recovery were defined on the basis of the number of drops touching the liquid-liquid interface as a function of time. Figure 5.9 shows the results of computations for different mixing bandwidth values

on the recovery of 100 μm diameter drops and also the experimental equivalent drop recovery curves (Figures 4.5 and 4.6). The model shows a high rate of drop recovery for bandwidth values of ~2 mm compared with settling under gravity alone. As the value of bandwidth and the flow field are coupled experimentally, this set of computations reports a sensitivity analysis only. However for bandwidth values in the range of physical expectations, $1\ mm \leq bandwidth \leq 4\ mm$, it is encouraging that recovery rates are predicted in excess of those obtained with gravity settling alone. This result confirms that the assumption concerning the benefit of mixing in the bubble street is both realistic and an essential aspect of the recovery process.

A direct comparison with experimental results is difficult because of the explicit and implicit assumptions in the model. For example the model applies only to drops in the center-plane of the view cell and the gravity settling calculation applies to an unbounded

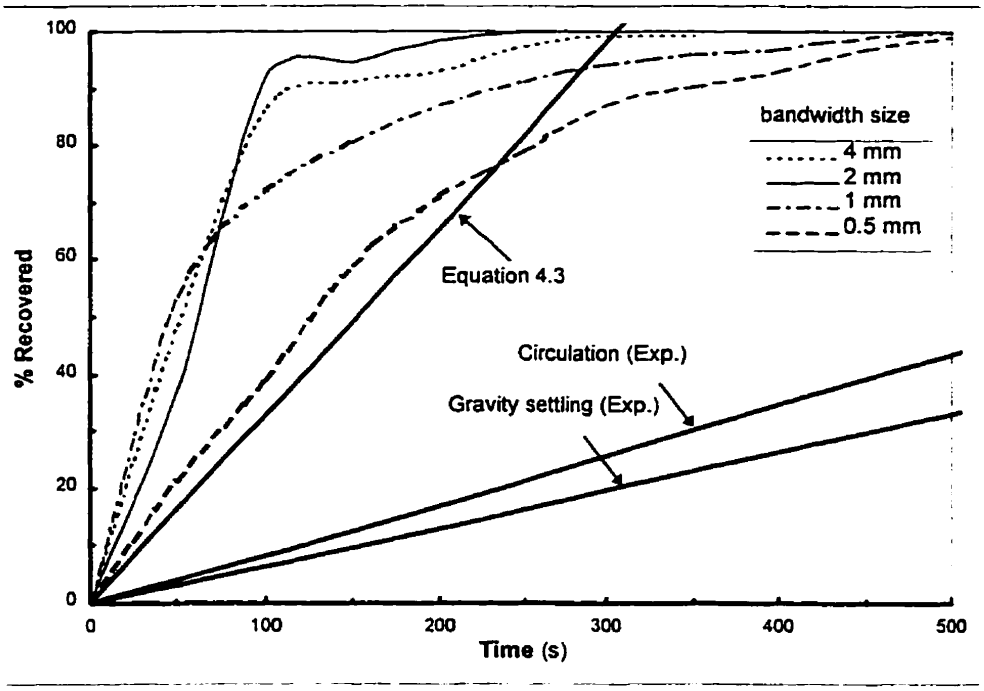

Figure 5.9 -The effect of mixing zone bandwidth on the recovery of 100 μm diameter drops using the current model compared with equation 4.3 and experimental results (center bubbling port at a gas flux of $2.0x10^{-4}$ m/s).

medium. Further, wall and electrostatic effects are ignored in the calculations. Despite the differences, these results confirm that circulation loops are an effective means for transporting drops to the liquid-liquid interface.

As mentioned in section 5.4.2, the exact nature of velocity profile close to liquid-liquid interface plays an important role with respect to fine drop recovery. For the limiting case where one simply extrapolates the horizontal velocity linearly to the boundary, based on the nearest adjacent grid points (2 mm and 12 mm), drop recoveries are reduced to those obtained under gravity settling (Figure 5.10). This is the worst case. Thus the boundary condition at the liquid-liquid interface is as important as the mixing in the bubble street with respect to fine drop recovery. For the values of velocities equal to half of the values obtained from extrapolations in the previous case, drop recovery rates approach those obtained assuming a linear gradient and a zero interface velocity. As the liquid-liquid

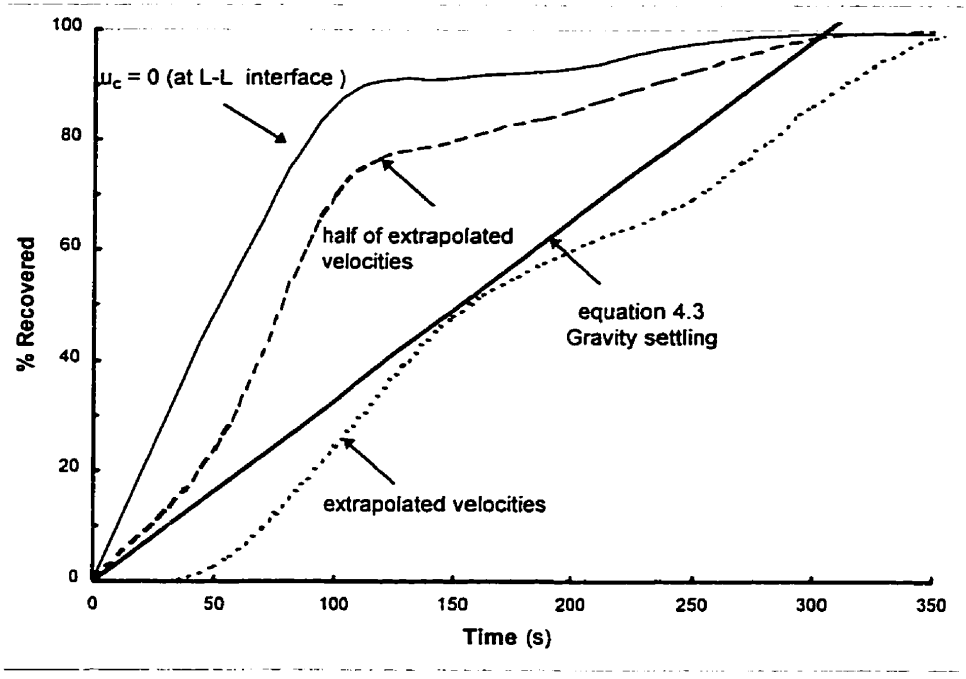

Figure 5.10-The effect of variations of velocities on liquid-liquid interface on the recovery of 100 μm diameter drops using the current model compared with equation 4.3 (bandwidth= 2 mm, gas flux= $2.0x10^{-4}$ m/s).

interface appears immobile during experiments, the model predictions are less sensitive to variation in this boundary condition than one might expect. However, these calculations suggest a possible limitation on the range of fluid properties where circulation would offer significant benefit with respect to fine drop recovery.

5.5 Predicted spatial drop concentration distribution for 100 μm diameter drops

In order to predict the spatial drop concentration distribution trajectories for 12382 drops of 100 μm diameter were computed. This proved to be a difficult task because the individual drop trajectories had to be followed consistently using time steps of 10^{-4} to

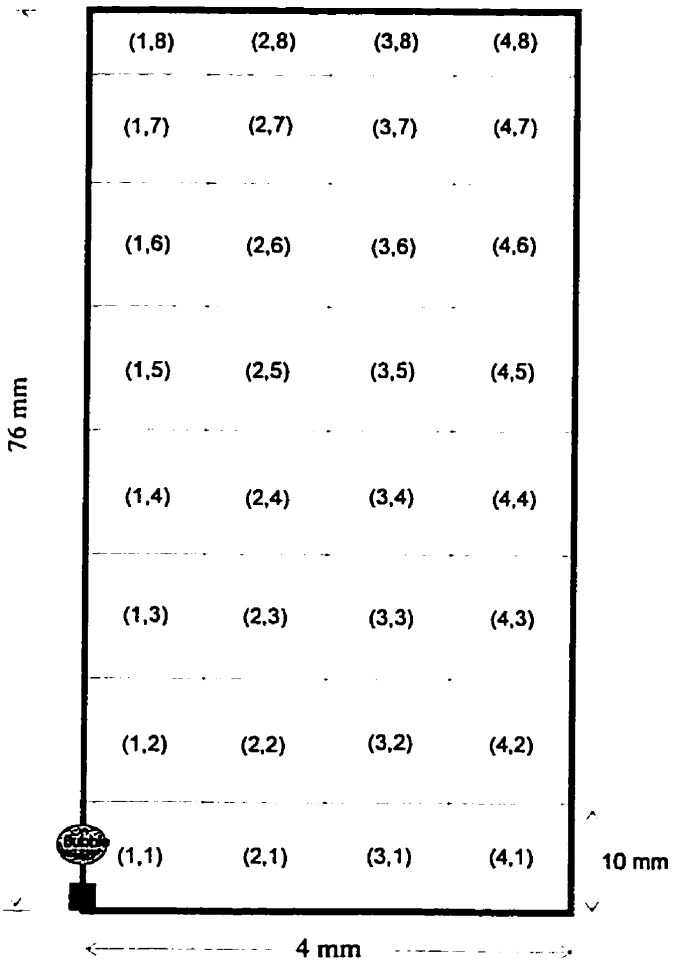

Figure 5.11 -Grid scheme for drop binning.

ensure stable results. A typical CPU time per simulation on a SGI workstation with 100 MHz processor was about 15 hours. The program calculates the trajectory of every drop and records positions at 30 second intervals. The drops are then binned as shown in Figure 5.11.

Drop concentrations presented in figure 5.12 exhibit a well defined maximum, midway between the bubble street and the wall (gray region), and in the lower wall region adjacent to the liquid-liquid interface. This is in qualitative agreement with the experimental results for 100 μm diameter drops (see figures 4.18.a-d). The three

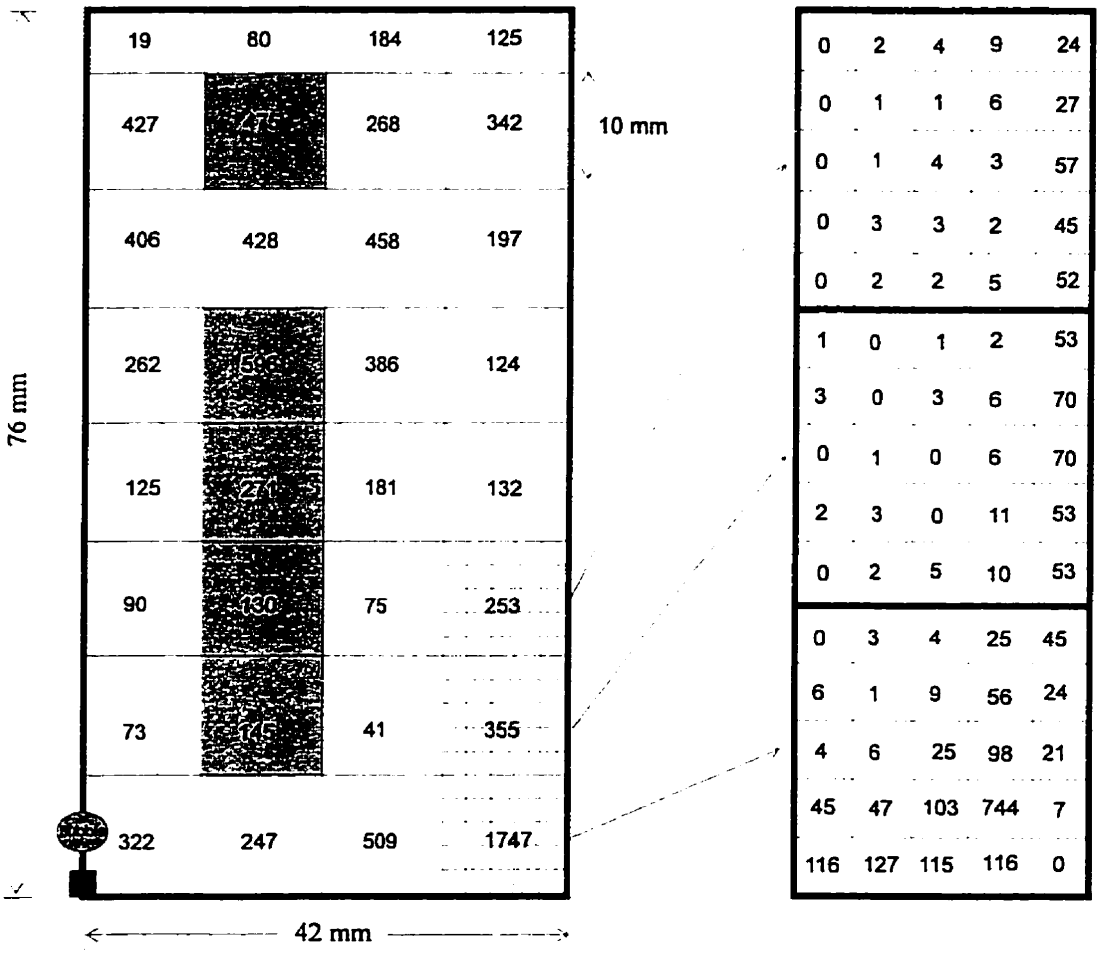

Figure 5.12 -The spacial concentration distribution of 100 μm diameter drops after 30 seconds. The total number of drops left is 9473 (12382 drops initially) bandwidth is 2 mm.

elements at the lower right corner are refined in figure 5.12 to show the distribution of drops close to the wall and the liquid-liquid interface. Since the measurement point in the experiments was more than 2 *mm* away from the liquid-liquid interface and the side wall, only the edge of this high drop concentration zone was detected experimentally.

5.6 Summary

The results of the numerical modeling presented here are in qualitative agreement with the experimental work. Key features of the flow field and their roles in drop recovery are identified. These features include:

- Circulation loops generated by rising bubbles transport fine drops close to the liquid-liquid interface.

- Bubble street randomization is a critical aspect in the drop transport process.

- Drop recovery rate is dependent on the continuous phase velocity profile adjacent to the liquid-liquid interface. When this boundary is immobile the rate of drop recovery is greatest.

- The lift force effect retards drop capture at the liquid-liquid interface. This may account for the similarity in recovery rates of 100 μm diameter and 20 μm diameter drops observed experimentally, because 20 μm diameter drops are less affected by lift than 100 μm diameter drops.

- The numerical model shows that far from boundaries, smaller drops are shifted to outer orbits faster than larger drops. The gravity force was found to be the parameter that causes this phenomenon. Close to liquid-liquid interface gravity facilitates large drop capture vis-a-vis small drops. This trade off may account for the similarity of drop capture rates regardless of size.

- Stokes law based predictions and the model predictions overestimate measured recovery rates by a factor of 6 relative to the experimental data. Over prediction was expected because the model only considers drops in the central plane of the cell and electrostatic and other forces were not considered. No attempt has been made at this time to fit the model to the experimental data.

6 CONCLUSIONS

This work stresses the combined use of experimental and computed results for the study of drop recovery from batch gas-agitated liquid-liquid dispersions. It provides a clear explanation for an apparently counter-intuitive empirical result, i.e., that agitation facilitates the settling of drops from dispersions.

A comprehensive search of the literature showed that detailed information on the liquid flow and spatial drop concentration distribution in batch gas-agitated liquid-liquid systems was unavailable. A video technique was employed to provide the missing experimental data and to identify the key mechanisms related to drop recovery from such dispersions. Computer modeling was employed to assess details which could not be evaluated experimentally. Although the model over-predicts drop recovery rates it confirms our understanding of the physics of such flows. The model is an idealized one and the computed results are viewed as qualitative. No effort was made to fit the model results to the experimental data. The principal conclusions are:

1. Enhanced drop liquid-liquid interface interaction is the primary mechanism for fine drop recovery in batch gas-agitated liquid-liquid dispersions.

2. Large drop-small drop coalescence is a secondary mechanism with respect to the recovery of fine drops in such systems.

3. There is no indication that drops in the size range of interest (drops in 20 μm-100

μm in diameter) coalesce in wakes.

4. Random agitation of the less dense liquid phase hinders drop recovery, while slow circulation enhances drop recovery rates significantly.

5. The combined effects of mixing in the bubble street and circulation loops transport drops from the bulk to the liquid-liquid interface efficiently. This transport process is largely independent of drop size particularly at optimum gas flux.

6. There is an optimum number of circulation loops per unit length of interface and an optimum gas flux.

7. At the optimum gas flux the recovery rates of drops in the 20 to 100 μm size range are approximately equal and 5 times higher than corresponding standard gravity settling cases.

8. The optimum gas flux is apparently a function of dispersion concentration. At high fractional recoveries, the optimum gas flux declines regardless of drop size.

9. Computations show that small drops move out of the core of the circulation loop faster than larger drops, while larger drops appear to possess a larger capture zone near the liquid-liquid interface than small drops.

10. Numerical simulations concerning drop concentration distributions conform qualitatively with the experimental findings and provide valuable insights into the roles played by shear flow (particularly at the liquid-liquid interface), and local mixing (particularly in the bubble street) in the transport of drops from the bulk to the liquid-liquid interface.

7 RECOMMENDATIONS

In order to refine our understanding and improve quantitative assessment of drop recovery in batch gas-agitated liquid-liquid dispersions the following courses of action are recommended.

1. In order to scale up the results of these experiments, the acquisition of additional experimental data is warranted. The impact of gas injection on fine drop recovery is affected by the presence of the cell walls. Consequently, the effect of mild gas agitation in a three dimensional flow field in particular should be investigated.

2. The effect of bubble size (which governs the size of mixing bandwidth) on drop recovery should be examined

3. Circulation induced by intermittent gas injection should be investigated.

4. More detailed information is needed concerning the hydrodynamic behavior around rising bubbles in bubble swarms. This applies in particular to the intensity of mixing in bubble wakes at different distances from the centerline of the bubble street.

5. The flow field close to the liquid-liquid interface plays an important role in fine drop recovery. The velocity profile in this region needs further investigation.

6. The flow field far from the bubble port and close to the gas-liquid interface plays an important role in conveying drops to the liquid-liquid interface. The flow field just below the gas-liquid interface is poorly defined and also requires further experimental and theoretical study.

REFERENCES

Anfruns, J.P. and Kitchener, J. A., (1977). Rates of capture of small particles in flotation. *Trans. Inst. Min. Metall.* 86, 9-21.

Bachalo, W., (1994). Experimental methods in multiphase flow. *Int. J. Multiphase Flow.* 20, Suppl., 261-295.

Basset, A.B., (1888). Treatise on Hydrodynamics. 2, Ch. 22. *Deighton Bell*, Cambridge, England. (Republished: Dover New York, 1961).

Batchelor, G.K., (1967). *An Introduction to Fluid Dynamics.* Cambridge University Press.

Becker, S., Sokolichin, A. and Eigenberger, G., (1994). Hydrodynamics of gas/liquid loop reactors- comparison of detailed experiments and flow simulations. *Pre-print of the 3rd German/Japanese Symposium on Bubble Columns,* Schwerte, Germany, 13-15 June, 223-228.

Brankovic, A., Borner, T. and Martin, W.W., (1984). The measurement of mass transfer coefficients of bubbles rising in liquids using Laser-Doppler Anemometry. *Laser Anemometry in Fluid Mechanics*. Lisbon, Ladoan.

Carderbank, P.H., (1985). Physical rate processes in industrial fermentation. *Trans. Inst. Chem. Engrs*, , 36, 443-452.

Cartellier, A., (1992). Local velocity and size measurements of particles in dense suspensions: Theory and design of endoscopic grating velocimeter-granulometers. *Applied optics*. 31, 18, 3493-3505.

Charles, G.E. and Mason, S.G., (1960). The coalescence of liquid drops at a flat liquid/liquid interface. *J. Colloid Sci.*, 15, 236-261.

Cook, T.L. and Harlow, F.H., (1986). Vortices in bubbly two-phase flow. *Int. J. Multiphase Flow*, 12, 35-61.

Coulaloglou, C.A. and Tavlarides, L.L., (1977). Description of interaction processes in agitated liquid-liquid dispersions. *Chem. Eng. Sci.*, 32, 1289-1337.

Davis, R.H., (1984). The rate of coagulation of a dilute polydispersed system of sedimenting spheres. *J. Fluid Mech.*, 145, 179-199.

Durst, F., (1973). Scattering phenomena and their application in Laser-Doppler Anemometry. *Journal of Applied Mathematics and Physics (ZAMP)*, 24, 4, 619-643.

Durst, F., Melling, A. and Whitelaw, J.H., (1981). Principles and practice of Laser-Doppler Anemometry. *2nd Edn. Academic Press, London.*

Durst, F., Schonung, B., Selanger, K. and Winter, M., (1986), Bubble -driven liquid flows. *J. Fluid. Mech.*, 170, 53-82.

Durst, F., Zare, M., (1975). Laser-doppler measurements in two-phase flows. *Proc. of the LDA-Symp.*, Denmark, 403-429.

East, T.W.R. and Marshall J.S., (1954). Turbulence in clouds as a factor in precipitation. *Q. J. R. Meteotol. Soc.*, 80, 26-41.

Flint, L.R. and Howarth, W.J., (1971). The collision efficiency of small particles with spherical air bubbles., *Chem. Eng. Sci.*, 26, 1155-1172.

Grienberger, J. and Hoffmann, H., (1992). Investigations and modelling of bubble columns. *Chem. Eng. Sci.*, 47, 2215-2220.

Han, Q. and Hunt, J.D., (1994). Particle pushing: the concentration of particles near a solid interface during downward flow. *Journal of Crystal Growth*, 140, 398-405.

Hardalupas, Y., Taylor, A. and Whitelaw, J., (1994). Mass-flux, mass fraction and concentration of liquid fuel in a swirl-stabilized flame. *Int. J. Multiphase Flow*, 20, Suppl., 233-259.

Hatzikiriakos, S.G., Gaikwad, R.P., Nelson, P.R. and Shaw, J. M., (1990). Hydrodynamics of gas-agitated liquid-liquid dispersions. *A.I.Ch.E.J.*, 36, 5, 677-684.

Hatzikiriakos, S.G., Gaikwad, R.P. and Shaw, J.M., (1990). Transitional drop size distributions in gas-agitated liquid-liquid dispersions. *Chem. Eng. Sci.*, 45, 8, 2349-2356.

Hejertager, B.H. and Morud, K., (1993). Computational fluid dynamics simulation of bioreactors. Paper presented at Bioreactor Performance Symposium, Helsingor, Denmark, 15-17 March.

Hillmer, G., Weismantel, L. and Hofmann, H., (1994). Investigations and modelling of slurry bubble columns. *Chem. Eng. Sci.*, 49, 837-843.

Howarth, W.J. (1967). Measurement of coalescence frequency in an agitated tank. *A.I.Ch.E.J.*, 13, 1007-1033.

Hulin, J.P., Fierfort, C. and Coudol, R. (1982). Experimental study of vortex emission behind bluff obstacles in gas liquid vertical two phase flow. *Int. J. Multiphase Flow*, 8, 475-490.

Jakobson, H.A., Svendsen, H.F. and Hjarbo, K.W., (1993). On the prediction of local flow structures in internal loop and bubble column reactors using a two-fluid model. *European Symposium on the computer aided Process Engineering-2.* 531-536.

Jeffery, G.V. and Davies, G.A., (1971). *Recent advances in liquid-liquid extraction*. Pergamon, Press, Oxford.

Johnson, S.T., (1990). On the modeling of disperse two phase flows. *Ph.D. Thesis*, The Norwegian Institute of Technology, Throndheim.

Jones, A.F. and Wilson, S.D.R., (1978). The film drainage problem in droplet coalescence. *J. Fluid Mech.*, 1978, 87, part 2, 268-288.

Konduru, R. and Shaw, J.M., (1990). *Proc. Int. Symp. On Material Handling in Pyrometallurgy, Hamilton, Ont.*, 14-24.

Landau, L.D. and Liftshitz, E.M. (1959). *Fluid Mechanics*. Pergamon, Oxford.

Lapin, A. and Lubbert, A., (1994). Numerical simulation of the dynamics of two-phase gas-liquid flows in bubble columns. *Chem. Eng. Sci.* 50, 371-398.

Levich, V.G., (1962). *Physicochemical Hydrodynamics*. Englewood, Cliffs, N.J.Prentice Hall, N.Y.

Lubbert, A. and Lapin A., (1994) A numerical fluid dynamics approach to structures in bubble columns. *Pre-prints of the 3rd German/Japanese Symposium on Bubble Columns*, Schwerte, Germany, 13-15 June, 79-88.

MacKay, G.D.M. and Mason, S.G., (1960). The gravity approach and coalescence of liquid drops at liquid interfaces. *Can. J. of Chem. Eng.*, 203-245.

Melik, D.H. and Folger, H.S., (1984). Gravity-induced flocculation. *J. Colloid Interface Sci.*, 101, 72-83.

Milynek, Y., and Treybal, R.E., (1972). Drop sizes in agitated liquid-liquid systems. *A.I.Ch.E J.*, 18 ,1 , 122-127.

Mok, Y.I. and Treybal, R.E., (1971). Continuous-phase mass transfer coefficient for liquid-liquid extraction in agitated vessels: II. *A.I.Ch.E.J.*, 17, 4, 916-920.

Noll, K.E. and Pilat, M.J., (1970). The impaction of particles upon rectangular bodies. *J. Colloid Interface Sci.*, 33, 197-221.

Oshinowa, T., (1972) Two phase flow in a vertical tube coil director. *Ph.D. Thesis.*, University of Toronto. Toronto, Canada.

Pancher, S., (1971). *Random functions and turbulence.* Pergamon, Oxford, 301.

Pavlushenko, I. S. and Yanishevskii, A. V., (1959). Magnitude of the interface area in mechanical agitation of mutually insoluble liquids. *J. Appl. Chem. USSR*, 32, 1529-1541

Reay, D. and Ratcliff, G.A., (1973). Removal of fine particles from water by dispersed air flotation :effect of bubble size and particle size on collection efficiency. *Cdn. J. Chem. Eng.*, 51, 178-192.

Rietema, K., (1982). Science and technology of dispersed two phase systems-I and II. *Chem. Eng. Sci.*, 37, 1125-1150.

Ross, S.L., and Curl, R.L., (1973). Measurements and models of the dispersed phase mixing process. Paper No. 29b, Joint. *Chem. Eng. Conf., 4th, Vancouver.*

Saffman, P.G., and Turner, J.S., (1956). On the collision of drops in turbulent clouds. *J. Fluid Mech.*, 1, 16-30.

Schwarz, M.P. and Turner, W.J., (1988). Applicability of the standard k-ε turbulent model to gas stirred baths. *Appl. Math. Modelling*, 12, 273-279.

Shahrokhi, H. and Shaw, J.M., (1994). The origin of fine drop recovery in batch gas agitated liquid-liquid systems. *Chem. Eng. Sci.*, 49, 24B, 5203-5213.

Shahrokhi, H. and Shaw, J.M., (1996). Enhancing metal/matte recovery in batch gas-agitated slag metal /matte systems. *Pyrometallurgy Fundamentals and Process Development, Proceedings of the Nickel-Cobalt 97 Intern. Symp.* Sudbury, Canada. 2, 40-49.

Sharifi, H. and Shaw, J.M., (1996). Secondary drop production in packed-bed coalescers. *Chem. Eng. Sci.*, 51, 21, 4817-4826.

Shaw, J. M and Konduru, R., (1992). The behaviour of large gas bubbles at the liquid-liquid interface. Part 2: Liquid-entrainment. *Can. J. Chem. Eng.*, 70, 381-384.

Shinnar, R., (1961). On the behaviour of liquid Dispersions in mixing vessels. *J. Fluid Mech.*, 1961, 10, 259-287.

Sokolichin, A. and Eigenberger, G., (1994). Gas-liquid flow in bubble columns and loop reactors: Part I. & Part II. *Chem. Eng. Sci.*, 49, 24B, 5735-5762.

Svendsen, H.F., Jackobson, H.A. and Torvik R., (1992). Local flow structures in internal loop and bubble column reactors. *Chem. Eng. Sci.*, 47, 3297-3304.

Thomas, N.H., Auton, T.R., Sene, K. and Hunt, J.C.R., (1983). Entrapment and transport of bubbles in transient large eddies in multiphase turbulent shear flows. *International conference on the physical modelling of multi-phase flows*, Coventry, UK., 169-184

Thomas, R.M., (1981). Bubble coalescence in turbulent flows. *Int. J. Multiphase Flow*. 7, 709-725.

Trovik, R. and Svendsen H.F., (1990). Modelling of slurry reactors: a fundamental approach. *Chem. Eng. Sci.*, 45, 2325-2332.

Webb, C., Que, F. and Senior, P.R., (1992). Dynamic simulation of gas-liquid

dispersion behaviour in a 2-D bubble column using a graphics mini-supercomputer. *Chem. Eng. Sci.*, 47, 3305-3312.

Weber M.E., (1981). In-line interaction of a pair of bubbles in a viscous liquid. *J. Sep. Proc. Technol.*, 2, 29-34.

Weiland, R.H. & McPherson, R.R., (1979). Accelerated settling by addition of buoyant Particles. *Ind. Engng. Chem. Fundls*. 18, 45-49

Wen, C.S. and Batchelor, G.K., (1985). The rate of coagulation in a dilute suspension of small particles. *Scientia Sinica.* A28, 172-184

Zinchenko, A.Z., (1982). Calculation of the effectiveness of gravitational coagulation of drops with allowance for internal circulation. *Prikl. Mat. Mech.*, 46, 58-65.

Appendix A DROP CONCENTRATION AND RECOVERY RATE MODEL

A.1 Introduction

The routine which controls the overall program sequence for drop trajectory calculations is shown schematically in Figure A.1. First the initial drop position, physical properties of the continuous phase and the drop are read from a file (vel.inp). Then experimental velocity components at 32 grid points are stored in two arrays. Velocities at the center of the bubble street and along the gas-liquid interface are calculated by integration over experimental velocities. The values of velocities at the liquid-liquid interface and the wall are assumed to be zero.

The third step is to identify the length of the re-entry zone for a particular bandwidth. Drop re-entry position is calculated based on the random numbers generated with the same distribution as the velocity distribution of flow coming out of the mixing zone.

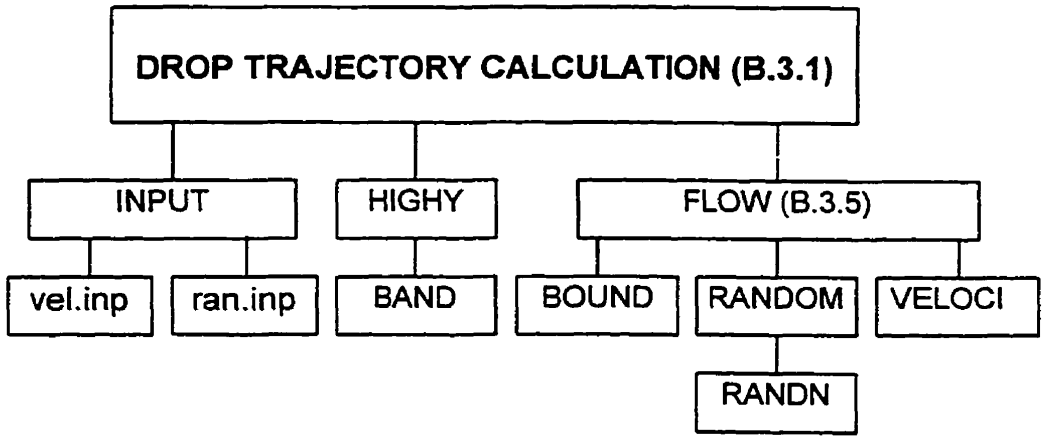

Figure A.1 -Schematic structure of drop trajectory calculation program.

Following this step the main part of the program performs a force balance around the drop. The integrated positions of drops are then calculated after each time step.

The routines used to calculate recovery rates and spacial drop concentration distributions also follow the same structure as in Figure A1. The only difference is the type and extent of output.

The Program given in section A.3.4 calculates the position probability distribution for drops exiting the bubble street (see figure 5.4). This distribution is matched to the velocity distribution of flow exiting the mixing zone.

A.2 FORTRAN implementation

List of principle variables

Program Symbol	*Definition*
A,B,C,D,E	Constants
BHIS	Basset history
CDENS	Continuous phase density
DELTAT	Time step
DDENS	Drop density
DUX	Temporary variable for DDUX
DUY	Temporary variable for DDUY
DDUX	First derivative of drop velocity component (x-direction)
DDUY	First derivative of drop velocity component (y-direction)
RAD	Drop radius
RAND	Random number
SGX	G_x
SGY	G_y
SUMX	Basset history integral (x-direction)
SUMY	Basset history integral (y-direction)
U	Continuous phase velocity at grid points (x-direction)

UG2 and UG1	Horizontal components of continuous phase velocity above and below the drop
UI	Relative velocity of flow coming out of the mixing zone
UX	Dispersed phase velocity component (x-direction)
UY	Dispersed phase velocity component (y-direction)
V	Continuous phase velocity at grid points (y-direction)
VG2 and VG1	Vertical components of continuous phase velocities at the left and right of the drop
VIS	Continuous phase viscosity
VX	Continuous phase velocity component (x-direction)
VY	Continuous phase velocity component (y-direction)
X	X-coordinate
Y	Y-coordinate
YI	Relative coordinate between 6.2 to 7.6 (y-direction)
YHIGH	The height that the last complete circulation loop touches the mixing zone.
XBAND	Mixing zone bandwidth

A.3 Main programs

A.3.1 Drop trajectory calculation in circulation loops

```
C=======================================================
C       Main Program
C=======================================================

        DIMENSION U(6,9),V(6,9),DUX(5),DUY(5),BHIS(5),UI(15),YI(15)
        DOUBLE PRECISION A,B,C,D,E,VX,VY,UX,UY,DDUX,DDUY,
     + U,V,X,Y,BHIS,YHIGH,XBAND,RAND,SGX,SGY,UG1,UG2,VG1,VG2,
     + DRAGX,DRAGY
        NTEGER S(3)
        OPEN (1,FILE='vel.inp')
        OPEN (2,FILE='ran.inp')
        OPEN (3,FILE='PRO.OUT')

C       READ INITIAL POSITION OF DROP (0.0<X<4.2),(0.0<Y<7.6)

        READ *,X,Y
        Y=Y+0.8
        X=X+1.0
        READ (1,*)DDENS,CDENS,VIS,RAD,XBAND
        XBAND=XBAND+1.0
        DO 10 J=1,8
        DO 10 I=2,6
                READ (1,*)U(I,J),V(I,J)
10      CONTINUE

        DO 16 J=1,8
                V(1,J)=-(2*(V(2,J)+V(3,J)+V(4,J))+1.2*V(5,J)+0.2*V(6,J))
16              U(1,J)=0.0
        DO 17 I=2,6
                U(I,9)=-1.67*(0.2*U(I,1)+1.2*U(I,2)+2*(U(I,3)+U(I,4)+U(I,5)
     +          +U(I,6)+U(I,7))+1.4*U(I,8))
17              V(I,9)=0.0
        U(1,9)=0.0
        V(1,9)=0.0
        U(1,1)=0.0
        V(1,1)=0.0

        CALL ITIME(S)
        N=S(2)*S(3)
        DO 1 I=1,15
1               READ (2,*) YI(I),UI(I)

        DELTAT=0.0001
        A=(DDENS+CDENS/2)
        B=4.5*VIS/(A*RAD**2)
        C=-980.665*(DDENS-CDENS)/A
        D=2.53885*SQRT(CDENS*VIS)/(A*RAD)
        E=6.46*VIS*(RAD**2)/(SQRT(VIS/CDENS)*DDENS)

        DO 2 J=1,5
```

```
2           BHIS(J)=D*DELTAT/SQRT(1.0*J)
      TIME=0.0
      K=0
      I=-1
      O=0.0
      CALL HIGHY(U,V,XBAND,DELTAT,YHIGH)
      PRINT 100

C     CALCULATE CONTINUOUS PHASE VELOCITIES IN X AND Y DIRECTION

      CALL FLOW(U,V,YI,UI,X,Y,YHIGH,XBAND,N,VX,VY)
      UX=VX
      UY=VY
      DDUX=0.0
      DDUY=0.0
      DO 5 J=1,5
           DUX(J)=DDUX
5          DUY(J)=DDUY
      SUMX=0.0
      SUMY=0.0


C     START CALCULATING NEW DROP POSITON IN X AND Y DIRECTIONS

11    CALL FLOW(U,V,YI,UI,X,Y+RAD,YHIGH,XBAND,N,UG2,VY)
      CALL FLOW(U,V,YI,UI,X,Y-RAD,YHIGH,XBAND,N,UG1,VY)
      CALL FLOW(U,V,YI,UI,X+RAD,Y,YHIGH,XBAND,N,VX,VG2)
      CALL FLOW(U,V,YI,UI,X-RAD,Y,YHIGH,XBAND,N,VX,VG1)
      SGX=SQRT(ABS(UG2-UG1)/(2*RAD))
      SGY=SQRT(ABS(VG2-VG1)/(2*RAD))
      DO 12 J=1,5
           SUMX=SUMX+DUX(J)*BHIS(J)
12         SUMY=SUMY+DUY(J)*BHIS(J)
      DDUX=(E*SGY-B)*(UX-VX)-SUMX
      DDUY=C+(E*SGX-B)*(UY-VY)-SUMY
      DUX(1)=DDUX
      DUY(1)=DDUY
      DO 15 J=2,5
           DUX(J)=DUX(J-1)
15         DUY(J)=DUY(J-1)
      UX=UX+DDUX*DELTAT
      UY=UY+DDUY*DELTAT
      X=X+UX*DELTAT+0.5*DDUX*(DELTAT*DELTAT)
      Y=Y+UY*DELTAT+0.5*DDUY*(DELTAT*DELTAT)

C     CALCULATE CONTINUOUS PHASE VELOCITIES IN NEW POSITION

      CALL FLOW(U,V,YI,UI,X,Y,YHIGH,XBAND,N,VX,VY)
      TIME=TIME+DELTAT
      I=I+1
      O=I/1000.0
      IF ((O-INT(O)).EQ.0.0) GOTO 21
      IF (Y.LE.0.80) GOTO 90
      GOTO 11
```

```
 21     PRINT 25,X-1.0,Y-0.8,TIME
        WRITE(3,25)X-1.0,Y-0.8,TIME
        GOTO 11
 90     WRITE(3,25)X-1,Y-0.8,TIME
        WRITE(3,95)
 22     FORMAT(2F10.5)
 25     FORMAT(F6.3,3X,F6.3,3X,F6.1)
 95     FORMAT('DROP HAS REACHED THE INTERFACE')
 100    FORMAT(1X,'X-COORD',2X,'Y-COORD',2X,'TIME(SEC)')
 105    STOP
        END
```

A.3.2 Drop recovery rate prediction

```
C=============================================================
C       Main Program
C=============================================================

        DIMENSION U(6,9),V(6,9),DUX(5),DUY(5),BHIS(5),UI(15),YI(15),M(9)
        DOUBLE PRECISION A,B,C,D,E,VX,VY,UX,UY,DDUX,DDUY,
     +  U,V,X,Y,BHIS,YHIGH,XBAND,SGX,SGY,UG1,UG2,VG1,VG2, XO,YO
        INTEGER S(3),CO
        OPEN (1,FILE='vel.inp')
        OPEN (2,FILE='PRO.OUT')
        OPEN (3,FILE='ran.inp')

        READ (1,*)DDENS,CDENS,VIS,RAD,XBAND
        XBAND=XBAND+1.0
        DO 10 J=1,8
        DO 10 I=2,6
        READ (1,*)U(I,J),V(I,J)
 10     CONTINUE

        DO 16 J=1,8
                V(1,J)=-(2*(V(2,J)+V(3,J)+V(4,J))+1.2*V(5,J)+0.2*V(6,J))
 16             U(1,J)=0.0
        DO 17 I=2,6
                U(I,9)=-1.67*(0.2*U(I,1)+1.2*U(I,2)+2*(U(I,3)+U(I,4)+U(I,5)
     +          +U(I,6)+U(I,7))+1.4*U(I,8))
 17             V(I,9)=0.0
        U(1,9)=0.0
        V(1,9)=0.0
        U(1,1)=0.0
        V(1,1)=0.0

        CALL ITIME(S)
        N=S(2)*S(3)
        DO 1 I=1,15
 1              READ (3,*) YI(I),UI(I)

        DELTAT=0.0001
        A=(DDENS+CDENS/2)
```

```
      B=4.5*VIS/(A*RAD**2)
      C=-980.665*(DDENS-CDENS)/A
      D=2.53885*SQRT(CDENS*VIS)/(A*RAD)
      E=6.46*VIS*(RAD**2)/(SQRT(VIS/CDENS)*DDENS)
      DO 2 J=1,5
2           BHIS(J)=D*DELTAT/SQRT(1.0*J)
      K=0
      CALL HIGHY(U,V,XBAND,DELTAT,YHIGH)

C     CALCULATE CONTINUOUS PHASE VELOCITIES IN X AND Y DIRECTION

      DO 3 I=1,9
3           M(I)=0

      DO 35 K=1,23
            X=1.0+K*0.18
      DO 35 L=1,42
            Y=0.8+L*0.18
      TIME=0.0
      I=0
      O=0.0
      CALL FLOW(U,V,YI,UI,X,Y,YHIGH,XBAND,N,VX,VY)
      UX=VX
      UY=VY
      DDUX=0.0
      DDUY=0.0
      DO 5 J=1,5
            DUX(J)=DDUX
5           DUY(J)=DDUY
      SUMX=0.0
      SUMY=0.0

C     START CALCULATING NEW DROP POSITON IN X AND Y DIRECTIONS

11    CALL FLOW(U,V,YI,UI,X,Y+RAD,YHIGH,XBAND,N,UG2,VY)
      CALL FLOW(U,V,YI,UI,X,Y-RAD,YHIGH,XBAND,N,UG1,VY)
      CALL FLOW(U,V,YI,UI,X+RAD,Y,YHIGH,XBAND,N,VX,VG2)
      CALL FLOW(U,V,YI,UI,X-RAD,Y,YHIGH,XBAND,N,VX,VG1)
      SGX=SQRT(ABS(UG2-UG1)/(2*RAD))
      SGY=SQRT(ABS(VG2-VG1)/(2*RAD))
      DO 12 J=1,5
            SUMX=SUMX+DUX(J)*BHIS(J)
12          SUMY=SUMY+DUY(J)*BHIS(J)
      DDUX=(E*SGY-B)*(UX-VX)-SUMX
      DDUY=C+(E*SGX-B)*(UY-VY)-SUMY
      DUX(1)=DDUX
      DUY(1)=DDUY
      DO 15 J=2,5
            DUX(J)=DUX(J-1)
15          DUY(J)=DUY(J-1)
      UX=UX+DDUX*DELTAT
      UY=UY+DDUY*DELTAT
      X=X+UX*DELTAT+0.5*DDUX*(DELTAT*DELTAT)
      Y=Y+UY*DELTAT+0.5*DDUY*(DELTAT*DELTAT)
```

```
C   CALCULATE CONTINUOUS PHASE VELOCITIES IN NEW POSITION

        CALL FLOW(U,V,YI,UI,X,Y,YHIGH,XBAND,N,VX,VY)

        TIME=TIME+DELTAT
        I=I+1
        O=I/300000.0
        IF (Y.LE.0.8) THEN
        M(INT(O+1))=M(INT(O+1))+1
        GOTO 35
        ENDIF
        GOTO 11
35      CONTINUE
        PRINT 25,(M(I),I=1,9)
25      FORMAT(9(I4,2X))
105     STOP
        END
```

A.3.3 Spacial drop concentration distribution

```
C=======================================================================
C       Main Program
C=======================================================================

        DIMENSION U(6,9),V(6,9),DUX(5),DUY(5),BHIS(5),UI(15),YI(15)
        DOUBLE PRECISION A,B,C,D,E,VX,VY,UX,UY,DDUX,DDUY,
     +  U,V,X,Y,BHIS,YHIGH,XBAND,SGX,SGY,UG1,UG2,VG1,VG2,XO,YO
        INTEGER S(3),CO
        OPEN (1,FILE='vel.inp')
        OPEN (2,FILE='ran.inp')
        OPEN (4,FILE='PRO.OUT')
        OPEN (5,FILE='1.OUT')
        OPEN (8,FILE='2.OUT')
        OPEN (10,FILE='3.OUT')

        READ (1,*)DDENS,CDENS,VIS,RAD,XBAND
        XBAND=XBAND+1.0
        DO 10 J=1,8
        DO 10 I=2,6
                READ (1,*)U(I,J),V(I,J)
10      CONTINUE

        DO 16 J=1,8
                V(1,J)=-(2*(V(2,J)+V(3,J)+V(4,J))+1.2*V(5,J)+0.2*V(6,J))
16              U(1,J)=0.0
        DO 17 I=2,6
                U(I,9)=-1.67*(0.2*U(I,1)+1.2*U(I,2)+2*(U(I,3)+U(I,4)+U(I,5)
     +          +U(I,6)+U(I,7))+1.4*U(I,8))
17              V(I,9)=0.0
        U(1,9)=0.0
        V(1,9)=0.0
        U(1,1)=0.0
```

```
      V(1,1)=0.0

      CALL ITIME(S)
      N=S(2)*S(3)
      DO 1 I=1,15
1           READ (2,*) YI(I),UI(I)

      DELTAT=0.0001
      A=(DDENS+CDENS/2)
      B=4.5*VIS/(A*RAD**2)
      C=-980.665*(DDENS-CDENS)/A
      D=2.53885*SQRT(CDENS*VIS)/(A*RAD)
      E=6.46*VIS*(RAD**2)/(SQRT(VIS/CDENS)*DDENS)

      DO 2 J=1,5
2     BHIS(J)=D*DELTAT/SQRT(1.0*J)
      K=0
      CALL HIGHY(U,V,XBAND,DELTAT,YHIGH)

C     CALCULATE CONTINUOUS PHASE VELOCITIES IN X AND Y DIRECTION

      M=1.0
      DO 35 K=1,22
      X=1.0+k*0.18
      DO 35 L=1,41
      Y=0.8+L*0.18
      TIME=0.0
      I=0
      O=0.0
      CALL FLOW(U,V,YI,UI,X,Y,YHIGH,XBAND,N,VX,VY)
      UX=VX
      UY=VY
      DDUX=0.0
      DDUY=0.0
      DO 5 J=1,5
            DUX(J)=DDUX
5           DUY(J)=DDUY
      SUMX=0.0
      SUMY=0.0

C     START CALCULATING NEW DROP POSITON IN X AND Y DIRECTIONS

11    CALL FLOW(U,V,YI,UI,X,Y+RAD,YHIGH,XBAND,N,UG2,VY)
      CALL FLOW(U,V,YI,UI,X,Y-RAD,YHIGH,XBAND,N,UG1,VY)
      CALL FLOW(U,V,YI,UI,X+RAD,Y,YHIGH,XBAND,N,VX,VG2)
      CALL FLOW(U,V,YI,UI,X-RAD,Y,YHIGH,XBAND,N,VX,VG1)
      SGX=SQRT(ABS(UG2-UG1)/(2*RAD))
      SGY=SQRT(ABS(VG2-VG1)/(2*RAD))
      DO 12 J=1,5
            SUMX=SUMX+DUX(J)*BHIS(J)
12          SUMY=SUMY+DUY(J)*BHIS(J)
      DDUX=(E*SGY-B)*(UX-VX)-SUMX
      DDUY=C+(E*SGX-B)*(UY-VY)-SUMY
      DUX(1)=DDUX
```

```
      DUY(1)=DDUY
      DO 15 J=2,5
            DUX(J)=DUX(J-1)
15          DUY(J)=DUY(J-1)
      UX=UX+DDUX*DELTAT
      UY=UY+DDUY*DELTAT
      X=X+UX*DELTAT+0.5*DDUX*(DELTAT*DELTAT)
      Y=Y+UY*DELTAT+0.5*DDUY*(DELTAT*DELTAT)
C   CALCULATE CONTINUOUS PHASE VELOCITIES IN NEW POSITION
      CALL FLOW(U,V,YI,UI,X,Y,YHIGH,XBAND,N,VX,VY)

      TIME=TIME+DELTAT
      I=I+1
      O=I/300000.0
      IF (I.GE.300000) GOTO 90
      IF (Y.LE.0.8) GOTO 34
      GOTO 11
90    PRINT 25,INT(X+0.8)-1.0,INT(Y+0.2)-0.0,INT(O),M
      WRITE(4,25) INT(X+0.8)-1.0,INT(Y+0.2)-0.0,INT(O),M
      IF ((X.GT.4.2).AND.(Y.LT.3.8)) THEN
      XO=3.2+0.2*INT(5*(X-4.21))
      IF (Y.LT.1.8) GOTO 91
      IF (Y.LT.2.8) GOTO 92
      IF (Y.LT.3.8) GOTO 93
91    WRITE (5,25) XO,0.2*INT(5*(Y-0.8)),INT(O),M
      GOTO 95
92    WRITE (8,25) Xo,1+0.2*INT(5*(Y-1.8)),INT(O),M
      GOTO 95
93    WRITE (10,25) Xo,2+0.2*INT(5*(Y-2.8)),INT(O),M
95    ENDIF
34    M=M+1
35    CONTINUE
25    FORMAT(F6.2,3X,F6.2,3X,I3,3x,I5)
00    FORMAT(1X,'X-COORD',2X,'Y-COORD',2X,'TIME(SEC)')
05    STOP
      END
```

A.3.4 Random number probability distribution

```
C=====================================================================
C     Main Program
C=====================================================================
      DIMENSION U(6,9),V(6,9),UI(15),YI(15),UIC(14),YIC(14)
      DOUBLE PRECISION U,V,X,Y,YHIGH,XBAND,SEG,VICC,SUM,
     *UIC,YIC,VIC,DDENS,CDENS,VIS,RAD,DELTAT
      OPEN (1,FILE='vel.inp')
      OPEN (2,FILE='ran.inp')
      READ (1,*)DDENS,CDENS,VIS,RAD,XBAND
      XBAND=XBAND+1.0
      DO 10 J=1,8
      DO 10 I=2,6
            READ (1,*)U(I,J),V(I,J)
10    CONTINUE
```

```
      DO 16 J=1,8
            V(1,J)=-(2*(V(2,J)+V(3,J)+V(4,J))+1.2*V(5,J)+0.2*V(6,J))
16          U(1,J)=0.0
      DO 17 I=2,6
            U(I,9)=-1.67*(0.2*U(I,1)+1.2*U(I,2)+2*(U(I,3)+U(I,4)+U(I,5)
     +      +U(I,6)+U(I,7))+1.4*U(I,8))
17          V(I,9)=0.0
      U(1,9)=0.0
      V(1,9)=0.0
      U(1,1)=0.0
      V(1,1)=0.0

      DELTAT=0.0001
      CALL HIGHY(U,V,XBAND,DELTAT,YHIGH)
      SEG=(8.4-YHIGH)/14.0
      SUM=0.0
      X=xband
      VIC=0.0
      DO 6 I=1,14
            YIC(I)=YHIGH+SEG*I
            CALL VELOCI(U,X,YIC(I),UIC(I))
            SUM=SUM+UIC(I)*SEG
6           YIC(I)=SEG*I/(8.4-YHIGH)
      VICC=0.0
      DO 7 I=1,14
            VICC=VICC+UIC(I)*SEG
7           UIC(I)=VICC/SUM
      LO=15
      DO 8 I=1,14
            LO=LO-1
            YI(I)=YIC(LO)
8           UI(I)=UIC(LO)
      YI(15)=0.0
      UI(15)=0.0
      DO 9 I=1,15
            PRINT *,YI(I),UI(I)
9           WRITE (2,*)YI(I),UI(I)
25    FORMAT (2(F7.3,2X))
      STOP
      END
```

A.3.5 Subroutines reffered in main programs

```
C     THIS SUBROUTINE EVALUATES THE POSITION OF THE DROP IN BOUNDARIES

      SUBROUTINE FLOW(U,V,YI,UI,X,Y,YHIGH,XBAND,N,VX,VY)
      DOUBLE PRECISION U,V,X,XI,Y,VX,VY,YHIGH,XBAND
      DIMENSION U(6,9),V(6,9),UI(15),YI(15)
      IF (X.LT.XBAND) GOTO 14
      IF (Y.LT.1.0) GOTO 12
      GOTO 23
```

```
 12     CALL BOUND(V,X,Y,VY)
        CALL BOUND(U,X,Y,VX)
        GOTO 40
 14     CALL RANDOM(N,YI,UI,RAND)
        Y=YHIGH+RAND*(8.4-YHIGH)
        N=N+1
        X=2.0
 23     CALL VELOCI(V,X,Y,VY)
        CALL VELOCI(U,X,Y,VX)
        IF (Y.GT.8.4) VY=0.0
        IF (X.GE.5.2) VX=-VX
 40     RETURN
 25     FORMAT(F6.3,3X,F6.3,3X,F5.2)
        END

*******************************************************************************************************************
C       THIS SUBROUTINE EVALUATES CONTINUOUS PHASE VELOCITIES IN X AND Y
C       DIRECTIONS

        SUBROUTINE VELOCI(VEL,X,Y,UORV)
        DOUBLE PRECISION VEL,X,Y,UORV,ALPHA,BETA
        DIMENSION  VEL(6,9)
        ALPHA=(Y-INT(Y))
        BETA=(X-INT(X))
        UORV=(1-ALPHA)*(1-BETA)*VEL(INT(X),INT(Y))+ALPHA*(1-BETA)*
     + VEL(INT(X),INT(Y+1))+BETA*(1-ALPHA)*VEL(INT(X+1),INT(Y))+
     + ALPHA*BETA*VEL(INT(X+1),INT(Y+1))
        RETURN
        END

*******************************************************************************************************************
C       THIS SUBROUTINE CALCULATES THE VELOCITIES CLOS TO LIQUID-
C       LIQUID INTERFACE.

        SUBROUTINE BOUND(VEL,X,Y,UORV)
        DOUBLE PRECISION VEL,X,Y,BETA,UORV
        DIMENSION VEL(6,9)
        BETA=(X-INT(X))
        UORV=(1-BETA)*VEL(INT(X),INT(Y+1))+BETA*VEL(INT(X+1),
     * INT(Y+1))
        UORV=UORV*((Y-0.8)/0.2)
        RETURN
        END

*******************************************************************************************************************
C       THIS FOLLOWING SUBROUTINES GENERATE THE RANDOM NUMBERS BASED
C       ON THE FLUID VELOCITY PROFILE CLOSE TO GAS-LIQUID INTERFACE

        SUBROUTINE RANDOM(N,YI,UI,RAND)
        DIMENSION YI(15),UI(15)
        REAL U ,RAND
        CALL RANDN(N,U)
```

```
      J=15
5     J=J-1
      IF (U.LT.UI(J)) THEN
      RAND=(U-UI(J+1))*(YI(J+1)-YI(J))/(UI(J+1)-UI(J))+YI(J+1)
      GOTO 18
      ENDIF
      GOTO 5
18    RETURN
      END

      SUBROUTINE RANDN(N,U)
      REAL U
      INTEGER N,NO
      NO=N
      NO=NO*843314861+453816693
      IF (NO.LT.0) THEN
      NO=NO+2147483647+1
      ENDIF
      U=NO*0.4656612E-9
      RETURN
      END
```

****

```
C     THE FOLLOWING SUBROUTINES CALCULATE THE HEIGHT THAT THE
C     CIRCULATING LOOPS TOUCH THE MIXING BANDWIDTH

      SUBROUTINE HIGHY(U,V,XBAND,DELTAT,YHIGH)
      DOUBLE PRECISION U,V,Y,VY,VX,X,XBAND,YHIGH
      CALL BAND(U,XBAND,Y)
      X=XBAND
10    CALL VELOCI(V,X,Y,VY)
      CALL VELOCI(U,X,Y,VX)
      IF ((2.0-X).LT.0.0) GOTO 20
      X=X+UX*DELTAT
      Y=Y+VY*DELTAT
      GOTO 10
20    YHIGH=Y
      RETURN
      END

      SUBROUTINE BAND(U,XBAND,Y)
      DOUBLE PRECISION U,XBAND,Y,VX,X
      Y=8.4
      X=XBAND
10    Y=Y-0.001
      CALL VELOCI(U,X,Y,VX)
      IF (UX.LT.0.0) GOTO 20
      GOTO 10
20    RETURN
      END
```

IMAGE EVALUATION TEST TARGET (QA-3)

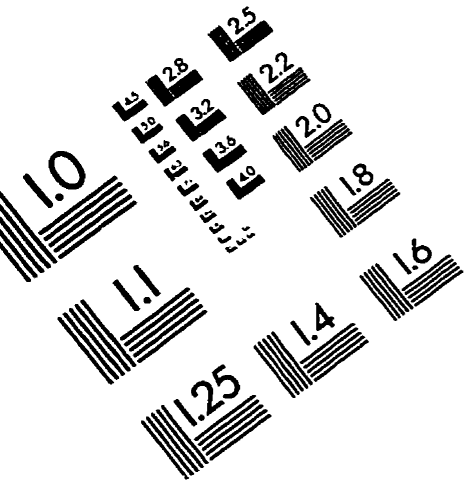

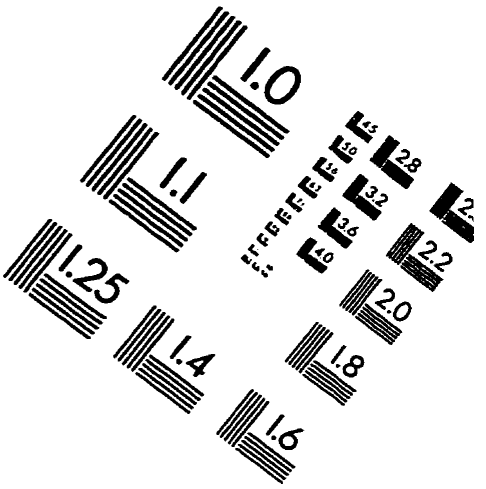

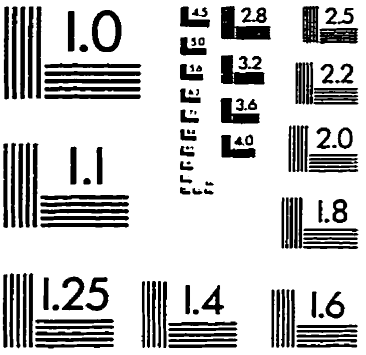

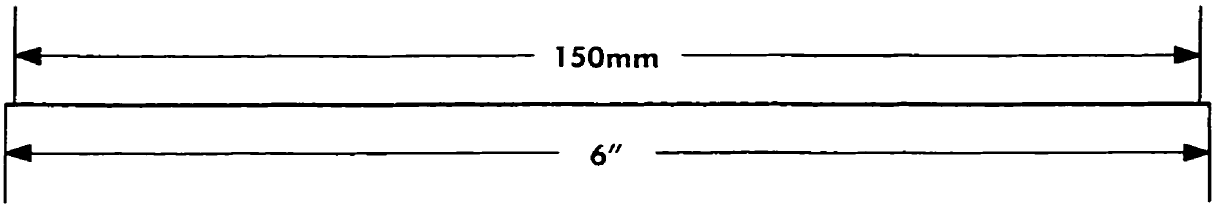

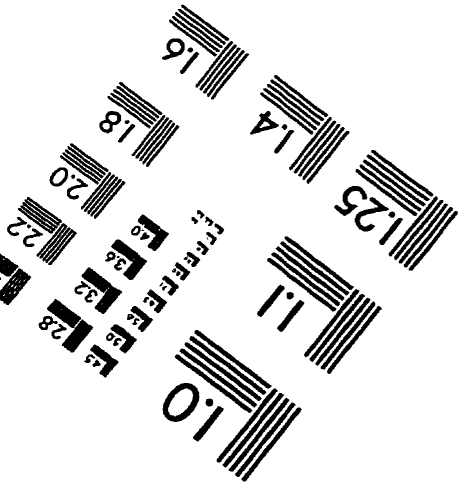

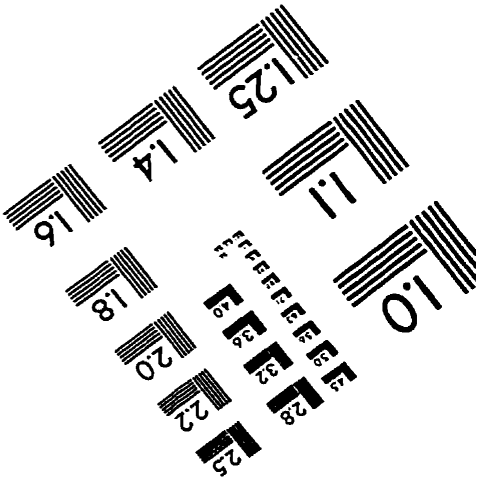

APPLIED IMAGE, Inc
1653 East Main Street
Rochester, NY 14609 USA
Phone: 716/482-0300
Fax: 716/288-5989